

**UNIVERSIDADE DE SÃO PAULO
INSTITUTO DE FÍSICA DE SÃO CARLOS**

Bruno Nicolau Santos

**Monte Carlo simulation proposal for narrow-line
magneto-optical traps**

São Carlos

2023

Bruno Nicolau Santos

**Monte Carlo simulation proposal for narrow-line
magneto-optical traps**

Dissertation presented to the Graduate
Program in Physics at the Instituto de Física
de São Carlos da Universidade de São Paulo,
to obtain the degree of Master in Science.

Concentration area: Applied Physics

Advisor: Prof. Dr. Emanuel Alves de Lima
Henn

Original version

**São Carlos
2023**

I AUTHORIZE THE REPRODUCTION AND DISSEMINATION OF TOTAL OR PARTIAL COPIES OF THIS DOCUMENT, BY CONVENTIONAL OR ELECTRONIC MEDIA FOR STUDY OR RESEARCH PURPOSE, SINCE IT IS REFERENCED.

Santos, Bruno Nicolau

Monte Carlo simulation proposal for narrow-line
magneto-optical traps / Bruno Nicolau Santos; advisor
Emanuel Alves de Lima Henn -- São Carlos 2023.

93 p.

Dissertation (Master's degree - Graduate Program in
Theoretical and Experimental Physics) -- Instituto de
Física de São Carlos, Universidade de São Paulo - Brasil ,
2023.

1. Magneto-optical trap. 2. Monte Carlo simulation. 3.
Laser cooling. I. Alves de Lima Henn, Emanuel, advisor.
II. Title.

ACKNOWLEDGEMENTS

I would like to acknowledge the support and patience of my advisor, Professor Emanuel A. L. Henn, who helped me proceed with my work even through the difficulties.

Many thanks to my father, Rogério C. Santos, my mother, Adeli C. C. Santos, and my sister Andressa C. N. Santos, who supported me throughout the process by keeping me motivated and always being present when I most needed them. I could not have finished this work without them. I would also like to thank my girlfriend and also my partner, Denise S. Ribeiro, who follows my dedication and keeps supporting me during the process.

Lastly, but not less important, I would like to thank my closest friends Adonai H. Silva, Cainã de Oliveira, Henrique Malavazzi, Raian Westin, and Vinicius Martinez (in alphabetical order since I value them equally) for all their support, insightful conversations, and unforgeable moments.

This study was financed in part by the Coordenação de Aperfeiçoamento de Pessoal de Nível Superior – Brasil (CAPES) – Finance Code 001

ABSTRACT

SANTOS, B. N. **Monte Carlo simulation proposal for narrow-line magneto-optical traps**. 2023. 93p. Dissertation (Master in Science) - Instituto de Física de São Carlos, Universidade de São Paulo, São Carlos, 2023.

In this work, we proposed and implemented a Monte Carlo simulation to estimate experimental quantities of narrow-line magneto-optical traps (nMOTs). Our model relies on sampling the atoms' movement under laser light and a quadrupole magnetic field as a Markov chain. We assume that the involved electronic transition can be modelled as a four-level system and split into three independent two-level systems, which is only valid for nMOTs in the power-broadened regime. We were able to estimate quantities for three nMOT arrangements at different laboratories. The first nMOT traps dysprosium atoms on an electronic transition with narrowness $\eta = 43.8$, which is not an ideal value since it is slightly larger. Nevertheless, we could obtain estimated quantities that were more accurate than the theoretical predictions. The other two nMOTs trap strontium atoms on an electronic transition with narrowness $\eta = 1.6$. We could also obtain estimated quantities close to the experimental measures in this case.

Keywords: Magneto-optical trap. Monte Carlo simulation. Laser cooling.

RESUMO

SANTOS, B. N. **Proposta de simulação de Monte Carlo para armadilhas magneto-ópticas de linha estreita.** 2023. 93p. Dissertação (Mestrado em Ciências) - Instituto de Física de São Carlos, Universidade de São Paulo, São Carlos, 2023.

Nesse trabalho, propomos e implementamos uma simulação de Monte Carlo para estimar quantidades experimentais de armadilhas magneto-ópticas de linhas estreita (nMOTs). Nosso modelo se baseia em amostrar o movimento dos átomos expostos a luz laser e um campo magnético quadrupolar como uma cadeia de Markov. Nós assumimos que a transição eletrônica envolvida pode ser modelada como um sistema de quatro níveis e, então, a dividimos em três sistemas de dois níveis independentes sobre a suposição em que nMOT esteja no regime de alargamento por potência. Nós fomos capazes de estimar três nMOTs de diferentes laboratórios. O primeiro aprisiona átomos de disprósio em uma transição cuja estreiteza é 43,8, o que não é um valor ideal por ser ligeiramente elevado. Apesar disso, nós obtivemos quantidades estimadas mais precisas que as previstas teoricamente. Os outros dois nMOTs aprisionam estrôncio em uma transição com estreiteza 1,6. Nesse caso, nós também obtivemos quantidades estimadas próximas as medidas experimentais.

Palavras-chave: Armadilha magneto-óptica. Simulação de Monte Carlo. Resfriamento a laser.

LIST OF FIGURES

Figure 1 – Representative illustration of stimulated absorption and emission, and spontaneous emission. In figure (a), an atom in the lower level goes into the upper level absorbing a photon with energy $\hbar\omega_0$ from a light field with $u(\omega_0) > 0$. In figure (b), an atom in the upper level decays into the lower level in the presence of a light field with $u(\omega_0) > 0$, emitting a photon with energy $\hbar\omega_0$ similar to the photons in the light field. In figure (c), an atom in the upper level emits an isotropic photon with energy $\hbar\omega_0$ spontaneously, decaying into the lower level.	22
Figure 2 – Representative illustration of optical two-level transitions. In figure (a), it is represented the absorption or emission spectrum without line-broadening mechanisms so that we can assume the line shape $g(\omega) = \delta(\omega - \omega_0)$. In figure (b), it is represented the absorption or emission spectrum taking line-broadening mechanisms into account. . .	24
Figure 3 – Dilute atomic gas interacting with a electromagnetic radiation in a slab of thickness Δz and volume $\Delta S \Delta z$	26
Figure 4 – Bloch sphere for a pure state given by $ \psi\rangle = \sin(\theta/2) 1\rangle + e^{i\phi} \cos(\theta/2) 2\rangle$. . .	30
Figure 5 – Population of the excited state for Rabi oscillations with detunings equal to 0 (exact resonance), Ω , and 2Ω	37
Figure 6 – Population of the excited state for damped Rabi oscillations with relaxation rates equal to 0 (exact resonance), $\Omega/2$, Ω , and 2Ω	38
Figure 7 – Damping coefficients a and b from equation (2.71) as a function of the detuning Δ for different Rabi frequencies Ω	39
Figure 8 – Oscillation frequency c from equation (2.71) in function of the detuning Δ for different Rabi frequencies Ω	39
Figure 9 – Energy uncertainty of a excited state whose lifetime is $1/\Gamma$. Due to the time-energy uncertainty principle, $\Delta E \geq \hbar\Gamma/2$ and then a spontaneously emitted photon have a random energy $\hbar\omega$ whose the average is $\hbar\omega_0$ and the uncertainty is greater than $\hbar\Gamma/2$	42
Figure 10 – Net absorption cross section as function of the detuning for some values of resonant saturation parameter.	43

Figure 11 – Representative illustration of the radiation pressure force as an average of scattering events. An atom initially with momentum \mathbf{p}_0 absorbs a photon with momentum $\hbar\mathbf{k}$ after a period $t_1 - t_0$. Then, at instant t_2 , this atom spontaneously emits a photon with momentum $\hbar\mathbf{k}'$ so that $ \mathbf{k} = \mathbf{k}' $. Finally, after successive absorption and emissions, the final momentum will be $\mathbf{p} \simeq \mathbf{p}_0 + N\hbar\mathbf{k}$ since the spontaneous emission is isotropic. The quantity N is the number of absorbed photons after a period $t_3 - t_0$. Therefore, the impulse after a period Δt will be $\Delta\mathbf{p} = \hbar\mathbf{k}R_{sc}\Delta t$, where R_{sc} is the rate at which the atom scatters photons. . . .	45
Figure 12 – Potential from gradient dipole force for few saturation parameters as a function of the laser detuning.	46
Figure 13 – Simplified one-dimensional MOT composed of two counter-propagating laser beams and a linear magnetic field $\mathbf{B} = B_0 z \mathbf{e}_z$, where $B_0 > 0$. We consider the σ_+ and σ_- beams right-handed and left-handed polarized respectively.	47
Figure 14 – Zeeman splitting of the transition $J = 0 \rightarrow J = 1$ in 1D-MOTs. When $\mathbf{B} = 0$ (\mathbf{B} off), the atomic transition $J = 0 \rightarrow J = 1$ is described by a degenerate two-level system . However, when $\mathbf{B} \neq 0$ (\mathbf{B} on), the same atomic transition is represented by a four-level system in which the excited states are energetically separated by the Zeeman shift $\delta_Z^{(\pm)}$. The energy scale was not plotted precisely to enhance the visibility. . . .	48
Figure 15 – Laser detuning, Doppler shift, and Zeeman shift of a 1D-MOT in function of velocity v and position z assuming red-detuned laser beams ($\delta < 0$).	49
Figure 16 – Breaking of a four-level system into three independent two-level systems.	50
Figure 17 – MOT force F_{MOT} for $v = 0$ ($z = 0$) as a function of $\beta z/\Gamma$ (kv/Γ) considering the transition $^1S_0 \rightarrow ^1P_1$ of the ^{88}Sr for $\delta = -\Gamma$ and $s_0 = 1$. The dashed line in the graph is the MOT force assuming $ \beta z \ll \delta $ ($ kv \ll \delta $).	51
Figure 18 – Standard arrangement of MOT composed of three orthogonal pairs of counter propagating laser beams with opposite circular polarization and coils in anti-Helmholtz configuration, which produces a magnetic quadrupole field.	52
Figure 19 – Measure of the full width at half maximum size of a rubidium atomic cloud along the magnetic coils axis. The three sets of data correspond to different MOT detunings. The solid line is a free fit of the data and the dashed line is fit considering the scaling model $L \propto N^{1/3}$	55
Figure 20 – Typical <i>in situ</i> absorption image of an atomic sample in a nMOT. . . .	56
Figure 21 – Forces diagram of a trapped atom in a power-broadened nMOT. . . .	58

Figure 22 – Basis $A' = \{\hat{\mathbf{x}}', \hat{\mathbf{y}}', \hat{\mathbf{z}}'\}$ of the magnetic field frame in relation to the basis $A = \{\hat{\mathbf{x}}, \hat{\mathbf{y}}, \hat{\mathbf{z}}\}$ of the laboratory frame.	61
Figure 23 – (a) Electronic transitions of spin-polarized dysprosium atoms and (b) laser beam arrangement and Helmholtz coils setup from the Dreon nMOT.	68
Figure 24 – (a) Estimated atomic cloud profile for different laser detunings based on equation (4.16). (b) In-situ atomic cloud profiles from the Dreon nMOT.	69
Figure 25 – The gravity direction component of the centre of mass as a function of the laser detuning. The blue spheres, orange triangles, and green squares are, respectively, the theoretical centres of mass from equation (3.20), estimated points, and experimental measures from (1).	70
Figure 26 – (a) Cloud sizes σ_y and σ_z and (b) cloud ratio σ_y/σ_z as a function of the laser detuning. The blue spheres and orange triangles are the estimated and experimental cloud sizes respectively.	71
Figure 27 – Temperature of the Dreon nMOT as a function of the laser detuning. The blue spheres and the orange triangles are the estimated and experimental temperatures respectively. We can roughly split the temperatures into two regions at the laser detuning $-6\Gamma' \simeq 7.5\Gamma$. For detunings lower than $6\Gamma'$ in module, the nMOT is not in the power-broadened regime and then present a divergence between experimental and estimated values.	72
Figure 28 – (a) Estimated atomic cloud profile for different laser detunings based on equation (4.16). (b) In-situ atomic cloud profiles from the Loftus nMOT.	74
Figure 29 – Centre of mass as a function of the laser detunings from the Loftus nMOT. The blue spheres, orange triangles, and black line are the estimated, experimental, and theoretical centre of mass respectively.	74
Figure 30 – Cloud sizes components from the Loftus nMOT as a function of the laser detuning. The blue spheres, orange triangles, and green squares are the estimated x , y , and z cloud size components respectively.	75
Figure 31 – (a) Temperature as a function of the laser detuning for a saturation parameter of $s = 102$. (b) Temperature as a function of the saturation parameter for a laser detuning of $\delta = -3.1 \text{ MHz}$. The blue spheres and orange triangles are the estimated and experimental values from the IFSC nMOT respectively.	76

LIST OF TABLES

Table 1	– Simulation parameters that defines the involved electronic transition and the mass of the atoms.	63
Table 2	– Simulation parameters that defines the magnetic field profile.	64
Table 3	– Simulation parameters that defines the laser beams arrangement.	64
Table 4	– Simulation performance parameters.	65
Table 5	– Parameters of the involved electronic transition from the Dreon nMOT.	67
Table 6	– Wave vector direction (x, y, z) and polarization $(\sigma_+, \sigma_-, \pi)$ in the laboratory frame (see Section 4.1.2) from Dreon nMOT. All laser beams are set up with the saturation parameter $s_0 = 0.65$ and waist 2.0 cm	69
Table 7	– Parameters that defined the magnetic field profile from Dreon nMOT.	69
Table 8	– Electronic transition parameters from the Loftus nMOT and the IFSC nMOT.	72
Table 9	– Wave vector direction (x, y, z) and polarization $(\sigma_+, \sigma_-, \pi)$ in the laboratory frame (see Section 4.1.2) from the Loftus nMOT and the IFSC nMOT. The laser beams of the Loftus nMOT have the saturation parameter $s_0 = 248$ and waist $w = 2.6 \text{ cm}$, whereas the laser beams of the IFSC nMOT have $s_0 = 102$ and $w = 6.0 \text{ cm}$	73
Table 10	– Parameters of the magnetic field profile from the Loftus nMOT.	73
Table 11	– Parameters of the magnetic field profile from the IFSC nMOT.	73

CONTENTS

1	INTRODUCTION	19
1.1	The thesis	20
2	ATOM-LIGHT INTERACTION	21
2.1	Rate equations model	21
2.1.1	Relation between the Einstein coefficients	22
2.1.2	Probabilistic analysis for single atoms	23
2.1.3	Spectral broadening	24
2.1.4	Monochromatic light field	25
2.1.5	Absorption cross section	26
2.2	Two-level atom interacting with classical light field	28
2.2.1	Two-level system and the Bloch sphere	28
2.2.2	Interaction Hamiltonian	30
2.2.3	Optical Bloch equations	32
2.2.4	Rabi oscillations	35
2.2.5	Rate-equation limit	40
2.2.6	Line-broadening mechanisms	41
2.2.7	Optical forces	43
3	MAGNETO-OPTICAL TRAP	47
3.1	One-dimensional model	47
3.1.1	Cooling and trapping effect	48
3.1.2	MOT Force	50
3.2	Three-dimensional case	52
3.2.1	Limit temperature in Doppler cooling	53
3.2.2	Atomic cloud size	54
3.2.3	Magnetic force	54
3.3	Narrow-line magneto-optical trap	56
3.3.1	Operating regimes	57
3.3.2	Centre of mass of the atomic cloud	57
4	MONTE CARLO SIMULATION	59
4.1	Stochastic evolution	59
4.1.1	Equilibrium	60
4.1.2	Magnetic field frame	60
4.1.3	Transition probabilities	62

4.2	Input and outputs	62
4.2.1	Input	63
4.2.2	Output	64
5	RESULTS	67
5.1	Dysprosium	67
5.1.1	Atomic cloud profile	68
5.1.2	Temperature	71
5.2	Strontium	71
5.2.1	Atomic cloud profile	73
5.2.2	Temperature	75
6	CONCLUSION	77
	REFERENCES	79
	APPENDIX A – DENSITY OPERATOR	83
A.0.1	Liouville equation	85
A.1	Decoherence	86
	APPENDIX B – SCATTERING CROSS SECTION	89
	APPENDIX C – SELECTION RULES	91

1 INTRODUCTION

The deep understanding of light-matter interaction brought several scientific possibilities such as improvements in the atom interferometry (2), accurate spectroscopic methods (3), and control of ultracold atoms. The Nobel Prize in Physics of 1997 was awarded jointly to Steven Chu (4), Claude Cohen-Tannoudji (5), and William D. Phillips (6) for developing methods to cool and trap atoms with laser light, also known as laser cooling (7). This achievement has enabled modern technologies, including accurate atomic clocks (8), qubits for quantum computing (9), and quantum sensors (10). Laser cooling also allowed the experimental confirmation of the Bose-Einstein condensation (BEC), motivating the Nobel Prize of Physics in 2001 (11,12).

The workhorse of laser cooling is the magneto-optical trap (MOT) (13), a technique to trap and cool a dilute atomic gas until temperatures in a range of μK . A standard MOT consists of three pairs of counter-propagating laser beams mutually orthogonal and a quadrupole magnetic field. Briefly, the atoms scatter photons from the laser light through atomic transitions, which cause momentum exchanges. The average momentum exchange yields a trapping and drag force on the atoms (MOT force). The frequency of these random scatterings increases with the atomic linewidth and defines the magnitude of both MOT force and its temperature. Overall, MOTs operating with narrow transitions reach lower temperatures at the cost of trapping efficiency. When the linewidth is comparable to the photonic recoil, we have the narrow line magneto-optical trap (nMOT) (14–16).

The currently theories of MOT based on Doppler cooling are limited to accurate predict experimental quantities such as temperature (17) and atomic cloud profile (18). In many experiments, there is either the absence of theoretical predictions or the necessity of adjustable scaling factors (19). Furthermore, most of these theories are restricted to an unfeasible one-dimensional MOT (7,20). The difficulty arises from the three-dimensional laser beams arrangement in the presence of a magnetic quadrupole field. The case of nMOTs is even more delicate since the gravity effect can be comparable to the optical forces and then must be included. This problem is often approach by computational solutions (21–23) that are capable of analysing MOTs qualitatively and quantitatively.

In this thesis, we propose a Monte Carlo simulation in order to predict experimental quantities of nMOTs. Our model relies on sampling the atoms' movement by assuming it is a discrete stochastic process. Then, we estimate the probability distributions of the atoms' position and velocity, which define the atomic cloud profile and the temperature. We could obtain estimated quantities that are more accurate than the theoretical predictions for three nMOT arrangements at different laboratories.

1.1 The thesis

In the framework of this thesis, we perform a deep study of atom-light interactions in Chapter 2. Firstly, in Section 2.1, we investigate the Einstein rate equations to get a start on the basic concepts. Although this approach is proper for an elementary understanding, it does not contemplate coherent effects such as Rabi oscillations or the nature of line broadening mechanisms. To take these phenomena into account, we introduce the optical Bloch equations in Section 2.2.3, which tackle the electronic transitions within quantum mechanics. Afterwards, we analyse mechanical effects by introducing optical forces in Section 2.2.7.

In Chapter 3, we introduce the theory of MOTs for electronic transitions $|J = 0\rangle \rightarrow |J = 1\rangle$ by analysing a simplified unidimensional model in Section 3.1. Then, we discuss the three-dimensional case in Section 3.2. We also analyse narrow-line MOTs and their three operating regimes in Section 3.3. In Chapter 4, we detailed our model to simulate the atoms' movement as a stochastic process and then estimate their position and velocity. We get through the parameters of the simulation and its output in Section 4.2. Finally, in Chapter 5, we present estimated quantities for three nMOT arrangements at different laboratories and then compare them with experimental measures and theoretical predictions.

2 ATOM-LIGHT INTERACTION

In this chapter, we review several aspects of atom-light interaction (24) to properly approach the atomic dynamics in magneto-optical traps. First of all, we shall explore the basic concepts through **the phenomenological Einstein rate equations** (25), a "semi-quantum" model where atoms absorb and emit light at a defined rate. Afterwards, we invoke the quantum mechanics apparatus through the **density operator** and the **master equation** (26) to analyze coherence effects and line broadening mechanisms. We thoroughly discuss the case of a two-level atom interacting with a monochromatic radiation through the semiclassical approach. Finally, we brief discuss conditions in which electric dipole transitions are allowed.

2.1 Rate equations model

A simple approach to introduce the essential aspects of atom-light interaction was proposed by Einstein in 1917. Although this theory does not take coherent effects into account, it is justified within the quantum mechanics framework in appropriate limits. Einstein assumed discrete energy levels for both atom and light. In this context, the electromagnetic radiation is composed of packets of energy $\hbar\omega$ and momentum $\hbar\omega/c$ known as photons, where ω is the angular frequency, $\hbar = h/2\pi$ is the reduced Planck constant, and c is the speed of light. Einstein also postulated phenomenological rate equations to describe two-level atomic transitions due to the absorption and emission of photons. Let us consider a two-level transition where the energy difference between the upper and lower level is $\hbar\omega_0$, and an electromagnetic radiation with spectral energy density $u(\omega)$. In Figure 1, we illustrated the three possible transitions involving absorption and emission of photons.

Let us consider a dilute atomic gas with number density $n_1(t)$ of atoms in the lower level and number density $n_2(t)$ of atoms in the upper level after a period of time t . The Einstein rate equations express the time evolution of n_1 and n_2 so that

$$\frac{dn_1}{dt} = -\frac{dn_2}{dt} = -B_{12}u(\omega_0)n_1 + B_{21}u(\omega_0)n_2 + An_2, \quad (2.1)$$

where $B_{12}u(\omega_0)$, $B_{21}u(\omega_0)$, and A are phenomenological rates associated with the stimulated absorption, stimulated emission and spontaneous emission respectively. The rates associated with stimulated processes are proportional to the spectral density energy and therefore these processes only happen in the presence of a light field.

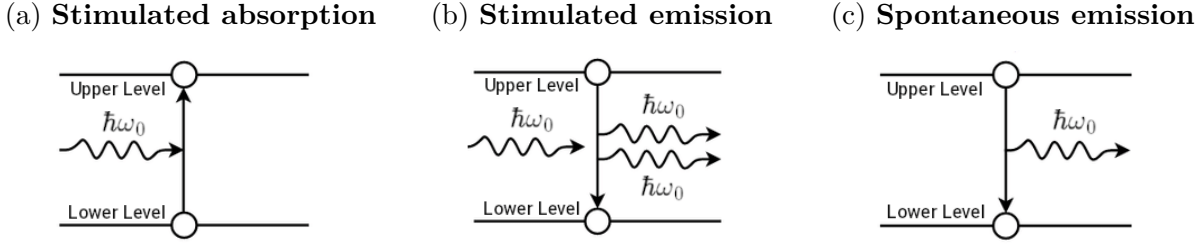


Figure 1 – Representative illustration of stimulated absorption and emission, and spontaneous emission. In figure (a), an atom in the lower level goes into the upper level absorbing a photon with energy $\hbar\omega_0$ from a light field with $u(\omega_0) > 0$. In figure (b), an atom in the upper level decays into the lower level in the presence of a light field with $u(\omega_0) > 0$, emitting a photon with energy $\hbar\omega_0$ similar to the photons in the light field. In figure (c), an atom in the upper level emits an isotropic photon with energy $\hbar\omega_0$ spontaneously, decaying into the lower level.

Source: By the author.

2.1.1 Relation between the Einstein coefficients

A dilute atomic gas at temperature T in thermal equilibrium establishes a steady state in which n_1 and n_2 are constants of time ($d_t n_1 = -d_t n_2 = 0$). In this condition, from equation (2.1), the spectral energy density is

$$u(\omega_0) = \frac{A}{(n_1/n_2)B_{12} - B_{21}}. \quad (2.2)$$

Considering a fixed number of atoms $n = n_1 + n_2$, the system are represented by the canonical ensemble and then the ratio n_1/n_2 is associated with the Boltzmann distribution so that

$$\frac{n_1}{n_2} = \frac{g_1}{g_2} \exp \left\{ -\frac{\hbar\omega_0}{k_B T} \right\}, \quad (2.3)$$

where g_1 and g_2 are the degeneracies of the lower and upper level, respectively, and k_B is the Boltzmann constant. Einstein evaluated atoms in a region of black body radiation, in which the spectral energy density of the light is consistent with the Planck distribution law given by

$$u(\omega_0) = \frac{\hbar\omega_0^3}{\pi^2 c^3} \frac{1}{e^{\hbar\omega_0/k_B T} - 1}. \quad (2.4)$$

Comparing (2.2), (2.3), and (2.4), we obtain

$$B \equiv B_{21} = \frac{g_1}{g_2} B_{12} \quad (2.5)$$

and

$$A = \frac{\hbar\omega_0^3}{\pi^2 c^3} B. \quad (2.6)$$

The Einstein coefficients are properties of the atoms. Thereby the equations (2.6) and (2.5) are valid for any electromagnetic radiation, from narrow bandwidth radiation to broadband light. If we know one of the three rate coefficients, we can always determine the other two.

It is worthwhile to compare the spontaneous emission rate A to the stimulated emission rate $Bu(\omega_0)$ considering the equations (2.4) and (2.6) so that

$$\frac{A}{Bu(\omega_0)} = e^{\hbar\omega_0/k_B T} - 1. \quad (2.7)$$

Spontaneous emission dominates for high frequencies (visible, UV, X-ray), $\hbar\omega_0 \gg k_B T$, but stimulated emission is more relevant for small frequencies (far IR, microwaves, radio waves).

2.1.2 Probabilistic analysis for single atoms

Previously, we consider the effect of the Einstein equations on an atomic sample. In this section, we shall analyze the effect of those equations on a single atom through the probability $P(t)$ of finding an atom in the upper level¹ after a period t ,

$$P(t) = \frac{n_2}{n_1 + n_2} = \frac{n_2(t)}{n}. \quad (2.8)$$

From now on, for simplicity, we shall consider non-degenerate atomic transitions ($g_1 = g_2 = 1$). We also shall call the lower level as *ground state* and the upper level as *excited state*. The probability distribution $\rho(t)$ of finding an atom in the excited state between the instants t and $t + dt$ is given by

$$\rho(t) = \frac{dP}{dt} = (1 - 2P)Bu(\omega_0) - AP, \quad (2.9)$$

where we consider (2.1), (2.8), and $1 - P = n_1/n$.

Let us analyze a system only subject to spontaneous emission, assuming an atom in the absence of light ($u(\omega) = 0$) initially in the excited state ($P(0) = 1$). From (2.9), we obtain

$$P(t) = e^{-At} \Rightarrow \rho(t) = Ae^{-At} \quad (2.10)$$

The equation (2.10) indicates an exponential decay, which means an atom in the excited state certainly goes into the ground state after a long period ($P(t) \rightarrow 0$). Therefore, we can interpret A as a *relaxation rate*. The average time τ in which an atom remains in the excited state, also known as *lifetime*, is given by

$$\tau = \int_0^\infty t\rho(t)dt = \int_0^\infty Ate^{-At}dt = \frac{1}{A} \Rightarrow A = \frac{1}{\tau}. \quad (2.11)$$

¹ Analogously, we can define the probability of finding an atom in the lower level.

In contrast, we can analyze the effect of stimulated processes considering $Bu(\omega_0) \gg A$. Let us assume an atom initially in the ground state ($P(0) = 0$). From equation (2.9), we obtain

$$P(t) = \frac{1 - e^{-\alpha t}}{2} \quad (2.12)$$

where $\alpha \equiv 2Bu(\omega_0)$ is the rate in which the radiation raises (or "pumps") atoms into the excited state due to stimulated process, also known as *pumping rate*. The equation (2.12) shows that the strong driving of a transition leads to its *saturation* ($P(t) \rightarrow 1/2$). In other words, the atomic ensemble goes into complete transparency.

Finally, let us assume an atom initially in the ground state subjected to the effect of both stimulated and spontaneous processes. In this situation, the solution of (2.9) is

$$P(t) = \frac{1/2}{1 + A/\alpha} (1 - e^{-(A+\alpha)t}) \quad (2.13)$$

The equation (2.13) also indicates a saturation so that

$$\lim_{t \rightarrow \infty} P(t) = \frac{1/2}{1 + A/\alpha}. \quad (2.14)$$

In the limits $A \gg \alpha$ and $A \ll \alpha$, we obtain $P(t) \rightarrow 0$ and $P(t) \rightarrow 1/2$, respectively. These results are expected from the previous analysis.

2.1.3 Spectral broadening

In the previous section, we assume that the emitted and absorbed photons have a single frequency ω_0 . In this case, the probability to absorb or emit a photon is a sharp line centered at $\omega = \omega_0$ as illustrated in figure 2a. However, in real situations, atoms can absorb and emit photons in a range of frequencies due to **line-broadening mechanisms** (section 2.2.6), which is illustrated in figure 2b.

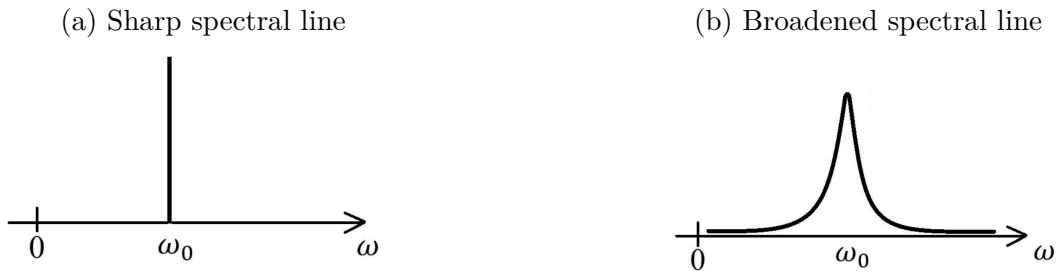


Figure 2 – Representative illustration of optical two-level transitions. In figure (a), it is represented the absorption or emission spectrum without line-broadening mechanisms so that we can assume the line shape $g(\omega) = \delta(\omega - \omega_0)$. In figure (b), it is represented the absorption or emission spectrum taking line-broadening mechanisms into account.

Source: VALVERDE; BASEIA; BAGNATO. (27)

We can take these mechanisms into account by introducing the normalized function g called **line shape function**. This function can be understood as the probability of absorbing or emitting a photon with frequency between ω and $\omega + d\omega$. A common g function in atomic spectroscopy is the *Lorentzian*² (Cauchy distribution) given by

$$g(\omega) = \frac{\Gamma'}{2\pi} \frac{1}{(\omega - \omega_0)^2 + (\Gamma'/2)^2} \quad \text{or} \quad g(\Delta) = \frac{\Gamma'}{2\pi} \frac{1}{\Delta^2 + (\Gamma'/2)^2}, \quad (2.15)$$

where $\Delta = \omega - \omega_0$ is the **detuning** and Γ' is the full width at half maximum (FWHM) also known as **spectral linewidth**. The main spectral linewidth is $\Gamma' = A$, which is related to the energy-time uncertainty principle. Thus,

$$g(\omega) = \frac{A}{2\pi} \frac{1}{(\omega - \omega_0)^2 + (A/2)^2} \quad \text{or} \quad g(\Delta) = \frac{A}{2\pi} \frac{1}{\Delta^2 + (A/2)^2}. \quad (2.16)$$

The probability distribution of finding an atom in the excited state taking the line shape function into account is given by

$$\rho(t) = (1 - 2P)B \int_0^\infty u(\omega)g(\omega)d\omega - AP. \quad (2.17)$$

For a broadband electromagnetic field, which means $u(\omega)$ much broader than $g(\omega)$, the equations (2.17) and (2.9) are equivalent because

$$\int_0^\infty u(\omega)g(\omega)d\omega \simeq u(\omega_0) \int_0^\infty g(\omega)d\omega = u(\omega_0). \quad (2.18)$$

2.1.4 Monochromatic light field

Let us consider a monochromatic electromagnetic field with frequency ω interacting with an atom initially in the ground state. In the case, the spectral intensity $I(\omega)$ and the spectral density energy $u(\omega)$ of the light field is $I(\omega') = cu(\omega') = I_0\delta(\omega' - \omega)$, where I_0 is the total intensity and $\delta(x)$ is the Dirac delta. Thus,

$$\int_0^\infty u(\omega')g(\omega')d\omega' = \frac{I_0}{c} \int_0^\infty g(\omega')\delta(\omega' - \omega)d\omega' = \frac{I_0}{c}g(\omega). \quad (2.19)$$

From equation (2.17) and (2.19), we obtain

$$\rho(t) = (1 - 2P)\frac{\alpha(\omega)}{2} - AP, \quad (2.20)$$

where $\alpha(\omega) = 2B(I_0/c)g(\omega)$ is the **pumping rate**. The stationary solution of (2.20) is given by

$$P(t) = \frac{1/2}{1 + A/\alpha(\omega)} = \frac{1}{2} \frac{s(\omega)}{1 + s(\omega)}, \quad (2.21)$$

² Some authors define this distribution as a function of the frequency ν instead of the angular frequency $\omega = 2\pi\nu$.

where $s(\omega) = \alpha(\omega)/A$ is the **saturation parameter**, which defines the balance between pumping and relaxation. From equation (2.6), we have

$$s(\omega) = \frac{2\pi^2 c^2}{\hbar \omega_0^3} I_0 g(\omega) = \frac{2\lambda_0^3}{hc} I_0 g(\omega) = \frac{I_0}{I_s} \frac{g(\omega)}{g(\omega_0)}, \quad \text{where } I_s \equiv \frac{\hbar \omega_0^3}{2\pi^2 c^2 g(\omega_0)}. \quad (2.22)$$

The intensity I_s is called **saturation intensity**. When $s(\omega) \gg 1$, stimulated processes are more significant than spontaneous emission, implying the saturation $P \rightarrow 1/2$. When $s(\omega) \ll 1$, relaxation processes are predominant. In this case, the atom will certainly decay to the ground state, $P \rightarrow 0$.

2.1.5 Absorption cross section

In atomic spectroscopic, it is common to analyse the attenuated or amplified light beam which passes through an atomic medium (28–30). Let us consider an electromagnetic beam with total spectral intensity $I(\omega, z)$ propagating in the z -direction. This radiation passes through an atomic ensemble with n_1 atoms per volume in the ground state and n_2 atoms per volume in the excited state, being attenuated or amplified in each slab of thickness Δz due to stimulated absorption, as illustrated in Figure 3.

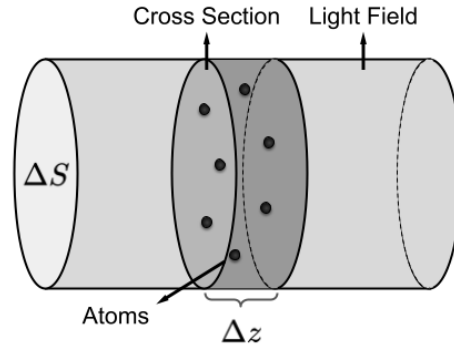


Figure 3 – Dilute atomic gas interacting with a electromagnetic radiation in a slab of thickness Δz and volume $\Delta S \Delta z$.

Source: By the author.

The spectral intensity will be reduced by a fraction of $n_1 \sigma(\omega) \Delta z$, where $\sigma(\omega)$, known as **absorption cross-section**³, is related to the probability that an atom will absorb a photon with angular frequency between ω and $\omega + d\omega$ from the light field on the section where this light passes on. Therefore, the lost spectral intensity is given $\Delta I/I = -N\sigma\Delta z$ and then

$$\frac{dI}{dz}(\omega, z) = -n_1 \sigma(\omega) I(\omega, z). \quad (2.23)$$

Besides the light attenuation due to stimulated absorption, there are also gain due to stimulated emission. Spontaneous emission does not contribute to the gain since the emitted

³ The absorption cross-section is expressed in units of area

light is isotropic. In this case, the light field will be amplified in each slab, increasing its intensity by a fraction of $n_2\sigma(\omega)\Delta z$. Here, the quantity σ gives the probability of emitting light stimulatory. The absorption cross-section and the emission cross-section are the same since the absorption rate equals the emission rate ($B_{12} = B_{21}$ when $g_1 = g_2$). Therefore, the light gain is given by

$$\frac{dI}{dz}(\omega, z) = n_2\sigma(\omega)I(\omega, z). \quad (2.24)$$

From equations (2.23) and (2.24), we obtain

$$\frac{dI}{dz}(\omega, z) = -(n_1 - n_2)\sigma(\omega)I(\omega, z) \quad (2.25)$$

where $(dI/dz)\Delta S\Delta z$ is equivalent to the net spectral power (power per unit of frequency) gained or lost by the radiation in a slab of thickness Δz due to stimulated processes⁴. It is convenient to define a **net absorption cross-section** as

$$\sigma_{abs}(\omega) = \frac{n_1 - n_2}{n}\sigma(\omega) = (1 - 2P)\sigma(\omega), \quad (2.26)$$

where $n = n_1 + n_2$ is the total density number and P is the probability of finding an atom in the excited state. This cross-section is associated with the probability of an atom attenuating or amplifying an incident light due to stimulated processes. Solving the differential equation (2.25), we obtain

$$I(\omega, z) = e^{-n\sigma_{abs}(\omega)z}I(\omega, 0), \quad (2.27)$$

In the regime of weak excitation such that $n_2 \ll n_1$, the total number density is approximately the number density of the atoms in the ground state $n \simeq n_1$ and then $\sigma_{abs}(\omega) \simeq \sigma(\omega)$.

Let us assume a *monochromatic* radiation whose frequency is ω such that $I(\omega', z) = I_0(z)\delta(\omega' - \omega)$ and $u(\omega', z) = I(\omega', z)/c$. In this case, integrating equation (2.25) over all frequencies, we obtain the total power per unit of volume gained or lost by the radiation

$$\frac{dI_0}{dz}(z) = -n\sigma_{abs}(\omega)I_0(z) \Rightarrow I_0(z) = I_0(0)e^{-n\sigma_{abs}(\omega)z}. \quad (2.28)$$

In the steady state, (dI_0/dz) equals the total power per unit of volume lost by spontaneous emission. Then, from equation (2.28), we have

$$n\sigma_{abs}(\omega)I_0 = An_2\hbar \int_0^\infty \omega g(\omega)d\omega. \quad (2.29)$$

Since ω_0 is much greater than the FWHM of $g(\omega)$ ⁵, thus

$$\int_0^\infty \omega g(\omega)d\omega \simeq \omega_0. \quad (2.30)$$

⁴ Spontaneous emitted light does not come back to the radiation field, since it is isotropic.

⁵ The line shape function must be normalized over 0 to ∞ , which demands that the peak frequency ω_0 of $g(\omega)$ must be much greater than its FWHM.

Then, from equation (2.29), we have

$$n\sigma_{abs}(\omega)I_0 = An_2\hbar\omega_0 \Rightarrow \sigma_{abs}(\omega) = \frac{\hbar\omega_0}{I_0}AP, \quad (2.31)$$

where $P = n_2/n$. Therefore, in the steady state, the *net absorption cross-section* can be understood as an area on which the photon flux of the incident beam passes through times the rate ΓP at which an atom scatters photons by spontaneous emission, i.e. the decay rate Γ times the probability of finding an atom in the excited state. From equations (2.21), (2.22), and (2.26), we obtain

$$\sigma(\omega) = \frac{\hbar\omega_0}{I_0} \frac{A}{2} s(\omega) = \frac{\overbrace{\hbar\omega_0 A}^{\sigma_0}}{I_s} \frac{g(\omega)}{2g(\omega_0)} = \sigma_0 \frac{g(\omega)}{g(\omega_0)} \quad \text{and} \quad (2.32)$$

$$\sigma_{abs}(\omega) = \frac{\hbar\omega_0}{I_0} \frac{A}{2} \frac{s(\omega)}{1+s(\omega)} = \sigma(\omega) \frac{1}{1+s(\omega)}, \quad (2.33)$$

where $\sigma_0 \equiv \sigma(\omega_0)$ is the *resonant absorption cross-section* which only depends on the properties of the atom (I_s , ω_0 , and A).

2.2 Two-level atom interacting with classical light field

In the previous section, we consider phenomenological rate equations to study two-level atomic transitions. This approach does not contemplate coherence effects nor a fundamental understanding of line broadening mechanisms. In a first attempt, we can take the coherence effects into account assuming the interaction between a classical light field (electromagnetic waves) and an atom whose internal states are described by a quantum state vector $|\psi\rangle$. Indeed, this is a proper treatment as long as we are only interested in stimulated processes. However, spontaneous emission comes from the interaction between atom and the vacuum modes of the quantized electromagnetic field, an incoherent relaxation process. Therefore, a single state vector is not sufficient to analyze an atom under both stimulated and spontaneous processes since such system is under decoherence. A proper description comes through the density operator (appendix A), which describes a statistical mixture of quantum states. This approach allows us to study the system time evolution taking both coherent and incoherent processes into account through a master equation.

2.2.1 Two-level system and the Bloch sphere

Let us consider a system composed of only two quantum states $|1\rangle$ and $|2\rangle$, in which $|1\rangle$ is the *ground state* and $|2\rangle$ is the excited state. An arbitrary two-dimensional density operator can be represent as

$$\hat{\rho} = \begin{bmatrix} \rho_{1,1} & \rho_{1,2} \\ \rho_{2,1} & \rho_{2,2} \end{bmatrix}, \quad (2.34)$$

where $\rho_{i,j} = \langle i|\hat{\rho}|j\rangle$. The diagonal terms represent probabilities so that $\rho_{1,1} + \rho_{2,2} = 1$, being $\rho_{1,1}$ and $\rho_{2,2}$ real values. Also, $\hat{\rho}$ must be hermitian and therefore $\rho_{1,2} = (\rho_{2,1})^*$. The density matrix (2.34) is represented on the basis

$$\left\{ \begin{bmatrix} 1 & 0 \\ 0 & 0 \end{bmatrix}, \begin{bmatrix} 0 & 1 \\ 0 & 0 \end{bmatrix}, \begin{bmatrix} 0 & 0 \\ 1 & 0 \end{bmatrix}, \begin{bmatrix} 0 & 0 \\ 0 & 1 \end{bmatrix} \right\}. \quad (2.35)$$

Another convenient basis is the **Pauli matrices basis**,

$$\left\{ \sigma_x = \begin{bmatrix} 0 & 1 \\ 1 & 0 \end{bmatrix}, \sigma_y = \begin{bmatrix} 0 & -i \\ i & 0 \end{bmatrix}, \sigma_z = \begin{bmatrix} 1 & 0 \\ 0 & -1 \end{bmatrix}, \mathbb{I}_2 = \begin{bmatrix} 1 & 0 \\ 0 & 1 \end{bmatrix} \right\}, \quad (2.36)$$

where σ_x , σ_y , and σ_z are the *Pauli matrices*. An arbitrary density matrix on this basis is written as⁶

$$\hat{\rho} = \frac{1}{2}(\mathbb{I}_2 + \mathbf{a} \cdot \vec{\sigma}) = \frac{1}{2} \begin{bmatrix} 1 + a_3 & a_1 - ia_2 \\ a_1 + ia_2 & 1 - a_3 \end{bmatrix}, \quad (2.37)$$

$$\text{where } \vec{\sigma} = \begin{bmatrix} \sigma_x \\ \sigma_y \\ \sigma_z \end{bmatrix} \text{ and } \mathbf{a} = \begin{bmatrix} a_1 \\ a_2 \\ a_3 \end{bmatrix} \text{ (**Bloch vector**).} \quad (2.38)$$

In this representation, its eigenvalues are $(1 \pm |\mathbf{a}|)/2$. Since they are probabilities, we must have $0 \leq (1 \pm |\mathbf{a}|)/2 \leq 1 \Rightarrow |\mathbf{a}| \leq 1$. For the same reason, the diagonal terms, and then a_3 , must be positive values. Furthermore, $\hat{\rho} = \hat{\rho}^\dagger$, which implies $a_1 = a_1^*$ and $a_2 = a_2^*$. Hence, \mathbf{a} is a real vector. Comparing with the density matrix (2.34), we have $a_3 = \rho_{1,1} - \rho_{2,2} = p$ and $(a_1 + ia_2)/2 = \rho_{2,1} = q$, where p is known as **population inversion** and q is the *coherence*. Then, the Bloch vector and the density matrix can be written as

$$\mathbf{a} = \begin{bmatrix} 2 \operatorname{Re}[q] \\ 2 \operatorname{Im}[q] \\ p \end{bmatrix} = \begin{bmatrix} q + q^* \\ i(q^* - q) \\ p \end{bmatrix} \text{ and } \hat{\rho} = \begin{bmatrix} (1+p)/2 & q^* \\ q & (1-p)/2 \end{bmatrix}. \quad (2.39)$$

Taking the property $|\mathbf{a}| \leq 1$ into account, we can represent the Bloch vector in a ball of unitary radius known as **Bloch sphere** (although it is a ball, not a sphere) illustrated in figure 4. The axes are given by $x = 2 \operatorname{Re}[q]$, $y = 2 \operatorname{Im}[q]$, and $z = p$. When $\hat{\rho}$ represent a pure state, we have

$$\operatorname{Tr}[\hat{\rho}^2] = 1 \Rightarrow \frac{1}{2}(1 + |\mathbf{a}|^2) = 1 \Rightarrow |\mathbf{a}|^2 = 1. \quad (2.40)$$

Therefore, the surface of the Bloch sphere represents all the pure states, whereas the inside corresponds to all the mixed states.

⁶ For an arbitrary operator, we should have four coefficients $[\hat{A}] = a_0\mathbb{I} + a_1\sigma_x + a_2\sigma_y + a_3\sigma_z$. In the case of the density matrix, we must have $a_0 = 1/2$ due to the property $\operatorname{Tr}[\hat{\rho}] = 1$.

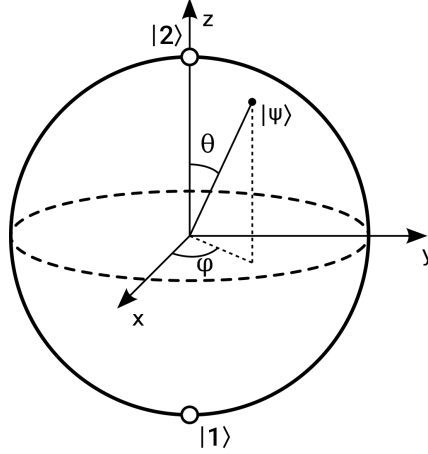


Figure 4 – Bloch sphere for a pure state given by $|\psi\rangle = \sin(\theta/2) |1\rangle + e^{i\phi} \cos(\theta/2) |2\rangle$.

Source: By the author.

Let us consider a pure state $|\psi\rangle = c_1 |1\rangle + c_2 |2\rangle$. Since a global phase is not measurable, we can assume $|\psi\rangle = c_1 |1\rangle + c_2 e^{i\phi} |2\rangle$ where ϕ is the phase difference between $|1\rangle$ and $|2\rangle$, and both c_1 and c_2 are real values. Moreover, $c_1^2 + c_2^2 = 1$, which allows us to associate c_1 and c_2 with a unique value θ considering $c_1 = \sin(\theta/2)$ and $c_2 = \cos(\theta/2)$. Even though the value of θ is not unique to represent c_1 and c_2 , the point (θ, ϕ) is unique to represent $|\psi\rangle$. Thus, a density operator $\hat{\rho} = |\psi\rangle\langle\psi|$ of a pure state can be written as

$$\begin{aligned} \hat{\rho} = & \sin^2(\theta/2) |1\rangle\langle 1| + \cos^2(\theta/2) |2\rangle\langle 2| + \\ & + \frac{1}{2} e^{-i\phi} \sin \theta |1\rangle\langle 2| + \frac{1}{2} e^{i\phi} \sin \theta |2\rangle\langle 1|, \end{aligned} \quad (2.41)$$

$$\hat{\rho} = \begin{bmatrix} \sin^2(\theta/2) & \frac{1}{2} e^{-i\phi} \sin \theta \\ \frac{1}{2} e^{i\phi} \sin \theta & \cos^2(\theta/2) \end{bmatrix}. \quad (2.42)$$

From equations (2.37) and (2.42), we obtain the following Bloch vector

$$\mathbf{a} = (\cos \phi \sin \theta, \sin \phi \sin \theta, \cos \theta), \quad (2.43)$$

in which (ϕ, θ) are *spherical coordinates* represented in figure 4.

2.2.2 Interaction Hamiltonian

Let us consider a system formed by only two electronic states $\{|1\rangle, |2\rangle\}$ ⁷, each one is a possible state of a valence electron in an atom. This system is well described by the density operator $\hat{\rho}$ given by (2.39). The dynamics of these states in the absence of a light

⁷ Actually, there are many electronic states which can be relevant. However, in many cases, only two states are enough to describe the interaction.

field is given by the following Hamiltonian

$$\hat{H}_0 = \hbar\omega_1 |1\rangle\langle 1| + \hbar\omega_2 |2\rangle\langle 2| = \hbar\omega_1 \hat{\sigma} \hat{\sigma}^\dagger + \hbar\omega_2 \hat{\sigma} \hat{\sigma}^\dagger, \quad (2.44)$$

where $\hat{\sigma} \equiv |1\rangle\langle 2|$ and $\omega_1 < \omega_2$. The lowest energy state $|1\rangle$ is called *ground state*, whereas the highest energy state $|2\rangle$ is called *excited state*. Since we are only concern with energy differences, we can shift the zero of energy adding $-\hbar\omega_1$ to each energy level so that

$$\hat{H}_0 = \hbar\omega_0 \hat{\sigma}^\dagger \hat{\sigma} = \begin{bmatrix} 0 & 0 \\ 0 & \hbar\omega_0 \end{bmatrix}, \quad (2.45)$$

where $\omega_0 = \omega_2 - \omega_1$ is the **resonant frequency**. The matrix in the equation (2.45) and also further matrix are represented on the basis $\{|1\rangle, |2\rangle\}$. Moreover, we shall assume a monochromatic radiation whose *electric field* \mathbf{E} is given by

$$\mathbf{E}(\mathbf{r}, t) = \frac{\vec{\epsilon}}{2} (E_0 e^{i\mathbf{k}\cdot\mathbf{r} - i\omega t} + E_0^* e^{-(i\mathbf{k}\cdot\mathbf{r} - i\omega t)}), \quad (2.46)$$

where $\vec{\epsilon} = (\vec{\epsilon})^*$ is the *polarization vector*, E_0 is the *complex amplitude*, \mathbf{k} is the *wave vector*, ω is the *angular frequency*, and \mathbf{r} is the *position vector*. The interaction between the electric field \mathbf{E} and the *electric dipole* formed by the valence electron and the atomic nucleus is the major atom-light interaction described by the following Hamiltonian

$$\hat{V} = -\mathbf{d} \cdot \mathbf{E}, \quad (2.47)$$

where $\mathbf{d} = -e\mathbf{r}_e$ is the **dipole operator**, $e \simeq 1.6 \times 10^{-19}C$ is the elementary charge, and \mathbf{r}_e is the valence electron position in the nucleus frame. The typical values of $|\vec{\mu}|$ are around ea_B ⁸, where $a_B = 0.529\text{\AA} = 0.529 \cdot 10^{-10}m$ is the *Bohr radius*. Atoms do not have permanent dipole moment due to the parity of the electrons position. Hence, the dipole operator can be written as⁹

$$\mathbf{d} = (\vec{\mu})^* \hat{\sigma} + \vec{\mu} \hat{\sigma}^\dagger, \quad (2.48)$$

where $\vec{\mu} \equiv \langle 2|\mathbf{d}|1\rangle$ is the **transition dipole moment**. When $|\vec{\mu}| = 0$, the transition is said to be **dipole forbidden**. Then, from equations (2.46), (2.48), and (2.47), we obtain the following interaction Hamiltonian

$$\hat{V}(t) = \frac{\hbar}{2} [(\tilde{\Omega}^*(\mathbf{r})e^{-i\omega t} + \Omega^*(\mathbf{r})e^{i\omega t})\hat{\sigma} + (\Omega(\mathbf{r})e^{-i\omega t} + \tilde{\Omega}(\mathbf{r})e^{i\omega t})\hat{\sigma}^\dagger], \quad (2.49)$$

$$\Omega(\mathbf{r}) \equiv -\frac{E_0(\vec{\epsilon} \cdot \vec{\mu})}{\hbar} e^{i\mathbf{k}\cdot\mathbf{r}} \text{ and } \tilde{\Omega}(\mathbf{r}) \equiv -\frac{E_0^*(\vec{\epsilon} \cdot \vec{\mu})}{\hbar} e^{-i\mathbf{k}\cdot\mathbf{r}}, \quad (2.50)$$

⁸ The *debye* (symbol D) is a standard unit measure for electric dipole moment in the atomic and molecular scale, $1D \equiv 10^{-18} \text{statC} \cdot \text{cm}$. Historically, the debye was defined as the dipole moment of a system composed of two electric charges of opposite sign and equal magnitude $10^{-10} \text{statC} \simeq 0.2083e$ separated by 1\AA .

⁹ We are assuming $\langle 1|\mathbf{d}|1\rangle = \langle 2|\mathbf{d}|2\rangle = 0$.

where $\Omega(\mathbf{r})$ and $\tilde{\Omega}(\mathbf{r})$ are known as **Rabi frequencies**¹⁰.

The minimum wavelength of non-ionizing radiation, which is the typical spectral range in laser cooling experiments, is around $100nm = 1000\text{\AA}$, whereas the atomic size is around the Bohr radius $a_B \simeq 0.5\text{\AA}$. Then, atoms are approximately thousand times smaller than the field spatial variation. Hence, assuming a quasi-static atom, we can neglect the spatial variation of the electromagnetic field in the dynamics of the electronic states. In this case, the Rabi frequency is approximately spatial-independent $\Omega(\mathbf{r}) \simeq \Omega$, which is known as **dipole approximation**.

The typical values of $|\Omega|$ are around MHz, whereas the typical atomic resonant frequencies are around 100THz. Thereby $\hat{V} \sim \hbar|\Omega| \ll \hbar\omega_0$, which allows us to treat the interaction as a perturbation on the system. In the *Dirac picture*, also called *interaction picture*, considering $\hat{U} = e^{-i\hat{H}_0 t/\hbar} = \hat{\sigma}\hat{\sigma}^\dagger + e^{-i\omega_0 t}\hat{\sigma}^\dagger\hat{\sigma}$, we have

$$\tilde{V}(t) = \hat{U}^\dagger \hat{V} \hat{U} = \tilde{V}_{fast}(t) + \tilde{V}_{slow}(t), \quad (2.51)$$

$$\tilde{V}_{fast}(t) = \frac{\hbar}{2}(\tilde{\Omega}^* e^{-i(\omega+\omega_0)t} \hat{\sigma} + \tilde{\Omega} e^{i(\omega+\omega_0)t} \hat{\sigma}^\dagger), \quad (2.52)$$

$$\tilde{V}_{slow}(t) = \frac{\hbar}{2}(\Omega e^{-i\Delta t} \hat{\sigma}^\dagger + \Omega^* e^{i\Delta t} \hat{\sigma}), \quad (2.53)$$

where $\Delta = \omega - \omega_0$ is the *laser detuning* and the *tilde* notation indicates the operators in the interaction picture. The interaction Hamiltonian \tilde{V}_{fast} oscillates much faster than \tilde{V}_{slow} since $\Delta \ll \omega + \omega_0$ and $\omega_0 \gg 0$ ($\omega_0 \sim 100\text{THz}$). To verify the effect of both interactions, let us calculate the transition amplitude $a_{1 \rightarrow 2}(t)$ from state $|1\rangle$ to state $|2\rangle$ through *time-dependent perturbation theory*,

$$a_{1 \rightarrow 2}(t) = \frac{1}{i\hbar} \int_0^t \langle 2 | \tilde{V}(t') | 1 \rangle dt' = \quad (2.54)$$

$$= \frac{1}{i\hbar} \left[\int_0^t \langle 2 | \tilde{V}_{fast}(t') | 1 \rangle dt' + \int_0^t \langle 2 | \tilde{V}_{slow}(t') | 1 \rangle dt' \right] = \quad (2.55)$$

$$= \frac{\tilde{\Omega}}{2(\omega + \omega_0)} (e^{i(\omega - \omega_0)t} - 1) + \frac{\Omega}{2\Delta} (e^{-i\Delta t} - 1). \quad (2.56)$$

We can neglect the terms with $\tilde{\Omega}$ since $\Delta \ll \omega + \omega_0$ in equation (2.56). In other words, we can neglect the \tilde{V}_{fast} such that $\tilde{V} \simeq \tilde{V}_{slow}$, which is called **rotating-wave approximation**.

2.2.3 Optical Bloch equations

Let us consider the unitary transformation $\hat{U}_{rot} = \hat{\sigma}\hat{\sigma}^\dagger + \hat{\sigma}^\dagger\hat{\sigma}e^{-i\Delta t}$ into the *rotating frame* aiming to eliminate the time-dependence in equation the interaction Hamiltonian

¹⁰ Both Ω and $\tilde{\Omega}$ have the same amplitude $|\Omega| = |\tilde{\Omega}|$ but different phases.

(2.49) in the rotating wave approximation so that

$$\tilde{V}' = \hat{U}_{rot}^\dagger \tilde{V} \hat{U}_{rot} + i\hbar(\partial_t \hat{U}_{rot}^\dagger) \hat{U}_{rot} = \frac{\hbar}{2} \begin{bmatrix} 0 & \Omega^* \\ \Omega & -2\Delta \end{bmatrix}. \quad (2.57)$$

Then, applying the unitary transformations to the interaction picture and rotating frame in the density operator $\hat{\rho}$ as well, we obtain the density operator $\tilde{\rho}'$ given by

$$\tilde{\rho}' = \begin{bmatrix} (1+p)/2 & q^* e^{-i\omega t} \\ q e^{i\omega t} & (1-p)/2 \end{bmatrix}. \quad (2.58)$$

From equations (2.39) and (2.58), we can see that $\hat{\rho}$ and $\tilde{\rho}'$ are pretty similar. The only difference are the coherences, which gain an additional phase factor $e^{i\omega t}$ after the transformations. Then, by simplicity, we shall assume $q' = q e^{i\omega t}$.

The master equation (A.29) for our system is given by

$$\partial_t \tilde{\rho}' = -\frac{i}{\hbar} [\tilde{V}', \tilde{\rho}'] + \frac{\Gamma}{2} (2\hat{\sigma} \tilde{\rho}' \hat{\sigma}^\dagger - \{\hat{\sigma}^\dagger \hat{\sigma}, \tilde{\rho}'\}), \quad (2.59)$$

where Γ is a decay rate associated with spontaneous emission. By simplicity, let us assume Ω a positive real value, since any phase of Ω can be incorporate in the coherence q . From now on, we shall consider $q' \rightarrow q$ and $\rho'_{1,2} \rightarrow \rho_{1,2}$ to simplify the notation, keeping in mind that p and q are evaluated on the rotating frame and in the interaction picture. Thus, evaluating the matrix elements of $\partial_t \tilde{\rho}'$, we obtain

$$\partial_t \rho_{1,1} = -\Omega \text{Im}[\rho_{1,2}] + \Gamma \rho_{2,2} \quad (2.60)$$

$$\partial_t \rho_{2,2} = \Omega \text{Im}[\rho_{1,2}] - \Gamma \rho_{2,2} \quad (2.61)$$

$$\partial_t \rho_{1,2} = -(\Gamma/2 - i\Delta) \rho_{1,2} + i\Omega(\rho_{1,1} - \rho_{2,2})/2 \quad (2.62)$$

$$\partial_t \rho_{2,1} = -(\Gamma/2 + i\Delta) \rho_{2,1} - i\Omega(\rho_{1,1} - \rho_{2,2})/2, \quad (2.63)$$

where $\rho_{2,1} = (\rho_{1,2})^*$ and $\rho_{1,1} + \rho_{2,2} = 1$. The equations (2.60), (2.61), (2.62), and (2.63) are known as **optical Bloch equations** (OBEs). We can represent these equations in a convenient form through the *Bloch vector* $\mathbf{a}(t)$ given by equation (2.38), so that

$$\partial_t \mathbf{a}(t) = \mathcal{M} \mathbf{a}(t) + \mathbf{b}, \quad (2.64)$$

$$\mathcal{M} = \begin{bmatrix} -\Gamma/2 & -\Delta & 0 \\ \Delta & -\Gamma/2 & -\Omega \\ 0 & \Omega & -\Gamma \end{bmatrix}, \quad \mathbf{b} = \begin{bmatrix} 0 \\ 0 \\ \Gamma \end{bmatrix}, \quad \mathbf{a}(t) = \begin{bmatrix} 2 \text{Re}[q(t)] \\ 2 \text{Im}[q(t)] \\ p(t) \end{bmatrix}. \quad (2.65)$$

It is labour to solve the equation (2.64) for a general case. *H. C. Torrey* (31) deduced a general form using the *Laplace transformation* but he only obtain exact solutions for the cases of exact resonance $\Delta = 0$ and strong excitation so that $\Omega \gg \Gamma$. We shall pursue the solution of the OBEs from a different approach based upon the calculation of *eigenvalues* and *eigenvectors*.

Considering the vector $\vec{\xi}(t) = \mathbf{a}(t) + \mathcal{M}^{-1}$, where \mathcal{M}^{-1} is the inverse¹¹ of \mathbf{M} , we can rewrite the equation (2.64) so that

$$\partial_t \vec{\xi}(t) = \mathcal{M} \vec{\xi}. \quad (2.66)$$

The equation (2.66) is similar to the Schrodinger equation, $\hat{H}|\psi\rangle = i\hbar\partial_t|\psi\rangle$. Then, since \mathcal{M} is time-independent, we can consider a time evolution given by

$$\vec{\xi}(t) = \sum_{i=1}^3 c_i e^{m_i t} \vec{\chi}_i = \begin{bmatrix} \xi_1 \\ \xi_2 \\ \xi_3 \end{bmatrix} = \begin{bmatrix} 2 \operatorname{Re}[q_\xi(t)] \\ 2 \operatorname{Im}[q_\xi(t)] \\ p_\xi \end{bmatrix}, \quad (2.67)$$

where m_1 , m_2 , and m_3 are *eigenvalues*¹², $\vec{\chi}_1$, $\vec{\chi}_2$, and $\vec{\chi}_3$ are *eigenvectors*, and c_1 , c_2 , and c_3 are constants ($\partial_t c_i = 0$) which depend on the initial conditions. The eigenvalues are roots of the *characteristic polynomial* given by

$$P(m) = -\det(\mathcal{M} - m\mathbb{I}) \quad (2.68)$$

$$= (\Gamma/2 + m)^2(\Gamma + m) + \Omega^2(\Gamma/2 + m) + \Delta^2(\Gamma + m). \quad (2.69)$$

Since $P(m)$ is a *cubic polynomial* with real coefficients, at least one root is real and the other two are complex conjugate of each other. By the *Routh-Hurwitz criterion*¹³, all real parts of the roots are negative numbers. Therefore, the eigenvalues can be written as

$$m_1 = -a, \quad m_2 = -b + ic, \quad \text{and} \quad m_3 = -b - ic, \quad (2.70)$$

where a , b , and c are real values, being a and b positive numbers. Thus, plugging (2.70) in (2.66), we obtain the general solution given by

$$a_i(t) = A_i e^{-at} + e^{-bt} [B_i \cos(ct) + C_i \sin(ct)] + a_i(\infty), \quad \text{for } i \in \{1, 2, 3\}, \quad (2.71)$$

where a_1 , a_2 , and a_3 are components of the Bloch vector \mathbf{a} and A_i , B_i , and C_i are complex constants that depend on the initial conditions and the eigenvectors $\vec{\chi}_i$. The first term of (2.71) represents exponential decays of the populations and coherences, which come from the relaxation due to the spontaneous emission. The second and third terms are associated with damped oscillations known as **Rabi oscillations** or **Rabi flopping**. The last term is a **stationary** solution in which any oscillation vanishes.

After a while, the system will reach a **steady-state** $\mathbf{a}(\infty)$ as shown in equation (2.71). This solution comes straightforwardly from equation (2.64) assuming $\partial_t \mathbf{a}(\infty) = 0$ such that

$$\mathcal{M} \mathbf{a}(\infty) + \mathbf{b} = 0 \Rightarrow \mathbf{a}(\infty) = -\mathcal{M}^{-1} \mathbf{b}, \quad (2.72)$$

¹¹ We are assuming $\det \mathcal{M} \neq 0$, which is a requirement to exist the inverse of \mathcal{M} .

¹² Since \mathcal{M} is not hermitian, its eigenvalues can be complex numbers.

¹³ Given a cubic polynomial $f(x) = c_0 + c_1 x + c_2 x^2 + x^3$, if c_0 , c_1 , and c_2 are positive and $c_2 c_1 > c_0$, then all roots have negative real parts.

where \mathcal{M}^{-1} is the inverse of \mathcal{M} given by

$$\mathcal{M}^{-1} = \frac{\text{adj}\mathcal{M}}{\det\mathcal{M}}, \quad \det\mathcal{M} = -\Gamma(\Gamma^2/4 + \Omega^2/2 + \Delta^2) \quad (2.73)$$

$$\text{adj}\mathcal{M} = \begin{bmatrix} \Gamma^2/2 + \Omega^2 & -\Delta\Gamma & \Delta\Omega \\ \Delta\Gamma & \Gamma^2/2 & -\Omega\Gamma/2 \\ \Delta\Omega & \Omega\Gamma/2 & \Gamma^2/4 + \Delta^2 \end{bmatrix}, \quad (2.74)$$

where $\text{adj}\mathcal{M}$ and $\det\mathcal{M}$ are the *adjugate*¹⁴ and the *determinant* of \mathcal{M} respectively. Thus, the **stationary solution** is given by

$$\mathbf{a}(\infty) = \frac{1}{\Gamma^2/4 + \Omega^2/2 + \Delta^2} \begin{bmatrix} \Delta\Omega \\ -\Omega\Gamma/2 \\ \Delta^2 + \Gamma^2/4 \end{bmatrix} = \begin{bmatrix} 2\text{Re}[q'] \\ 2\text{Im}[q'] \\ p \end{bmatrix} = \begin{bmatrix} 2\text{Re}[qe^{i\omega t}] \\ 2\text{Im}[qe^{i\omega t}] \\ p \end{bmatrix}, \quad (2.75)$$

$$p(\infty) = \frac{\Delta^2 + \Gamma^2/4}{\Delta^2 + \Omega^2/2 + \Gamma^2/4} \quad \text{and} \quad (2.76)$$

$$q(\infty) = \frac{\Omega}{2} \frac{\Delta - i(\Gamma/2)}{\Delta^2 + \Omega^2/2 + \Gamma^2/4} \quad (2.77)$$

From equation (2.76), the population of the excited state is given by

$$\rho_{2,2}(\infty) = \frac{1}{2} \frac{\Omega^2/2}{\Delta^2 + \Omega^2/2 + \Gamma^2/4}. \quad (2.78)$$

For strong excitation such that $\Omega^2 \gg 2\Delta^2 + \Gamma^2/2$, the population inversion saturates $p(\infty) \rightarrow 0$ as well as the population of the excited state $\rho_{2,2} \rightarrow 1/2$. For weak excitation such that $\Omega^2 \ll 2\Delta^2 + \Gamma^2/2$, $p(\infty) \rightarrow 1$ and then $\rho_{2,2} \rightarrow 0$.

2.2.4 Rabi oscillations

The Rabi oscillations occur during the transient to the steady-state as shown in equation (2.71). They are fully associated with the *coherent evolution* given by the term $[\hat{H}, \hat{\rho}]$ in the master equation (2.59). These oscillations are damped by spontaneous emission, which is an incoherent process. Then, to clearly approach this effect, let us assume a system under strong excitation $\Omega \gg \Gamma$ so that spontaneous emission can be neglected over a considerable period t . In this case, $\vec{\xi}(t) \simeq \mathbf{a}(t)$ in equation (2.67) since $\mathcal{M}^{-1}\mathbf{b} \simeq 0$. The characteristic polynomial (2.69) and its roots are given by

$$P(m) = m(m^2 + |\Omega|^2 + \Delta^2) \Rightarrow m_1 = 0, \quad m_2 = -iG, \quad m_3 = iG, \quad (2.79)$$

where $G \equiv \sqrt{|\Omega|^2 + \Delta^2}$ is the **generalized Rabi frequency**. Plugging the values (2.79) in $\mathcal{M}\vec{\chi}_i = m_i\vec{\chi}_i$, we obtain the following eigenvectors

$$\vec{\chi}_1 = \begin{bmatrix} 1 \\ 0 \\ \Delta/\Omega \end{bmatrix}, \quad \vec{\chi}_2 = \begin{bmatrix} \Delta/\Omega \\ i(G/\Omega) \\ -1 \end{bmatrix}, \quad \vec{\chi}_3 = \begin{bmatrix} -\Delta/\Omega \\ i(G/\Omega) \\ 1 \end{bmatrix}. \quad (2.80)$$

¹⁴ The adjugate of a matrix is the transpose of its cofactor matrix.

Let us assume an atom initially in the ground state so that $p(0) = 1$ and $q(0) = 0$. Then, from equations (2.67) and (2.80), we obtain

$$\mathbf{a}(0) = \begin{bmatrix} 0 \\ 0 \\ 1 \end{bmatrix} = c_1 \begin{bmatrix} 1 \\ 0 \\ \Delta/\Omega \end{bmatrix} + c_2 \begin{bmatrix} \Delta/\Omega \\ i(G/\Omega) \\ -1 \end{bmatrix} + c_3 \begin{bmatrix} -\Delta/\Omega \\ i(G/\Omega) \\ 1 \end{bmatrix}. \quad (2.81)$$

Solving the system (2.81) of linear equations, we obtain

$$c_1 = \frac{\Delta\Omega}{G^2} \quad \text{and} \quad c_2 = -c_3 = -\frac{\Omega^2}{2G^2}. \quad (2.82)$$

Plugging the values (2.79), (2.80) and (2.82) in (2.67), we obtain

$$p(t) = \frac{\Omega^2}{G^2} \left[\frac{\Delta^2}{\Omega^2} + \cos(Gt) \right] \quad \text{and} \quad (2.83)$$

$$q(t) = \frac{\Omega}{2G^2} [\Delta(1 - \cos(Gt)) - iG \sin(Gt)]. \quad (2.84)$$

Finally, from equation (2.83), the population of the excited state is given by

$$\rho_{2,2}(t) = \frac{1 + p(t)}{2} = \frac{\Omega^2}{2G^2} [1 - \cos(Gt)]. \quad (2.85)$$

In the exact resonance $\Delta = 0$,

$$p(t) = \cos(\Omega t) \quad (2.86)$$

$$q(t) = i \sin(\Omega t). \quad (2.87)$$

Equation (2.85) reveals oscillations between the ground and excited states at frequency G and period $T = 2\pi/G$. This phenomenon is called **Rabi oscillations** or **Rabi flopping**. Roughly, the ups and downs can be seen as absorptions and stimulated emissions respectively. Furthermore, the amplitude of the oscillations is given

$$\frac{\Omega^2}{G^2} = \frac{\Omega^2}{\Omega^2 + \Delta^2} = \frac{1}{1 + (\Delta/\Omega)^2}, \quad (2.88)$$

which has the maximum 1 when $\Delta = 0$, decreasing with Δ/Ω . Figure 5 illustrates the Rabi oscillations for a few detunings.

In the exact resonance given by the equations (2.86) and (2.87), the period is $T = 2\pi/\Omega$. If a field is turned on at $t = 0$ and then turned off after $t = T/2$, an atom initially in the ground state will be certainly promoted to the excited state. Such pulse is called **π -pulse**. Furthermore, if a field is turned on for a duration $T/4$, an atom initially in the ground state ends up in a superposition between the excited and ground states, which is called **$\pi/2$ -pulse**. This is widely used in atomic clocks and quantum computation, beyond the scope of this thesis.

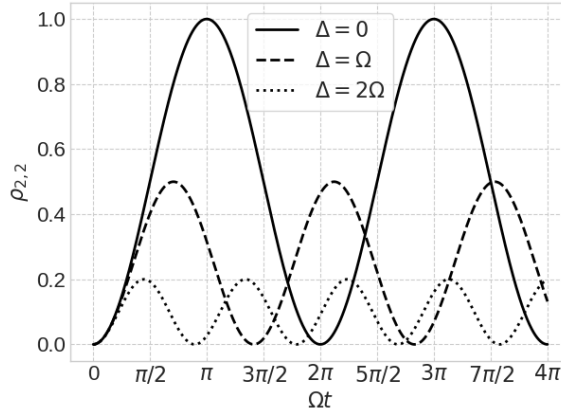


Figure 5 – Population of the excited state for Rabi oscillations with detunings equal to 0 (exact resonance), Ω , and 2Ω .

Source: By the author.

When spontaneous emission is consirable, the Rabi oscillations will be damped by them so that, after a while, the system will reach the steady-state given by (2.76) and (2.77). To get some insight into the damping oscillations, let us analyze the case of exact resonance $\Delta = 0$, which has a friendly exact solution. Afterwards, we perform numerical calculations to evaluate the dependence of the damping coefficients a and b , and the oscillation frequency c in (2.71) with the parameters Ω , Δ , and Γ .

In the exact resonance case $\Delta = 0$, the roots of the characteristic polynomial (2.69) have a friendly form given by

$$m_1 = -\frac{\Gamma}{2}, \quad m_2 = -\left(\frac{3\Gamma}{4} + i\Omega_\Gamma\right), \quad m_3 = -\left(\frac{3\Gamma}{4} - i\Omega_\Gamma\right), \quad (2.89)$$

where $\Omega_\Gamma \equiv \sqrt{\Omega^2 - (\Gamma/4)^2}$ is the Rabi oscillations frequency in the presence of damping. Plugging these eigenvalues in $\mathcal{M}\vec{\chi}_i = m_i\vec{\chi}_i$, we obtain the following eigenvectors

$$\vec{\chi}_1 = \begin{bmatrix} 1 \\ 0 \\ 0 \end{bmatrix}, \quad \vec{\chi}_2 = \begin{bmatrix} 0 \\ 1 \\ e^{i\theta} \end{bmatrix}, \quad \vec{\chi}_3 = \begin{bmatrix} 0 \\ 1 \\ e^{-i\theta} \end{bmatrix}, \quad (2.90)$$

where $\tan \theta = 4\Omega_\Gamma/\Gamma$. Again, let us consider an atom initially in the ground state so that

$$\vec{\xi}(0) = \mathbf{a}(0) - \mathbf{a}(\infty) = \begin{bmatrix} 0 \\ 0 \\ 1 \end{bmatrix} - \begin{bmatrix} 2 \operatorname{Re}[q(\infty)] \\ 2 \operatorname{Im}[q(\infty)] \\ p(\infty) \end{bmatrix} = (1 - p(\infty)) \begin{bmatrix} 0 \\ \Gamma/\Omega \\ 1 \end{bmatrix}. \quad (2.91)$$

Thus, plugging the values (2.89) and (2.90) in (2.67) and assuming the initial conditions (2.91), we obtain

$$c_1 \begin{bmatrix} 1 \\ 0 \\ 0 \end{bmatrix} + c_2 \begin{bmatrix} 0 \\ 1 \\ e^{i\theta} \end{bmatrix} + c_3 \begin{bmatrix} 0 \\ 1 \\ e^{-i\theta} \end{bmatrix} = (1 - p(\infty)) \begin{bmatrix} 0 \\ \Gamma/\Omega \\ 1 \end{bmatrix}, \quad (2.92)$$

which is a system of linear equations. After some algebra, the solution of (2.92) is

$$c_1 = 0, \quad c_2 = c_3^* = \left[\frac{\Gamma}{2\Omega} - i \frac{\Omega^2 - \Gamma^2/4}{2\Omega\Omega_\Gamma} \right] (1 - p(\infty)). \quad (2.93)$$

Then, we plug (2.93), (2.89), and (2.90) in (2.67), obtaining

$$p_\xi(t) = e^{-3\Gamma t/4} (1 - p(\infty)) \left[\cos(\Omega_\Gamma t) + \frac{3\Gamma}{4\Omega_\Gamma} \sin(\Omega_\Gamma t) \right] \quad \text{and} \quad (2.94)$$

$$q_\xi(t) = i e^{-3\Gamma t/4} (1 - p(\infty)) \frac{\Gamma}{2\Omega} \left[\cos(\Omega_\Gamma t) - \frac{\Omega^2 - \Gamma^2/4}{\Gamma\Omega_\Gamma} \sin(\Omega_\Gamma t) \right]. \quad (2.95)$$

Finally, plugging the equations (2.94) and (2.95) in $\mathbf{a}(t) = \vec{\xi}(t) + \mathbf{a}(\infty)$, we obtain

$$p(t) = e^{-3\Gamma t/4} (1 - p(\infty)) \left[\cos(\Omega_\Gamma t) + \frac{3\Gamma}{4\Omega_\Gamma} \sin(\Omega_\Gamma t) \right] + p(\infty) \quad \text{and} \quad (2.96)$$

$$q(t) = i(1 - p(\infty)) \frac{\Gamma}{2\Omega} \left\{ e^{-3\Gamma t/4} \left[\cos(\Omega_\Gamma t) - \frac{\Omega^2 - \Gamma^2/4}{\Gamma\Omega_\Gamma} \sin(\Omega_\Gamma t) \right] - 1 \right\}. \quad (2.97)$$

The equation (2.96) shows a *damped oscillation* illustrated in figure 6. The damping effect is as strong as the spontaneous emission so that the oscillation vanishes at a decay rate $3\Gamma/4$. Furthermore, when Γ approaches 4Ω , the oscillations also vanish since Ω_Γ tends to zero.

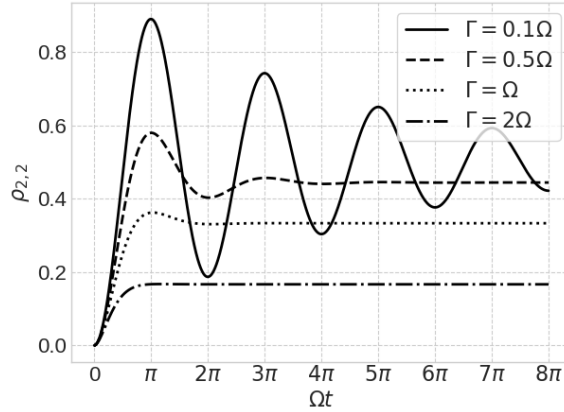


Figure 6 – Population of the excited state for damped Rabi oscillations with relaxation rates equal to 0 (exact resonance), $\Omega/2$, Ω , and 2Ω .

Source: By the author.

There is not a simple analytical solution for the general case (2.71) since the roots of the characteristic polynomial (2.69) do not have a friendly form out of specific regimes such as strong excitation and exact resonance. Then, to evaluate the coefficients a and b , and the oscillation frequency c , we numerically calculate the eigenvalues of \mathcal{M} . These eigenvalues are associated with the coefficients a , b , and c through (2.70).

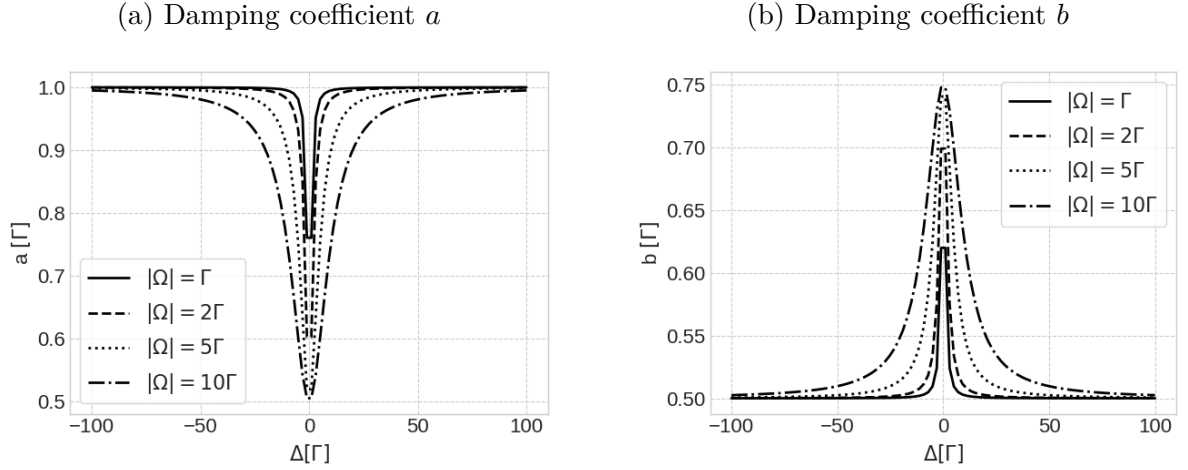


Figure 7 – Damping coefficients a and b from equation (2.71) as a function of the detuning Δ for different Rabi frequencies Ω .

Source: By the author.

The damping coefficient a from equation (2.71) is the rate at which the populations and coherences decay. From figure 7a, we can see that a converges to Γ when $a \rightarrow \pm\infty$. Also, the coefficient a is between $\Gamma/2$ and Γ . The damping coefficient b from equation (2.71) is a rate at which the Rabi oscillations decay. From figure 7b, we can see that b converges to $\Gamma/2$ when $b \rightarrow \pm\infty$ and it is between $\Gamma/2$ and $3\Gamma/4$. The lower the Rabi frequency the faster a and b converge. The system practically reaches the steady-state for a time greater than $2/\Gamma$, since both damping coefficients have the minimum $\Gamma/2$.

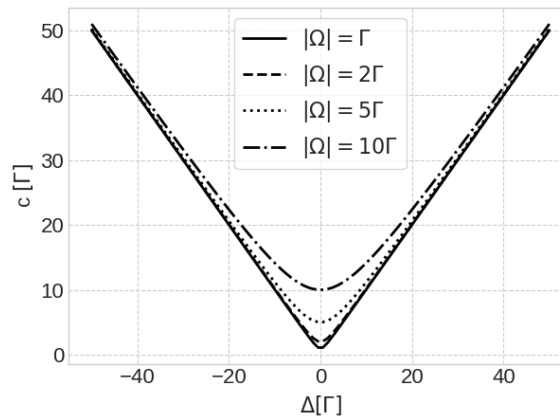


Figure 8 – Oscillation frequency c from equation (2.71) in function of the detuning Δ for different Rabi frequencies Ω .

Source: By the author.

The coefficient c from equation (2.71) is the frequency at which the system oscillates (Rabi oscillations). From figure 8, we can see that c increases linearly for higher detunings so that $c = |\Delta|$. For lower detunings, c converges to $\Omega_\Gamma = \sqrt{\Omega^2 - (\Gamma/4)^2}$.

2.2.5 Rate-equation limit

The OBEs become the Einstein rate equations when the coherent effects do not play a role. Then, we can derive the Einstein equations eliminating the coherence q in the OBEs adiabatically. Let us assume a slow population dynamics so that the coherence decay much faster than the populations. Thus, $\partial_t q \simeq 0$ in the time scale of the population dynamics. This is called **adiabatic approximation** and it is valid when there is a considerable collision rate¹⁵ γ so that $\gamma \gg \Gamma, \Omega$. In this regime, from equations (2.60), (2.61), (2.62) and (2.63), we obtain

$$\partial_t \rho_{2,2} = (1 - 2\rho_{2,2}) \frac{\Omega}{2} \frac{2\Omega/\Gamma}{1 + (2\Delta/\Gamma)^2} - \Gamma \rho_{2,2}, \quad (2.98)$$

where we assume $\partial_t \rho_{1,2} = \partial_t \rho_{2,1} = 0$ and $\rho_{1,1} = 1 - \rho_{2,2}$. Comparing equations (2.98) and (2.20), we associate

$$A \rightarrow \Gamma \quad \text{and} \quad \alpha(\Delta) = \Omega \frac{2\Omega/\Gamma}{1 + (2\Delta/\Gamma)^2}, \quad (2.99)$$

where α is the *pumping rate*. Therefore, the *saturation parameter* $s(\Delta) = \alpha(\Delta)/A$ is given by

$$s(\Delta) = \frac{2\Omega^2/\Gamma^2}{1 + (2\Delta/\Gamma)^2} = \frac{s_0}{1 + (2\Delta/\Gamma)^2}, \quad s_0 \equiv s(0) = \frac{2\Omega^2}{\Gamma^2}, \quad (2.100)$$

where s_0 is the **resonant saturation parameter**. Thus, comparing equations (2.22) and (2.100), we obtain

$$s_0 = \frac{I_0}{I_s} = \frac{2\Omega^2}{\Gamma^2} \quad \text{and} \quad g(\Delta) = \frac{g(0)}{1 + (2\Delta/\Gamma)^2}, \quad (2.101)$$

where $g(\Delta)$ is the *line shape function* and I_s is the *saturation parameter*. Since g must be normalized, we have

$$\int_{-\infty}^{\infty} g(\Delta) d\Delta = 1 \Rightarrow g(0) = \frac{2}{\pi\Gamma} \Rightarrow g(\Delta) = \frac{1}{\pi} \frac{\Gamma/2}{\Delta^2 + (\Gamma/2)^2} = \frac{2}{\pi\Gamma} \frac{1}{1 + (2\Delta/\Gamma)^2}, \quad (2.102)$$

where $g(\Delta)$ is a *Lorentzian function* whose centre is at $\Delta = 0$ and FWHM is Γ . From equations (2.32), (2.33), and (2.100), we obtain

$$\sigma(\Delta) = \frac{\hbar\omega_0}{I_s} \frac{\Gamma}{2} \frac{1}{1 + (2\Delta/\Gamma)^2} = \frac{\sigma_0}{1 + (2\Delta/\Gamma)^2} \quad \text{and} \quad (2.103)$$

$$\sigma_{abs}(\Delta) = \frac{\hbar\omega_0}{I_0} \frac{\Gamma}{2} \frac{s_0}{1 + s_0 + (2\Delta/\Gamma)^2} = \frac{\sigma_0}{1 + s_0 + (2\Delta/\Gamma)^2}. \quad (2.104)$$

Even if $\partial_t q$ is not negligible, i.e. the coherence and populations dynamics are in the same time scale, it is possible to compare the stationary solution of the OBEs and the Einstein equations in thermal equilibrium. In this case, we should obtain the same equations deduced above if we compare (2.21) and (2.78).

¹⁵ The collision rate is associated with pure dephasing terms in the Lindblad superoperator (A.30)

It is convenient to rewrite equations (2.76) and (2.77) in terms of the saturation parameter so that

$$p(\infty) = \frac{1}{1 + s(\Delta)} = \frac{1 + (2\Delta/\Gamma)^2}{1 + s_0 + (2\Delta/\Gamma)^2}, \quad (2.105)$$

$$q(\infty) = \rho_{2,1} = \frac{\Gamma}{2\Omega} \frac{s(\Delta)}{1 + s(\Delta)} (2\Delta/\Gamma - i) = \frac{\Gamma}{2\Omega} \frac{s_0}{1 + s_0 + (2\Delta/\Gamma)^2} (2\Delta/\Gamma - i). \quad (2.106)$$

2.2.6 Line-broadening mechanisms

In section 2.1.3, we introduce the *line shape function* $g(\omega)$, which gives the probability of either absorbing or emitting a photon with a frequency between ω and $\omega + d\omega$. This function is proportional to the *absorption cross-section* $\sigma(\omega)$ according equation (2.32). Although the line shape function take spectral broadening into account, it is not directly proportional to both absorbing and fluorescence profiles, which are actually measured. These profiles are associated directly with the *net absorption cross-section* σ_{abs} and the *scattering cross-section* σ_{sc} . From equations (2.104) and (B.1), we can see that the absorption profile is not a sharp line as discussed in section 2.1.3. In the next sections, we shall discuss physical effects which can both broaden and shift the absorption/scattering cross-section profile. Overall, there are two types of line broadening mechanisms:

- **Homogeneous broadening:** all atoms in a medium are affected in the same way. In this case, we can add these line-broadening mechanisms in the optical Bloch equations so that it is valid for all atoms in the medium;
- **Inhomogeneous broadening:** each atom in a medium is individually affected. In this case, we can only described line-broadening mechanisms in the optical Bloch equations for individual atoms. Therefore, we can not generalize for all atoms in the medium.

Let us assume an isolated atom initially in the excited state so that there is not an incident light beam ($s_0 = 0$). This atom will decay in an average time $1/\Gamma$ known as *lifetime*. In other words, $1/\Gamma$ is the average time for the system changes considerably. Therefore, due to the *time-energy uncertainty principle*, there will be an energy uncertainty in the excited state given by

$$\Delta E \geq \frac{\hbar}{2\Delta t} = \frac{\hbar\Gamma}{2}. \quad (2.107)$$

Spontaneously emitted photons do not have a deterministic energy $\hbar\omega_0$ since the system does not have either, as illustrated in figure 9. This phenomena provokes a *homogeneous* line-broadening known as **natural broadening** or **lifetime broadening**. The probability of spontaneously emitting a photon with frequency between ω and $\omega + d\omega$ is given by

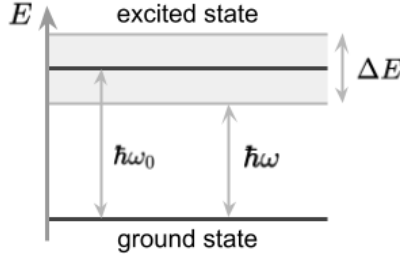


Figure 9 – Energy uncertainty of a excited state whose lifetime is $1/\Gamma$. Due to the time-energy uncertainty principle, $\Delta E \geq \hbar\Gamma/2$ and then a spontaneously emitted photon have a random energy $\hbar\omega$ whose the average is $\hbar\omega_0$ and the uncertainty is greater than $\hbar\Gamma/2$.

Source: By the author.

the line shape function $g(\omega)$ and it is proportional to the absorption cross-section $\sigma(\omega)$ according equations (2.102) and (2.103). From equation (2.102), we have

$$g(\Delta) = \frac{1}{\pi} \frac{\Gamma/2}{\Delta^2 + (\Gamma/2)^2}. \quad (2.108)$$

The equation (2.108) is *Lorentzian profile* whose FWHM, also known as *linewidth*, is Γ , which is in agreement to equation (2.16) proposed in section 2.1.3. Since Γ is associated with the natural broadening, it is also called **natural linewidth**. In the regime of weak excitation so that $s_0 \ll 1$, the absorption cross-section approximately equals the net absorption cross-section such that $\sigma \simeq \sigma_{abs}$.

In the presence of a light field so that $s_0 > 0$, the only spectral broadening is the natural broadening given by (2.108). However, the net absorption cross-section σ_{abs} does not equal the absorption cross-section σ . According to equation (2.33), there will be a decreasing by a factor of $1 + s(\omega)$, which causes a line-broadening illustrated in figure (10). From equations (2.104) and (2.103), we have

$$\sigma(\Delta) = \frac{\pi\Gamma\sigma_0}{2} g(\Delta) \quad \text{and} \quad \sigma_{abs}(\Delta) = \frac{\pi\Gamma\sigma_0}{2(1+s_0)} L(\Delta), \quad (2.109)$$

$$\text{where } L(\Delta) \equiv \frac{2}{\pi\Gamma'} \frac{1}{1 + (2\Delta/\Gamma')^2} \quad \text{and} \quad \Gamma' \equiv \Gamma\sqrt{1+s_0}. \quad (2.110)$$

The function L is known as **absorption line-shape** and it is a *Lorentzian profile* whose *FWHM* is Γ' . The quantity Γ' is known as **power-broadened linewidth**. In the regime of weak excitation so that $s_0 \ll 1$, the absorption line-shape becomes the line shape function, $L(\Delta) \rightarrow g(\Delta)$, and the power-broadened linewidth becomes the natural linewidth, $\Gamma' \rightarrow \Gamma$.

The angular frequency ω' of an incident light beam depends on the frame in which it is being observed. This effect is known as **Doppler effect**. We have been studying the atom-light interaction assuming that the light frequency is the same in both laboratory

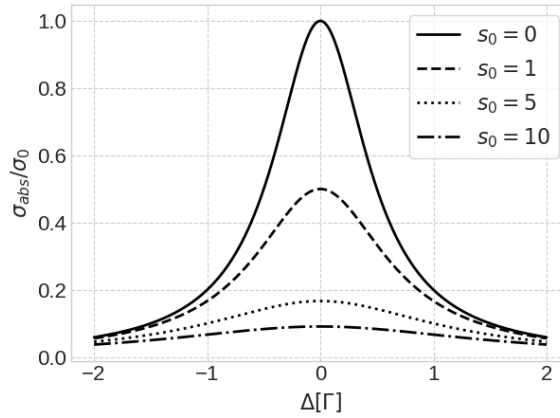


Figure 10 – Net absorption cross section as function of the detuning for some values of resonant saturation parameter.

Source: By the author.

and atom frames. However, the Doppler effect causes an *inhomogeneous resonance shift* since each atom will perceive an angular frequency given by

$$\omega' = \omega - \mathbf{k} \cdot \mathbf{v}, \quad (2.111)$$

where ω and \mathbf{k} are, respectively, the angular frequency and the wave vector of the light beam in the laboratory frame, and \mathbf{v} is the velocity of the atom also in the laboratory frame. Subtracting the resonant angular frequency ω_0 in both sides of equation (2.111), we obtain

$$\Delta_{eff} = \Delta - \mathbf{k} \cdot \mathbf{v}, \quad (2.112)$$

where $\Delta_{eff} = \omega' - \omega_0$ is the *effective detuning*. We must call $-\mathbf{k} \cdot \mathbf{v}$ as **Doppler shift**. Let us consider a gas following the *Maxwell-Boltzmann distribution* so that the probability $P(v)dv$ of finding an atom with a velocity component between v and $v + dv$ parallel to \mathbf{k} direction is given by

$$P(v)dv = \frac{1}{\alpha\sqrt{2\pi}} \exp\left(-\frac{v^2}{2\alpha^2}\right) dv, \quad \alpha \equiv \sqrt{\frac{k_B T}{m}}, \quad (2.113)$$

where T is the temperature of the gas, k_B is the Boltzmann constant, and m is the atom mass. The equation (2.113) is a **Gaussian distribution** centered at zero whose *standard deviation* is α . Also, the FWHM is approximately 2.355α . If we consider a resonant laser so that $\Delta = 0$ or $\omega = \omega_0$, we can associated an effective absorption line shape given by

$$D(\omega') = \frac{1}{\beta\sqrt{2\pi}} \exp\left[-\frac{(\omega' - \omega_0)^2}{2\beta^2}\right], \quad \beta \equiv \frac{\omega_0}{c}\alpha = \frac{\omega_0}{c}\sqrt{\frac{k_B T}{m}}. \quad (2.114)$$

2.2.7 Optical forces

We can divide the atom state into two sets. The first one is the *internal states* related to the *electronic states*. The second one is the *external states* associated with the

centre-of-mass coordinates. So far we evaluated the dynamics of the internal states, neglecting the dynamics of the atomic centre-of-mass except to explain Doppler broadening in section (2.2.6). However, there is a coupling between the external and internal degrees of freedom mediated by the absorption and emission processes, which provokes mechanical effects in the atomic centre-of-mass. These effects can be quantified from the *Ehrenfest theorem*, which establishes the average force given by

$$\mathbf{F} = -\langle \nabla \hat{V} \rangle, \quad (2.115)$$

where \hat{V} is the interaction Hamiltonian.

In section 2.2.2, we introduce the interaction Hamiltonian assuming an interaction between a two-level atom and a monochromatic light beam in the *rotating frame* and in the *interaction picture*. In the dynamics of the internal states, we can neglect the spatial dependence of the Rabi frequency Ω due to the rotating wave approximation. However, in the dynamics of the external states this spatial variation must be considered. It is important to notice that E_0 can have a spatial dependence by itself when the light beam is not a plane wave, which is the case of a Gaussian beam¹⁶. Considering $\Omega(\mathbf{r}) = |\Omega(\mathbf{r})|e^{i\mathbf{k}\cdot\mathbf{r}}$ ¹⁷, we obtain

$$\hat{V}(\mathbf{r}) = \frac{\hbar}{2} \begin{bmatrix} 0 & |\Omega(\mathbf{r})|e^{-i\mathbf{k}\cdot\mathbf{r}} \\ |\Omega(\mathbf{r})|e^{i\mathbf{k}\cdot\mathbf{r}} & -2\Delta \end{bmatrix} \Rightarrow \quad (2.116)$$

$$\nabla \hat{V} = \frac{\hbar}{2} \begin{bmatrix} 0 & (\nabla|\Omega| - i\mathbf{k}|\Omega|)e^{-i\mathbf{k}\cdot\mathbf{r}} \\ (\nabla|\Omega| + i\mathbf{k}|\Omega|)e^{i\mathbf{k}\cdot\mathbf{r}} & 0 \end{bmatrix}, \quad (2.117)$$

We can evaluate the average force (2.115) considering the property (A.15) so that

$$\mathbf{F} = -\text{Tr}[\hat{\rho}\nabla\hat{V}], \quad (2.118)$$

where $\hat{\rho}$ is the density operator of the two-level atom. As discussed in section 2.2.3, the system will reach a steady-state due to spontaneous emission, a relaxation process. We also verify that the system reaches the steady-state exponentially at a minimum rate $\Gamma/2$, where Γ is the natural linewidth. If the dynamics time scale is much greater than $2/\Gamma$, we can assume the system in the steady-state. Then, the density operator $\hat{\rho}$ are defined by equations (2.76) and (2.77) and the average force \mathbf{F} is given by

$$\mathbf{F} = -\hbar \text{Re}[(\nabla|\Omega| + i\mathbf{k}|\Omega|)q^*(\infty)]. \quad (2.119)$$

Plugging $q(\infty)$ of equation (2.106) in (2.119), we obtain

$$\mathbf{F} = -\frac{\hbar\Delta}{\Omega} \frac{s(\Delta)}{1+s(\Delta)} \nabla\Omega + \hbar\mathbf{k} \frac{\Gamma}{2} \frac{s(\Delta)}{1+s(\Delta)}. \quad (2.120)$$

¹⁶ The Gaussian beam properly described that light beam produces by a laser.

¹⁷ Any additional phase in Ω can be incorporated in the coherence q

We can simplify the equation (2.120) considering

$$\nabla \ln [1 + s(\Delta)] = \frac{2}{\Omega} \frac{s(\Delta)}{1 + s(\Delta)} \nabla \Omega. \quad (2.121)$$

Then, plugging (2.121) in (2.120), we obtain $\mathbf{F} = \mathbf{F}_{rp} + \mathbf{F}_{dp}$ where

$$\mathbf{F}_{rp} = \hbar \mathbf{k} \frac{\Gamma}{2} \frac{s(\Delta)}{1 + s(\Delta)} = \hbar \mathbf{k} \frac{\Gamma}{2} \frac{s_0}{1 + s_0 + (2\Delta/\Gamma)^2}, \quad (2.122)$$

$$\mathbf{F}_{dp} = -\nabla U_{dp}, \quad U_{dp} = \frac{\hbar \Delta}{2} \ln [1 + s(\Delta)] = \frac{\hbar \Delta}{2} \ln \left[1 + \frac{s_0}{1 + (2\Delta/\Gamma)^2} \right], \quad (2.123)$$

The dissipative force \mathbf{F}_{rp} is called **radiation pressure force** and the conservative force \mathbf{F}_{dp} is called **gradient dipole force**.

We can rewrite \mathbf{F}_{rp} from equation (2.122) considering the scattering cross-section σ_{sc} from equation (B.1) so that

$$\mathbf{F}_{rp} = \hbar \mathbf{k} \frac{I_0}{\hbar \omega_0} \sigma_{sc}(\Delta) = \hbar \mathbf{k} R_{sc}, \quad R_{sc} = \frac{\Gamma}{2} \frac{s_0}{1 + s_0 + (2\Delta/\Gamma)^2}, \quad (2.124)$$

where $I_0/(\hbar \omega_0)$ is the flux of photons from the incident beam. The quantity R_{sc} , known as **scattering rate**, is the frequency at which an atom absorbs photons from the incident beam and afterwards scatters them out by spontaneous emission. Hence, from equation (2.124), we can interpret the radiation pressure force as the gained momentum after successive events of absorption followed by spontaneous emission. Since the spontaneous emission is isotropic, only the absorption events contribute for the gained momentum as shown in figure (11).

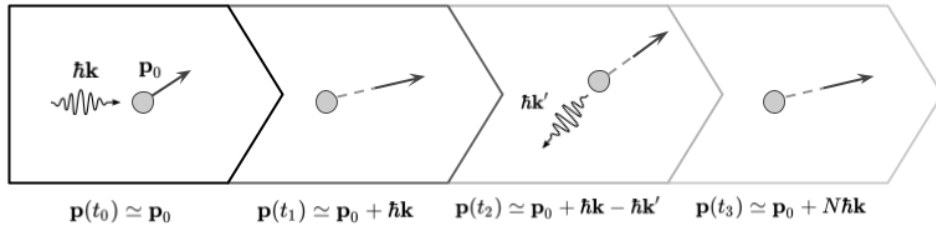


Figure 11 – Representative illustration of the radiation pressure force as an average of scattering events. An atom initially with momentum \mathbf{p}_0 absorbs a photon with momentum $\hbar \mathbf{k}$ after a period $t_1 - t_0$. Then, at instant t_2 , this atom spontaneously emits a photon with momentum $\hbar \mathbf{k}'$ so that $|\mathbf{k}| = |\mathbf{k}'|$. Finally, after successive absorption and emissions, the final momentum will be $\mathbf{p} \simeq \mathbf{p}_0 + N \hbar \mathbf{k}$ since the spontaneous emission is isotropic. The quantity N is the number of absorbed photons after a period $t_3 - t_0$. Therefore, the impulse after a period Δt will be $\Delta \mathbf{p} = \hbar \mathbf{k} R_{sc} \Delta t$, where R_{sc} is the rate at which the atom scatters photons.

Source: By the author.

From equation (2.124), we can see that the radiation pressure force has the maximum at resonance, and it decreases with the detuning. Also, this force saturates when s_0 is much greater than $1 + (2\Delta/\Gamma)^2$. The spontaneous emission rate determines the force intensity, which is as greater as Γ . Since \mathbf{F}_{rp} is a dissipative force, it can be used to both cool and trap atoms, being a the key concepts to understand MOTs.

The gradient dipole force can be derived from a potential U_{dp} illustrated in figure (12), and therefore it is a conservative force. At resonance, U_{dp} is zero and its module increases with the detuning for a range near to resonance. Far from resonance, U_{dp} asymptotically goes into zero. Unlike the radiation pressure force, the gradient dipole force does not saturate. It can increase continuously without bound, though it only does logarithmically for large intensities (saturation parameter). This forces is usually applied to spatially confine atoms.

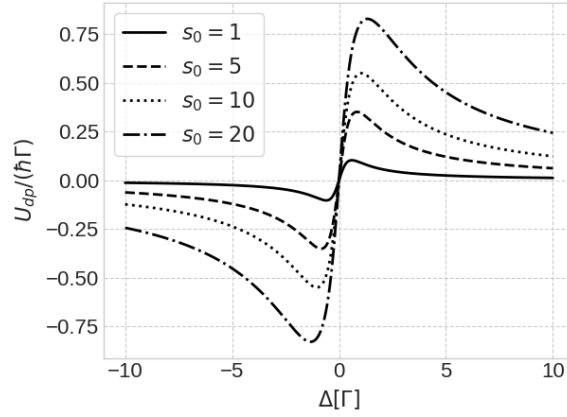


Figure 12 – Potential from gradient dipole force for few saturation parameters as a function of the laser detuning.

Source: By the author.

3 MAGNETO-OPTICAL TRAP

The magneto-optical trap (MOT) is a technique widely used in laser cooling experiments which allows both trapping and cooling of an atomic dilute gas. In this section, we shall approach the MOT theory (13, 32) considering the simplest transition $J = 0 \rightarrow J = 1$, where J is the total angular momentum of the electronic state. To get an insight into the cooling and trapping mechanisms, we introduce a simplified one-dimensional MOT (1D-MOT) assuming two counter-propagating laser beams and a linear magnetic field¹. The three-dimensional case is more complicated to approach since there are considerable difficulties related to the complex spatial structure of the light field (33), which hampers a quantitative analysis. Lastly, we introduce **narrow-line magneto-optical traps** (nMOTs) (34) by assuming an atomic transition with a natural linewidth (section 2.2.6) close to the photonic recoil.

3.1 One-dimensional model

Let us consider a simplified one-dimensional model (1D-MOT) illustrated in figure 13. In this model, two counter-propagating laser beams of opposite circular polarization interact with an atom in the presence of a linear magnetic field $\mathbf{B} = B_0 z \mathbf{e}_z$, where $B_0 > 0$ is the gradient magnitude. Both laser beams have the same angular frequency ω and are tuned close to the transition $J = 0 \rightarrow J = 1$ whose angular frequency is ω_0 .

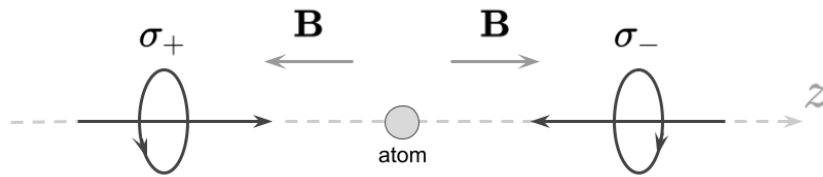


Figure 13 – Simplified one-dimensional MOT composed of two counter-propagating laser beams and a linear magnetic field $\mathbf{B} = B_0 z \mathbf{e}_z$, where $B_0 > 0$. We consider the σ_+ and σ_- beams right-handed and left-handed polarized respectively.

Source: By the author.

Disregarding the magnetic field, the transition is properly represented by a degenerate *two-level system* whose energy difference is $\hbar\omega_0$. The presence of the magnetic field splits the energy level $J = 1$ into three different energy levels $m_J = 0, \pm 1$ such that the system turns into a *four-level system* illustrated in figure 14. This effect is known as

¹ A linear magnetic field is not a real magnetic field since it does not satisfy the Gauss's law for magnetism.

Zeeman splitting (26, Section 7.4). Essentially, assuming a weak magnetic field², there will be a effective detuning $\delta_Z^{(m_J)}$ due to the **anomalous Zeeman effect** so that

$$\delta_Z^{(m_J)} = -\beta g_J m_J z, \quad \text{being } \beta \equiv \frac{\mu_B B_0}{\hbar}, \quad (3.1)$$

where g_J is the *Landé factor* and μ_B is the Bohr magneton. The equation (3.1) is also called **Zeeman shift**. It is relevant to notice that the detuning depends linearly on the position z so that $\delta_Z^{(m_J)} \propto z$.

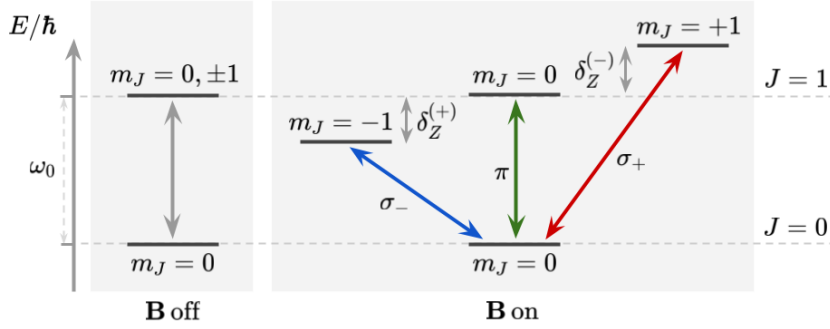


Figure 14 – Zeeman splitting of the transition $J = 0 \rightarrow J = 1$ in 1D-MOTs. When $\mathbf{B} = 0$ (**B off**), the atomic transition $J = 0 \rightarrow J = 1$ is described by a **degenerate two-level system**. However, when $\mathbf{B} \neq 0$ (**B on**), the same atomic transition is represented by a **four-level system** in which the excited states are energetically separated by the Zeeman shift $\delta_Z^{(\pm)}$. The energy scale was not plotted precisely to enhance the visibility.

Source: By the author.

3.1.1 Cooling and trapping effect

Let us consider an arbitrary atom from an atomic cloud in a MOT neglecting interatomic interactions. Although the momentum exchange between atoms and light are quantized, we can evaluate the atom dynamics classically by assuming a mean force \mathbf{F}_{MOT} , which is known as **semiclassical approach**. It is possible to obtain an analytical expression for \mathbf{F}_{MOT} under the **two-level system approximation**, which will be done in the next section 3.1.2. Without this approximation, we must consider the interplay between optical pumping, photon scattering, Zeeman effect, and Doppler effect in multiple excited states. Therefore, the complexity of the problem will increase considerably. There are only a few articles (33,35,36) that approach this case.

² The quantity $\mu_B B$, where B is the magnetic field magnitude, must be much lower than the spin-orbit coupling energy.

We can split \mathbf{F}_{MOT} into two components³: one exclusively associated with coherent transitions (absorption and *stimulated* emission); and another associated with decoherence decays (absorption and *spontaneous* emission). In weak atom-light coupling, stimulated emission is much less often than spontaneous emission. Therefore, \mathbf{F}_{MOT} is the **radiation pressure force**. Essentially, $\mathbf{F}_{MOT} = (F_+ - F_-)\mathbf{e}_z$, where F_{\pm} is related to the interaction between atom and the σ_{\pm} -beam. Thus, F_{\pm} depends on the detuning Δ_{\pm} so that the lower $|\Delta_{\pm}|$, the greater F_{\pm} . The detuning Δ_{\pm} can be split into three detunings (figure 15) so that $\Delta_{\pm} = \delta + \delta_Z^{\pm} + \delta_D^{\pm}$. These detunings are given by

- *Laser detuning* $\delta = \omega - \omega_0$: associated with the laser frequency ω and the energy difference ω_0 of the atomic transition. This detuning is the same for all transitions;
- *Doppler shift* $\delta_D^{(\pm)} = \mp kv$: associated with the atomic movement (see section 2.2.6);
- *Zeeman shift* $\delta_Z^{(\pm)} \propto \mp z$: associated with the Zeeman splitting. This detuning is given by the equation (3.1).

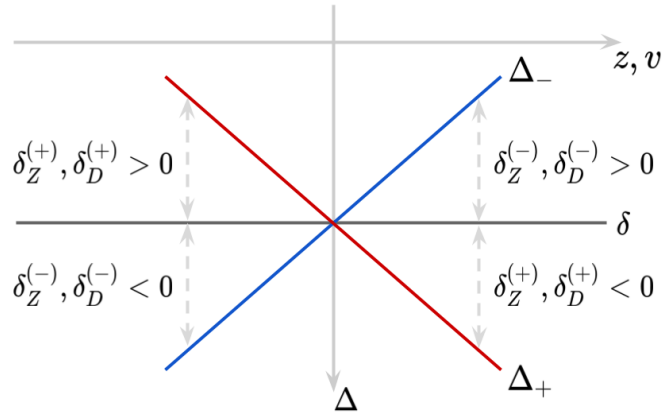


Figure 15 – Laser detuning, Doppler shift, and Zeeman shift of a 1D-MOT in function of velocity v and position z assuming red-detuned laser beams ($\delta < 0$).

Source: By the author.

Both Doppler shift and Zeeman shift increase linearly with the atom velocity and atom position respectively. Assuming red-detuned laser beams ($\delta < 0$) and $v > 0$, the probability of absorbing the σ_{\pm} -beam decreases (increases) with v since $|\Delta_{\pm}|$ increases (decreases). When $v < 0$, the opposite effect occurs. Therefore, the MOT force is opposite to the velocity v ($\partial\mathbf{F}_{MOT}/\partial v < 0$) such as a friction, which is essentially a **cooling mechanism** also known as **Doppler cooling**. The Zeeman shift behaves the same in function of z such that the MOT force is also opposite to the position ($\partial\mathbf{F}_{MOT}/\partial z < 0$), which is essentially a **trapping mechanism**.

³ In section 2.2.7, we deduced both forces for the case of a two-level atom interacting with a single field.

3.1.2 MOT Force

We shall get deeper into the 1D-MOT analysis by quantifying the MOT force. As mentioned in section 3.1.1, obtain an analytical expression for the MOT forces in the general case is a complicated task. Although, we can obtain such analytical expression under two approximations:

- By breaking the four-level system (figure 14) into three independent two-level systems illustrated in figure 16. That is a strong assumption in which the coherence effects between the Zeeman states, such as Raman-like transitions (25, Section 9.8), are neglected;
- By assuming that the atom density operator $\hat{\rho}(\mathbf{k}, -\mathbf{k})$ related to the simultaneous interaction equals the sum of the density operators $\hat{\rho}_+(\mathbf{k})$ and $\hat{\rho}_-(-\mathbf{k})$ associated with the individual interactions, which is essentially a superposition ($\hat{\rho} = \hat{\rho}_+ + \hat{\rho}_-$). This approximation relies on the perturbation theory in first and second-order (37, Chapter 7).

Both approximations are valid in the regime of weak atom-light coupling so that the total detuning is higher than the power-broadened linewidth.

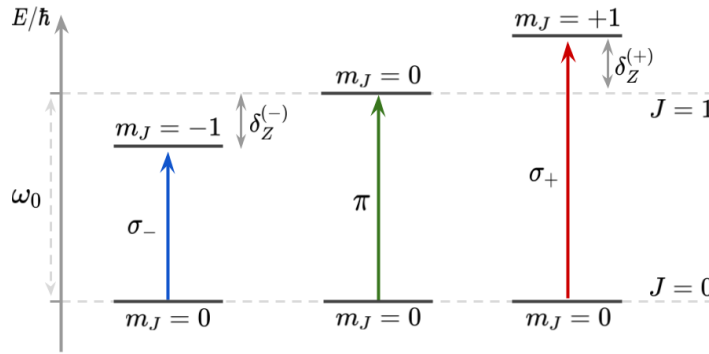


Figure 16 – Breaking of a four-level system into three independent two-level systems.

Source: By the author.

Since there are only right-handed and left-handed polarized beams, there will only σ_{\pm} -transitions. Therefore, the components F_+ and F_- associated with the σ_+ and σ_- transitions respectively are independent radiation pressure forces given by (see section 2.2.7)

$$F_{\pm}(z, v) = \pm \hbar k \frac{\Gamma}{2} \frac{s_0}{1 + s_0 + 4(\Delta_{\pm}/\Gamma)^2}, \quad (3.2)$$

where $\Delta_{\pm} = \delta + \delta_Z^{(\pm)} + \delta_D^{(\pm)}$, s_0 is the saturation parameter, and Γ is the natural linewidth⁴ of the transition $J = 0 \rightarrow J = 1$. Assuming low velocities ($|kv| \ll |\delta|$) and positions close to the magnetic field centre ($|z| \ll |\delta|$), the MOT force is essentially linear with z and v as illustrated in figure 17. Hence, we can expand F_{MOT} about $z = 0$ and $v = 0$ so that

$$F_{MOT}(z, v) \simeq F_{MOT}(0, 0) + z \frac{\partial F_{MOT}}{\partial z}(0, 0) + v \frac{\partial F_{MOT}}{\partial v}(0, 0), \quad (3.3)$$

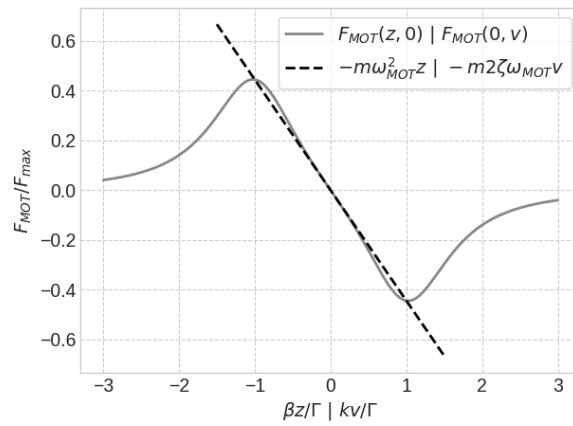


Figure 17 – MOT force F_{MOT} for $v = 0$ ($z = 0$) as a function of $\beta z/\Gamma$ (kv/Γ) considering the transition $^1S_0 \rightarrow ^1P_1$ of the ^{88}Sr for $\delta = -\Gamma$ and $s_0 = 1$. The dashed line in the graph is the MOT force assuming $|\beta z| \ll |\delta|$ ($|kv| \ll |\delta|$).

Source: By the author.

Rearranging the terms of equation (3.3), we obtain

$$\frac{d^2 z}{dt^2} + 2\zeta\omega_{MOT} \frac{dz}{dt} + \omega_{MOT}^2 z = 0, \quad (3.4)$$

$$\omega_{MOT}^2 \equiv -\frac{1}{m} \frac{8\hbar k \beta g_J s_0 (\delta/\Gamma)}{[1 + s_0 + 4(\delta/\Gamma)^2]^2}, \quad \text{and} \quad \zeta \equiv \frac{k}{2\beta g_J} \omega_{MOT}, \quad (3.5)$$

where m is the atomic mass. The quantity ω_{MOT} has unit of frequency and ζ is a dimensionless quantity. Also, ω_{MOT}^2 is a positive real value since we are assuming red-detuned lasers, which means $\delta < 0$ in equation 3.5. The equation of motion (3.4) describes a *damped harmonic oscillation* of which ω_{MOT} is the *undamped frequency* and ζ is the *damping ratio*. Therefore, the atom is trapped by the restoring force $-m\omega_{MOT}^2 z$, being limited to move in a restricted region (**trapping mechanism**). Furthermore, the atom loses energy due to the damping $2\zeta\omega_{MOT}v$ can be understood as a **cooling mechanism**.

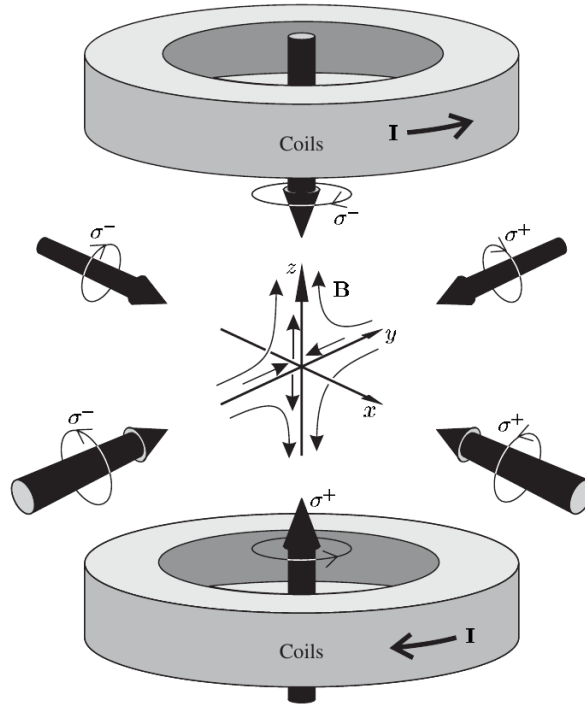


Figure 18 – Standard arrangement of MOT composed of three orthogonal pairs of counter propagating laser beams with opposite circular polarization and coils in anti-Helmholtz configuration, which produces a magnetic quadrupole field.

Source: FOOT et al. (25).

3.2 Three-dimensional case

Let us assume the standard 3D-MOT arrangement illustrated in figure 18. An atom, free to move along all Cartesian axes, interacts with *three pairs* of counter-propagating laser beams with opposite circular polarization and a magnetic quadrupole field \mathbf{B} . In a first attempt, we can naturally extend the 1D-MOT theory into a 3D theory considering that each laser beam yields a radiation pressure force given by equation (3.2). Nevertheless, the quantization axis (z -axis) must match the direction of the field \mathbf{B} to properly evaluate the Zeeman shift, which implies that each laser beam polarization depends on the atomic position. This is not a concern in the 1D-MOT since the magnetic field has a fixed direction. Therefore, a theoretical description of the 3D-MOT (33) encounters considerable difficulty due to the spatial-dependence of the quantization axis. Regardless of the theoretical complications, the cooling and trapping effects of MOTs are widely confirmed for many alkali (38–40) and lanthanide (14–16). Also, in this thesis, we could demonstrate both effects for dysprosium and strontium atoms through a Monte Carlo simulation.

⁴ The natural linewidth depends on the energy difference between the states, which is slightly different in each transition. However, this energy difference is much lower than $\hbar\omega_0$ such that the natural linewidth is approximately Γ .

3.2.1 Limit temperature in Doppler cooling

Let us consider a equilibrium atomic position close to the magnetic field centre. In this case, the Zeeman shift becomes negligible compared to the Doppler shift ($\delta_Z \ll \delta_D$) such that a defined quantization axis is no longer required.⁵ Also, we suppose weak atom-light couplings in which the laser detuning are grater than the power-broadened linewidth. Thus, the interaction between each laser beam and the atom is independent and it is described by two-level dynamics. In this situation, the MOT force is given by

$$\mathbf{F}_{MOT}(\mathbf{v}) = \frac{\hbar k \Gamma s_0}{2} \sum_{n=1}^3 \left(\frac{1}{1 + s_0 + 4[\delta - k(\mathbf{v} \cdot \mathbf{e}_n)]^2/\Gamma^2} - \frac{1}{1 + s_0 + 4[\delta + k(\mathbf{v} \cdot \mathbf{e}_n)]^2/\Gamma^2} \right) \mathbf{e}_n, \quad (3.6)$$

where $\{\mathbf{e}_1, \mathbf{e}_2, \mathbf{e}_3\}$ is the Cartesian basis. We are assuming all laser beams with the same saturation parameter s_0 , wavevector magnitude k , and detuning δ . For low velocities v such that $kv \ll \delta$, we can expand the MOT force around $\mathbf{v} = 0$ so that $\mathbf{F}_{MOT} \simeq -\gamma \mathbf{v}$,

$$\gamma = -\frac{8\hbar k^2 s_0 (\delta/\Gamma)}{[1 + s_0 + 4(\delta/\Gamma)^2]^2}. \quad (3.7)$$

Assuming red-detuned laser beams ($\delta < 0$), we have $\gamma > 0$ and then \mathbf{F}_{MOT} describes a friction force. Hence, the velocity vanishes after a time as long as $1/\gamma$ and then the final temperature should be zero. However, the \mathbf{F}_{MOT} is an average. We also must to consider the variance effect of \mathbf{F}_{MOT} which relies on the Brownian atomic motion due to spontaneous emission. This random dynamics yields a *heating process*. Therefore, the balance between cooling and heating mechanisms set finite temperature.

From the *equipartition theorem*, the average total energy of the atom is given by

$$\frac{\Delta \mathbf{p}^2}{2m} = \frac{3}{2} k_B T, \quad (3.8)$$

where T is the temperature of the atomic cloud, m is the the atomic mass, and \mathbf{p} is the linear momentum of the atom. There is an association between the **diffusion coefficient**⁶ D and the quantity $\Delta \mathbf{p}^2$ given by $\Delta \mathbf{p}^2 \approx D/\gamma$ (32, Section 2). To obtain an expression for D , we need to calculate quantum fluctuations, which is out of the scope of this work. However, skipping this step (32, Section 2.3), there are two possible regimes in which we can define a temperature (34, Section V):

- $\delta/\Gamma \gg 1$:

$$T(s_0) = \sqrt{1 + s_0} T_0 \quad (3.9)$$

⁵ Essentially, we are proposing the treatment of a MOT as an **optical molasses**, which is a similar technique to only cool an atomic dilute gas based upon *Doppler cooling*.

⁶ Correlation between the $\mathbf{F}_{MOT}(t)$ and $\mathbf{F}_{MOT}(t + \delta t)$, where t is a specific instant and δt is a time interval.

- $\delta/\Gamma \sim 1$

$$T(s_0, \delta) = \frac{1 + 4(\delta/\Gamma_E)^2}{4|\delta|/\Gamma_E} \sqrt{1 + s_0} T_0 \quad (3.10)$$

where $T_0 \equiv \hbar\Gamma/(2k_B)$ is known as **Doppler cooling limit** and $\Gamma_E \equiv \Gamma\sqrt{1 + s_0}$ is the **power-broadened linewidth**. The temperature is dependent of the lasers intensity in both regimes and is dependent of the lasers detuning only in the low saturation case.

3.2.2 Atomic cloud size

The atomic cloud size is typically characterized by its root-mean-square width along each spatial dimension. There are several factors which influence the cloud size such as the laser arrangement, the magnetic field, the atomic species features, gravity, and interatomic interactions. Overall, the cloud size is defined by the trapping potential. Thus, considering the equipartition theorem, we have

$$\frac{1}{2}\kappa_i \langle x_i^2 \rangle = \frac{1}{2}k_B T \Rightarrow \sigma_i \equiv \sqrt{\langle x_i^2 \rangle} = \frac{k_B T}{\kappa_i}, \quad (3.11)$$

where σ_i is the cloud size on the x_i direction, κ_i is the *spring constant* on the same direction, and T is the temperature of the cloud. In the unidimensional MOT, from equation (3.4), $\kappa_i = m\omega_{MOT}^2 \propto B_0/(s_0\delta)$. Therefore, the more intense the magnetic field gradient, the smaller the cloud size. The saturation parameter and the detuning cause an inverse effect. The atomic cloud will have a Gaussian shape when the laser arrangement is symmetric and the centre of mass is at the magnetic field origin. In the regime of low density, the cloud size given by equation (3.11) is a proper estimation. However, interatomic interactions play a role when the density increases. These interactions expand the cloud by a factor of $N^{1/3}$ as shown in figure 19, where N is the number of atoms, due to the reabsorption of scattered photons (light-induced interactions) (41).

3.2.3 Magnetic force

Since the atom experiences a magnetic field gradient, it also feels a position-dependent magnetic force $\mathbf{F}_B(\mathbf{r})$ (42, Section 3.2.1) given by

$$\mathbf{F}_B(\mathbf{r}) = -g_J m_J \mu_B \nabla |B(\mathbf{r})| \quad (3.12)$$

where g_J is the *Landé* factor of the ground state and m_J is the magnetic quantum number of the ground state⁷. The magnetic field $\mathbf{B}(\mathbf{r})$ does not have a trivial dependence with the position since it is generated by anti-Helmholtz coils as illustrated in figure 18. However,

⁷ We should consider one force for each excited states. However, the average time $1/\Gamma$ that the atom stays in the excited state is much lower than the average time it remains in the ground state.

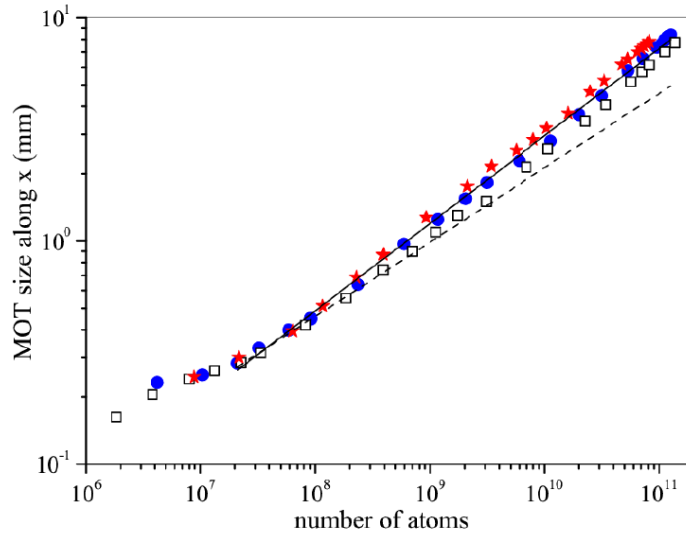


Figure 19 – Measure of the full width at half maximum size of a rubidium atomic cloud along the magnetic coils axis. The three sets of data correspond to different MOT detunings. The solid line is a free fit of the data and the dashed line is fit considering the scaling model $L \propto N^{1/3}$.

Source: CAMARA; KAISER; LABEYRIE. (41).

the atom is restricted to move close to the magnetic field centre, otherwise the MOT force will throw it away from the trap. Hence, \mathbf{B} can be approximated by the following linear expression

$$\mathbf{B} = B_0 \left(\frac{x}{2} \hat{\mathbf{x}} + \frac{y}{2} \hat{\mathbf{y}} - z \hat{\mathbf{z}} \right), \quad (3.13)$$

where B_0 depends only on the coils features. Thus, the magnetic force \mathbf{F}_B will be

$$\mathbf{F}_B(x, y, z) = -\frac{g_J m_J \mu_B B_0 / 2}{\sqrt{x^2 + y^2 + 4z^2}} (x \hat{\mathbf{x}} + y \hat{\mathbf{y}} + 4z \hat{\mathbf{z}}), \quad (3.14)$$

where x , y , and z are the Cartesian coordinates whose origin is the magnetic field. This force is comparable to gravity for very large magnetic field gradients, which is not suitable for MOTs because large gradients decrease the trapping region. Therefore, we expect that the magnetic force will be much lower than the radiation pressure forces.

3.3 Narrow-line magneto-optical trap

In previous sections, we have been neglecting the gravity effect on the MOT parameters. This assumption is valid when the MOT force is much higher than gravity. The maximum radiation pressure force on an atom is $\hbar k \Gamma / 2$ from equation (3.2). Therefore, the ratio between the maximum radiation pressure force and gravity is

$$R \equiv \frac{\hbar k \Gamma}{2mg}, \quad (3.15)$$

where m is the atomic mass and g is the gravitation acceleration. Usually, R is on the order of 10^5 . Hence, the gravity force is negligible since the radiation pressure force is much higher. However, the lower Γ , the higher the gravity effect so that for $\Gamma \sim \text{kHz}$, the ratio (3.15) approaches values on the order of 10. In this case, the centre of mass moves towards the gravity direction such that, for small laser intensities, the atoms gather on the bottom of the surface of an ellipsoid as illustrated in figure 20.

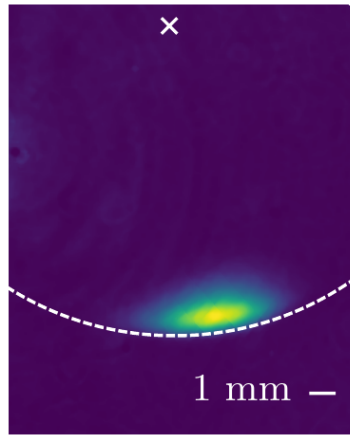


Figure 20 – Typical *in situ* absorption image of an atomic sample in a nMOT.

Source: DREON. (43)

Furthermore, Γ also defines the average number of scattering events per time (**scattering rate**) so that the lower Γ , the fewer the number of events in a determined time interval. We have been analysing the atoms dynamics classically through the optical forces, which assumes that there are a large number of momentum exchange in a small period of time. In this condition, we can average out a force. That is not satisfied when Γ is sufficient smaller. In this case, we must include the discrete momentum exchange in the analysis and then treat the dynamics quantum mechanically. To quantify the range of Γ in which this happens, let us define the ratio given by

$$\eta = \frac{\Gamma}{\omega_R} = \frac{m\lambda^2\Gamma}{2\pi^2\hbar} = \quad (3.16)$$

where $\hbar\omega_R$ is the kinetic energy $(\hbar k)^2/(2m)$ gain by the atom when it absorbs an photon with the momentum $\hbar k$, h is the Planck constant, and $\lambda = 2\pi/k$ is the wavelength.

This energy is known as **photonic recoil**. When $\eta \leq 1$, one scattering event is able to detune the atom-light interaction. A MOT whose $\eta \sim 1$ or less is known as **narrow-line magneto-optical trap** (nMOT), whereas a MOT whose $\eta \gg 1$ is known as **broad-line magneto-optical trap**. We shall call the ratio (3.16) as **narrowness**.

3.3.1 Operating regimes

Four quantities play a crucial role in nMOTs operating: the saturation parameter s_0 , the laser detuning δ , the natural linewidth Γ , and the photonic recoil ω_R . We can combined s_0 and Γ in a single quantity known as **power-broadened linewidth** $\Gamma' \equiv \Gamma\sqrt{1 + s_0}$, which is the natural energy scale of the atom-light interaction due to the power-broadening mechanism (section 2.2.6). Furthermore, we can summarize those quantities in two essential quantities that characterized nMOTs:

- ($\eta' \equiv \Gamma'/\omega_R$): it defines the relevance of single scattering events to the the atom-light interaction taking the natural energy scale into account. Hence, η' is more accurate than η ;
- ($\delta' \equiv \delta/\Gamma'$): it defines the coupling strength between atom and light normalized by the natural energy scale of the interaction.

When $\eta' \gg 1$, the semiclassical approach is suitable since the photonic recoil is much lower than the natural energy scale and, therefore, the scattering events can be averaged out. There are three nMOTs regimes:

- I **Doppler regime** ($\eta' \gg 1$ and $|\delta'| < 1$): in this regime, gravity is negligible so that the atomic cloud is ellipsoidal;
- II **Power-broadened regime** ($\eta' \gg 1$ and $|\delta'| > 1$): In this regime, gravity is comparable to the radiation pressure forces such that the atomic cloud centre of mass sags to vertical positions.
- III **Quantum regime** ($\eta' \sim 1$): in this regime, the photonic recoil is the natural energy scale and, therefore, the quantum physics governs the nMOT dynamics.

3.3.2 Centre of mass of the atomic cloud

We can estimate the centre of mass of the atomic cloud in the power-broadened regime by assuming that all radiation pressure forces on an atom balance each other in all directions except in the gravity direction \hat{z} . In this direction, the radiation pressure forces F_{\pm} balance with the gravity force as illustrated in figure 21. Thus, a trapped atom is restricted to be in a region where the magnetic field components perpendicular to z

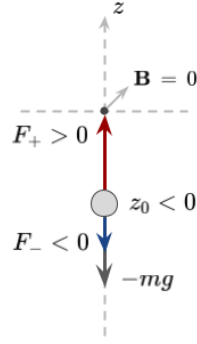


Figure 21 – Forces diagram of a trapped atom in a power-broadened nMOT.

Source: By the author.

is zero, otherwise there will be unbalance between forces in those direction due to the Zeeman shift (see section 3.1.1). The average position of a trapped atom must be $\vec{r} = z_0 \hat{z}$ so that its dynamics is well described by the one-dimensional model presented in section 3.1. From equations (3.2), we obtain the following equation of motion

$$\hbar k \frac{\Gamma}{2} s_0 \left(\frac{1}{1 + s_0 + 4(\Delta_+/\Gamma)^2} - \frac{1}{1 + s_0 + 4(\Delta_-/\Gamma)^2} \right) - mg = 0. \quad (3.17)$$

We must impose $|\Delta_+| < |\Delta_-|$ to ensure a solution to the equation (3.17). Neglecting the Doppler shift ($\delta_D^{(\pm)} = 0$), and assuming red-detuned lasers⁸ ($\delta < 0$), we obtain $z_0 < 0$, which means the centre of mass will be located below the magnetic field origin. Let us consider $|\delta| \gg 1$ so that $|\Delta_+| \gg |\Delta_-|$. In this condition, F_- is negligible. Hence, we can approximate the equation (3.17) to

$$\hbar k \frac{\Gamma}{2} s_0 \left(\frac{1}{1 + s_0 + 4[(\delta + \delta_Z^{(+)})/\Gamma]^2} \right) - mg = 0. \quad (3.18)$$

We have been assuming the transition $J = 0 \rightarrow J = 1$ such that $\delta_Z^{(+)} = -\beta g_J m_J z$. However, the transition can happen between any transition $J = j \rightarrow J = j + 1$, where $j \geq 0$. To take it into account, we must consider

$$\delta_Z^{(+)} = -\beta \chi z_0, \text{ being } \chi \equiv (g_J - g'_J)j > 0, \quad (3.19)$$

where g'_J and g_J are the *Landé factors* of the excited and ground states respectively. The equation (3.19) is valid when the transitions only happens between the states $m_J = -j$ and $m_J = -j + 1$. Isolating z_0 , we obtain

$$z_0 = -\frac{1}{\beta \chi} \left(\delta + \frac{\Gamma}{2} \sqrt{\frac{\hbar \Gamma s_0}{2 \lambda m g}} - 1 - s_0 \right) \quad (3.20)$$

The equation (3.20) is only valid when the centre of mass is sufficient below the magnetic field origin to match all the assumptions described above and in section 3.1.2.

⁸ This assumption is necessary to create a trapping environment as discussed in 3.1.1.

4 MONTE CARLO SIMULATION

In order to predict experimental quantities in nMOTs, we propose a Monte Carlo simulation that estimates the probability distributions of both the atoms' position and velocity. The goal is to acquire simulated quantities in agreement with experimental measures for different nMOTs by considering as many parameters as possible. Our simulation can be used to optimize the parameters of nMOTs without the necessity of experimental data. It is also a tool to analyse the feasibility of unusual nMOT arrangements such as nMOTs with fewer laser beams. We developed a module for Python using the C programming language¹ that implements our model with high performance. We also developed a Python program that applies the model-view-controller pattern and parallelism. In this section, we shall introduce our model as well as its deployment.

4.1 Stochastic evolution

Let us consider an atom at \mathbf{r}_0 and with the velocity \mathbf{v}_0 in the presence of laser beams and a quadrupole magnetic field. After a period δt , this atom can absorb a photon with momentum $\hbar \mathbf{k}_j$ and then emit a photon with momentum $\hbar |\mathbf{k}_j| \hat{\mathbf{u}}$, where $\hat{\mathbf{u}}$ is a uniform unit random vector and \mathbf{k}_j is the wave vector of the j -th laser beam. Also, since there is a magnetic field gradient, a magnetic force acts on the atom as discussed in section 3.2.3 that yields a position-dependent acceleration $\mathbf{a}_B(\mathbf{r}_0)$. Therefore, the atom's velocity \mathbf{v}_i and position \mathbf{r}_i at instant $i\delta t$, where $i = 0, 1, \dots$, are

$$\mathbf{v}_i = \begin{cases} \mathbf{v}_{i-1} + \hbar \frac{|\mathbf{k}_j|}{m} (\hat{\mathbf{k}}_j + \hat{\mathbf{u}}) + (\mathbf{a}_B(\mathbf{r}_{i-1}) - g\hat{\mathbf{z}})\delta t, & \text{with probability } P_{i,j} \\ \mathbf{v}_{i-1} + (\mathbf{a}_B(\mathbf{r}_{i-1}) - g\hat{\mathbf{z}})\delta t, & \text{with probability } 1 - \sum_j P_{i,j} \end{cases} \quad (4.1)$$

and

$$\mathbf{r}_i = \mathbf{r}_{i-1} + \mathbf{v}_i \delta t + (\mathbf{a}_B(\mathbf{r}_{i-1}) - g\hat{\mathbf{z}})\delta t^2/2, \quad (4.2)$$

where $P_{i,j}$ is the probability of happening a scattering event due to the j -th laser beam also known as **transition probability**. Since $P_{i,j}$ is a conditional probability that depends on the previous atom state, the dynamics is then a **memoryless stochastic process**, also known as **Markov chain**. The goal is to sample trajectories $\mathbf{r}(t)$ and velocities $\mathbf{v}(t)$ in order to estimate the probability distributions of the atom's position and velocity. To perform this, we iterate the equations (4.1) and (4.2) and then fill up histograms.

We shall assume that simulating a single atom's motion for a long period of time is equivalent to simulating the motion of many atoms over smaller periods of time, which

¹ We choose the C language since it is one of the fastest languages available.

is known as **the ergodic hypothesis**. Thus, we shall work with ensembles of atoms' motions. We also shall neglect the interaction between atoms so that the atoms' motions will be independent of each other. These assumptions allow us to efficiently apply parallelism and then decrease the computational time.

4.1.1 Equilibrium

Let us consider the vector $\rho(t) = \rho(i\delta) = \rho_i$ in which each component is the probability of an atom being at specific position $\mathbf{r} = (x, y, z)$ with a specific velocity $\mathbf{v} = (v_x, v_y, v_z)$ at a instant t . We shall call this vector as **atom state**. Although position and velocity are continuous variables, we must discrete both to perform a feasible computation. If we consider N possible values for x, y, z, v_x, v_y , and v_z , the dimension of the vector ρ_i is N^6 , which means that the computational spatial complexity is very high and can leads to memory issues. However, we can reduce such complexity by getting only the the marginal probabilities $\rho_{i,\alpha}$, where $\alpha \in \{x, y, z, v_x, v_y, v_z\}$, since they are independent, $\rho_i = \sum_{\alpha} \rho_{i,\alpha}$. Hence, the total dimension will be reduced to $6N$.

Let us represent the transition probabilities P_i in the same vector space as a matrix \mathbf{P} of which each element is $P_{i,j}$ ². Therefore, after n iterations, the atom state will be (44, Section 23.2)

$$\rho_n = \rho_0 \underbrace{(\mathbf{P} \times \mathbf{P} \times \cdots \times \mathbf{P})}_{\text{multiply the matrix } n \text{ times}} = \rho_0 \mathbf{P}^n, \quad (4.3)$$

where ρ_0 is the initial atom state given by a deterministic vector since we set the initial atom's position and velocity. We expect that ρ be constant after a sufficient number of iterations so that $\rho = \rho \mathbf{P}$ for large enough n . In this case, we say that ρ is **stationary** and then the Markov chain settle into an **equilibrium**. We can ensure this assumption based on the **thermodynamics equilibrium**. To make sure that we are only getting samples in the equilibrium, we only store \mathbf{r} and \mathbf{v} after a specified number of iterations.

4.1.2 Magnetic field frame

We shall consider the assumptions introduced in section 3.1.2, which simplifies a four-level system in three independent two-level systems associated with the polarizations σ_{\pm} and π . In this condition, for each laser beam, there are three possible transitions, each one with its scattering rate $R_{i,j,l}$, where $l \in \{\sigma_+, \sigma_-, \pi\}$. Initially, we define the laser polarizations on the basis $\mathbf{B} = \{\hat{\sigma}_+, \hat{\sigma}_-, \hat{\pi}\}$ so that

$$\hat{\sigma}_+ = \frac{\hat{\mathbf{x}} + i\hat{\mathbf{y}}}{\sqrt{2}}, \quad \hat{\sigma}_- = \frac{\hat{\mathbf{x}} - i\hat{\mathbf{y}}}{\sqrt{2}}, \quad \hat{\pi} = \hat{\mathbf{z}}, \quad (4.4)$$

where $A = \{\hat{\mathbf{x}}, \hat{\mathbf{y}}, \hat{\mathbf{z}}\}$ is the basis of the **laboratory frame**.

² We are assuming that \mathbf{r} and \mathbf{v} are discrete variables

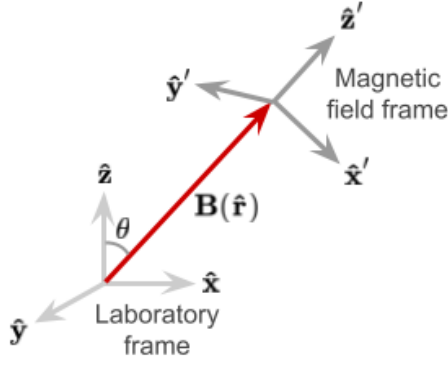


Figure 22 – Basis $A' = \{\hat{\mathbf{x}}', \hat{\mathbf{y}}', \hat{\mathbf{z}}'\}$ of the magnetic field frame in relation to the basis $A = \{\hat{\mathbf{x}}, \hat{\mathbf{y}}, \hat{\mathbf{z}}\}$ of the laboratory frame.

Source: By the author.

To account the magnetic field \mathbf{B} effect in $R_{i,j,l}$, we must analyse the magnetic field in a frame that defines the quantization axis parallel to \mathbf{B} . Let us consider the basis $A' = \{\hat{\mathbf{x}}', \hat{\mathbf{y}}', \hat{\mathbf{z}}'\}$ in the **magnetic field frame** as illustrated in figure 22. The polarization basis $\mathbf{B}' = \{\hat{\sigma}'_+, \hat{\sigma}'_-, \hat{\pi}'\}$ in the magnetic field frame is given by

$$\hat{\sigma}'_+ = \frac{\hat{\mathbf{x}}' + i\hat{\mathbf{y}}'}{\sqrt{2}}, \quad \hat{\sigma}'_- = \frac{\hat{\mathbf{x}}' - i\hat{\mathbf{y}}'}{\sqrt{2}}, \quad \hat{\pi}' = \hat{\mathbf{z}}' \parallel \mathbf{B}. \quad (4.5)$$

The polarization vector $\hat{\epsilon}_j$ of the j -th laser beam is then

$$[\hat{\epsilon}_j]_B = \begin{bmatrix} \epsilon_{i,\sigma_+} \\ \epsilon_{i,\sigma_-} \\ \epsilon_{i,\pi} \end{bmatrix} \Rightarrow \hat{\epsilon}_j = \epsilon_{i,\sigma_+} \hat{\sigma}_+ + \epsilon_{i,\sigma_-} \hat{\sigma}_- + \epsilon_{i,\pi} \hat{\pi}, \quad (4.6)$$

where $[\hat{\epsilon}_j]_B$ is a column matrix whose elements are the components of $\hat{\epsilon}_j$ on the laboratory basis B . Hence, the components of $\hat{\epsilon}_j$ on the magnetic field basis B' are

$$[\hat{\epsilon}_j]_{B'} = M[\hat{\epsilon}_j]_B, \quad (4.7)$$

where M is the change-of-basis matrix. We must consider two other change-of-basis matrices to obtain M . The first one is the matrix M' that change a polarization basis such as B to a Cartesian basis such as A . The second one is the rotation matrix $R(\theta)$. Thus, the change-of-basis M is given by

$$M = (M')^\dagger R(\theta) M', \quad (M')^\dagger = ((M')^*)^T = (M')^{-1}, \quad (4.8)$$

where

$$M' = \begin{bmatrix} 1/\sqrt{2} & 1/\sqrt{2} & 0 \\ -i/\sqrt{2} & i/\sqrt{2} & 0 \\ 0 & 0 & 1 \end{bmatrix}, \quad R(\theta) = \begin{bmatrix} 1 & 0 & 0 \\ 0 & \cos(\theta) & -\sin(\theta) \\ 0 & \sin(\theta) & \cos(\theta) \end{bmatrix}. \quad (4.9)$$

4.1.3 Transition probabilities

The transition probability $P_{i,j}$ is the probability of an atom at state i transiting to the state j by scattering a photon of the j -th laser in a nMOT arrangement. Let us impose the independent two-level systems assumption discussed in section 3.1.2 such that there will be three independent transitions for each laser beam. Thus,

$$P_{i,j} = \sum_{l=0}^2 P_{i,j,l}, \quad (4.10)$$

where $P_{i,j,l}$ is the probability of an atom at state i scattering a photon of the j -th laser due to the l -th electronic transition. This assumption is only valid when the Zeeman shift is strong enough to decouple the excited states so that we can neglect coherent transitions between them. Therefore, our model is reliable when the trapped atoms are far away from the magnetic field origin, which happens in the power-broadened and quantum regimes (see section 3.3.1). Although the quantum regime matches this condition, we are not analysing the atom dynamics in quantum mechanics since we are treating the atoms' position and velocity classically. Therefore, we expect that our model will fail in the Doppler and quantum regime.

The time derivative of $P_{i,j,l}$ is the scattering rate $R_{i,j,l}$ given by

$$R_{i,j,l} = \frac{\Gamma}{2} \frac{s(\mathbf{r})}{1 + s(\mathbf{r}) + (2\Delta_l/\Gamma)^2}, \quad s(\mathbf{r}) = \exp \left[-\frac{2(x^2 + y^2)}{w^2} \right], \quad \Delta_l = \delta + \delta_Z^{(l)} + \delta_D, \quad (4.11)$$

where w and δ is, respectively, the waist and the laser detuning of the j -th laser beam, $\delta_Z^{(l)}$ is the Zeeman shift due to the l transition given by equation (3.1), and $\delta_D = -\mathbf{k} \cdot \mathbf{v}_{i-1}$ is the Doppler shift. To increase accuracy, we are taking into account the Gaussian profile of the laser beams in $s(\mathbf{r})$. Hence, the probability $P_{i,j,l}$ of happening a scattering event during a small time interval δt can be approximate by

$$R_{i,j,l} = \frac{\partial P_{i,j,l}}{\partial t} \Rightarrow P_{i,j,l} \simeq R_{i,j,l} \delta t. \quad (4.12)$$

Each transition is associated with one laser polarization. The probability of a photon from the j -th laser beam having the polarization associated with the l -transition is $|\langle \hat{\epsilon}_j | \hat{\epsilon}_l \rangle|^2$, where $\hat{\epsilon}_l \in B'$. Thus, the transition probability $P_{i,j}$ is given by

$$P_{i,j} = \sum_l |\langle \hat{\epsilon}_j | \hat{\epsilon}_l \rangle|^2 P_{i,j,k} = \sum_l |\langle \hat{\epsilon}_j | \hat{\epsilon}_l \rangle|^2 R_{i,j,l} \delta t. \quad (4.13)$$

4.2 Input and outputs

Overall, the input of the simulation is divided into two categories: the **experiment** and the **performance parameters**. The experiment parameters include information

about the controllable quantities of a nMOT, such as the laser arrangement, the magnetic field profile, and the involved electronic transitions. It is essential to have detailed information about the nMOT in order to accurately obtain experimental quantities. The performance parameters define precision, execution time, and memory usage. We seek the optimisation of both time and spatial computational complexities. Hence, it is important to properly set up the performance parameters in order to execute a simulation in an acceptable period of time using the available memory.

The raw output of the simulation is six probability distributions of the atoms' position and velocity, as explained in Section 4.1.1. The position distributions are essential to obtaining experimental quantities related to the atomic cloud profile, such as the centre of mass and the cloud size. While the velocity distributions are relevant to obtaining the temperature.

4.2.1 Input

The **experiment parameters** are presented in three groups: the laser arrangement, the magnetic field profile, and the involved electronic transition. All groups are shown in tables 1, 2, and 3. Table 1 contains essential information to define the involved electronic transition as well as the atoms' mass, which is crucial for evaluating the scattering rates (4.11) and therefore the transition probabilities (4.13). Table 2 contains the magnetic field profile. Besides the quadrupole magnetic field already mentioned in previous sections, some experiments also have a residual linear gradient and a constant magnetic field to control the magnetic field origin. Lastly, table 3 defines the laser beam arrangement.

Table 1 – Simulation parameters that defines the involved electronic transition and the mass of the atoms.

Symbol	Description	Unit
Γ	Natural linewidth	$2\pi \times kHz$
λ	Resonance wavelength	nm
J_{gnd}	Total angular momentum of the ground state	dimensionless
J_{exc}	Total angular momentum of the excited state	dimensionless
g_{gnd}	<i>Landé</i> factor of the ground state	dimensionless
g_{exc}	<i>Landé</i> factor of the excited state	dimensionless
m	Atomic mass	Da (Dalton unit)

Source: By the author.

The **performance parameters** are shown in table 4. Let us discussed each of them. The parameter t_w is the period of time in which we do not get samples. This parameter defines a moment at which equilibrium has already been reached. We set its value by analysing the variation of the atom's position. Thus, we only get samples during

Table 2 – Simulation parameters that defines the magnetic field profile.

Symbol	Description	Unit
B_0	Magnetic field gradient in equation (3.13)	G/cm
B_{axial}	Axial direction of the magnetic field	3D vector
B_{ingrad}	Residual magnetic field gradient	3D vector
B_{bias}	Constant magnetic field	3D vector

Source: By the author.

Table 3 – Simulation parameters that defines the laser beams arrangement.

Symbol	Description	Unit
δ	Laser detuning	$2\pi \times kHz$
s_0	Saturation parameter	dimensionless
w	Waist	cm
$\hat{\mathbf{k}}$	Wavevector direction	3D vector
$\hat{\epsilon}$	Polarization vector in the laboratory frame	3D vector

Source: By the author.

the interval $t - t_w$. The last time parameter is the time resolution from equations (4.1) and (4.2). The parameters t , r_m , and v_m define the conditions to stop the simulation, which are

- If the simulation time is greater than t ;
- If the atom trespasses the sphere of radius r_m ;
- If the atom's velocity is greater than v_m .

The position and velocity resolution are defined by the parameters N_r , r_m , v_m . The spatial resolution is $\delta r = r_m/N_r$, whilst the speed resolution is $\delta v = v_m/N_r$. Hence, the atoms' positions x , y , and z are multiples of δ_r , whereas the atoms' velocities v_x , v_y , and v_z are multiples of δ_v . The number of samples N_s is basically the number of ensembles (atoms' motions), which defines the precision of the output. Lastly, the initial temperature T_0 defines the initial atoms' velocities by sampling the **Maxwell-Boltzmann distribution**.

4.2.2 Output

The raw output of the simulation consists of six probability distributions that describe the atoms' motion. These distributions can be divided into two groups: **position** and **velocity distributions**. Although these are continuous quantities, our model reproduces discrete values. Hence, the atoms' position and velocities are then restricted to the

Table 4 – Simulation performance parameters.

Symbol	Description	Unit
t	Maximum time of simulation	ms
t_w	Waiting time	ms
δt	Time resolution	ms
r_m	Maximum distance of the origin	cm
v_m	Maximum speed	cm/s
N_s	Number of samples	dimensionless
N_r	Resolution number	dimensionless
N_p	Number of parallel tasks	dimensionless
T_0	Initial temperature	μK

Source: By the author.

following space

$$\mathbf{r} = (i_x \hat{\mathbf{x}} + i_y \hat{\mathbf{y}} + i_z \hat{\mathbf{z}}) \delta r, \quad (4.14)$$

$$\mathbf{v} = (j_x \hat{\mathbf{x}} + j_y \hat{\mathbf{y}} + j_z \hat{\mathbf{z}}) \delta v, \quad (4.15)$$

where i_x , i_y , i_z , j_x , j_y , and j_z are positive integers, and δr and δv are the spatial and speed resolution respectively. The joint probability distribution d_r of the atoms' position is given by

$$d_r(i_x, i_y, i_z) = d_x(i_x) d_y(i_y) d_z(i_z), \quad (4.16)$$

$$\sum_V d_r(i_x, i_y, i_z) \rightarrow \text{Probability of finding an atom in the volume } V, \quad (4.17)$$

where d_x , d_y , and d_z are marginal probability distributions. The equation (4.16) assumes independence between each direction. Similarly, the joint probability distribution d_v of the atoms' velocity is given by

$$d_v(i_{v_x}, i_{v_y}, i_{v_z}) = d_{v_x}(i_{v_x}) d_{v_y}(i_{v_y}) d_{v_z}(i_{v_z}), \quad (4.18)$$

$$\sum_{\Delta v} d_v(i_{v_x}, i_{v_y}, i_{v_z}) \rightarrow \text{Probability of finding an atom with velocities } \Delta v, \quad (4.19)$$

We are interested in two atomic cloud quantities: the centre of mass and the cloud size. The centre of mass is given by,

$$\mathbf{r}_c = \langle d_x \rangle \hat{\mathbf{x}} + \langle d_y \rangle \hat{\mathbf{y}} + \langle d_z \rangle \hat{\mathbf{z}}, \quad (4.20)$$

where $\langle d_x \rangle$, $\langle d_y \rangle$, and $\langle d_z \rangle$ are averages. The cloud sizes are

$$\sigma_x = \sqrt{\langle (d_x - \langle d_x \rangle)^2 \rangle}, \quad \sigma_y = \sqrt{\langle (d_y - \langle d_y \rangle)^2 \rangle}, \quad \sigma_z = \sqrt{\langle (d_z - \langle d_z \rangle)^2 \rangle}, \quad (4.21)$$

where σ_x , σ_y , σ_z are standard deviations.

We are also interested in temperature, which is evaluated by the equipartition theorem given by

$$\frac{3}{2} k_B T = \frac{m}{2} (\langle d_{v_x}^2 \rangle + \langle d_{v_y}^2 \rangle + \langle d_{v_z}^2 \rangle) \Rightarrow T = \frac{m}{3k_B} (\langle d_{v_x}^2 \rangle + \langle d_{v_y}^2 \rangle + \langle d_{v_z}^2 \rangle). \quad (4.22)$$

5 RESULTS

In order to validate our model, we estimated the experimental quantities of three nMOT arrangements reproduced by different laboratories. One traps dysprosium atoms, whereas the other two trap strontium atoms. We chose those experiments since their narrownesses are small enough to reach the power-broadened regime, which is a requirement of our model. In this chapter, we present the estimated quantities and compare them to experimental measures.

5.1 Dysprosium

The dysprosium nMOT (43) reproduced by Davide Dreon and his research group matches the conditions of our experiment and is thoroughly detailed in the Dreon PhD thesis (1), which helps us improve accuracy as discussed in Section 4.2. Also, our research group is preparing a similar experimental setup in order to study dipolar quantum gases by making use of the large magnetic dipole moment of dysprosium. Moreover, the involved electronic transition presented in Table 5 yields a narrowness of $\eta = 43.8$ from equation (3.16) and $R = 169.3$ from equation (3.15), which are not ideal values. However, the experimental setup is designed to decrease the MOT force in the gravity direction, allowing the atoms to fall under gravity. Therefore, even with a non-ideal narrowness, Dreon nMOT is able to reach the power-broadened regime and then satisfy our model requirements.

Table 5 – Parameters of the involved electronic transition from the Dreon nMOT.

Symbol	Quantity	Value
$\Gamma/2\pi$	Natural Linewidth	136 <i>kHz</i>
λ	Resonant wavelength	626 <i>nm</i>
J_{gnd}	Ground state angular momentum	8
g_{gnd}	Ground state Landé factor	1.24
J_{exc}	Excited state angular momentum	9
g_{exc}	Excited state Landé factor	1.29
m	Mass	164 <i>u</i>

Source: DREON. (1).

The involved transition is more complicated than the one present in Chapter 4 since it has 36 possible states in the presence of a magnetic field due to the large angular momenta $|J = 8\rangle \rightarrow |J = 9\rangle$. However, in the power-broadened regime, the dysprosium atoms gather in a region with a large and negative magnetic field, which leads to a large and positive Zeeman shift so that an efficient optical pumping populates the absolute

ground state $|J = 8, m_J = -8\rangle$. This spin-polarization was observed experimentally for nMOTs with lanthanide atoms (45, 46) and also in the Dreon experiment. Therefore, due to selection rules (see Appendix C), we can simplify the transitions to a four-level system as illustrated in Figure 23a and then apply our model under the three independent two-level systems assumption.

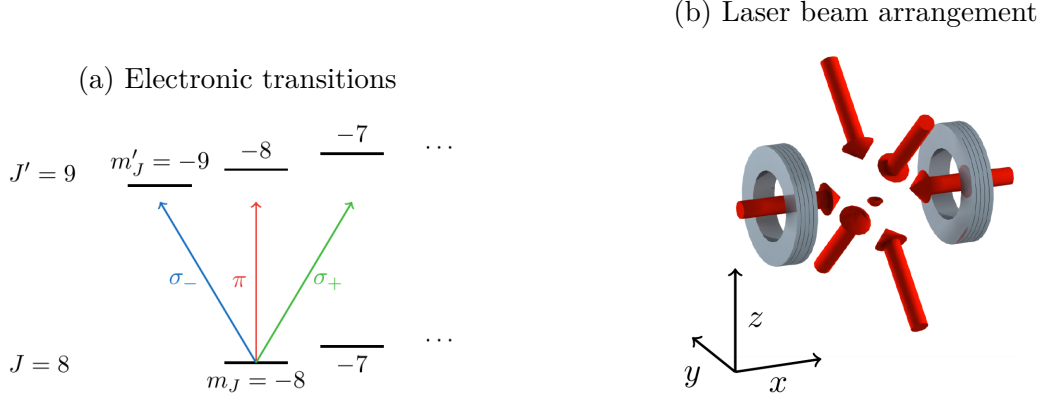


Figure 23 – (a) Electronic transitions of spin-polarized dysprosium atoms and (b) laser beam arrangement and Helmholtz coils setup from the Dreon nMOT.

Source: DREON. *et al.* (43).

The arrangement of the lasers is not the usual one introduced in Section 3.2, where we have a pair of counter-propagating laser beams in the gravity direction. In the Dreon setup, there are two pairs of counter-propagating laser beams forming an angle of 45 degrees with the gravity direction, as illustrated in Figure 23b. Moreover, the strong and negative magnetic field component is perpendicular to the gravity direction so that the laser beams in this direction have different polarization than the other ones. This setup was designed to decrease the MOT force in the gravity direction and then guarantee that the atoms fall below the magnetic field origin. The parameters of the laser arrangement and the magnetic field profile are presented in Tables 6 and 7.

5.1.1 Atomic cloud profile

The in-situ and estimated atomic cloud profiles are shown in Figures 24a and 24b. The larger the laser detuning, the lower the centre of mass, and the more spread the atomic cloud. The atomic cloud distributions resemble an ellipsoid whose semi-major axis is perpendicular to the gravity direction. Those are typical effects of power-broadened nMOTs, regardless the slightly large narrowness.

From equation (3.20), we expect that the centre of mass¹ of the atomic cloud is

¹ We are considering only the z component as the centre of mass since all other components is about zero in all cases.

Table 6 – Wave vector direction (x, y, z) and polarization $(\sigma_+, \sigma_-, \pi)$ in the laboratory frame (see Section 4.1.2) from Dreon nMOT. All laser beams are set up with the saturation parameter $s_0 = 0.65$ and waist 2.0 cm .

Wave vector (arb. unit.)	Polarization
$(1, 0, 0)$	$(0, 1, 0)$
$(-1, 0, 0)$	$(0, 1, 0)$
$(0, 1, 1)$	$(1, 0, 0)$
$(0, -1, 1)$	$(1, 0, 0)$
$(0, 1, -1)$	$(1, 0, 0)$
$(0, -1, -1)$	$(1, 0, 0)$

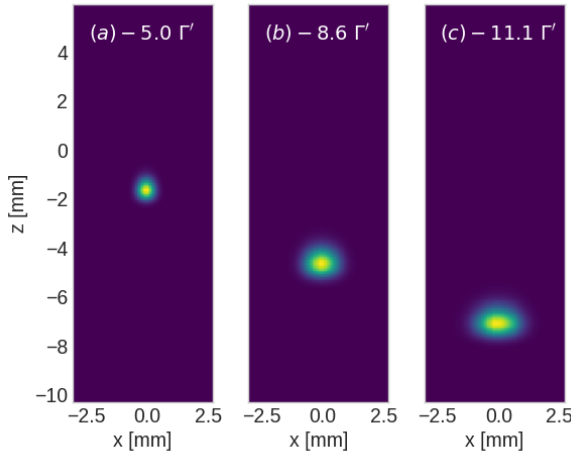
Source: DREON. *et al.* (43).

Table 7 – Parameters that defined the magnetic field profile from Dreon nMOT.

Symbol	Quantity	Value
B_0	Axial gradient	$1.71 G$
B	Magnetic Field	$B_0(-\hat{x} + \hat{y}/2 + \hat{z}/2)$
B_{bias}	Bias	$(-0.094 \hat{z}) \text{ G/cm}$

Source: DREON. *et al.* (43).

(a) Simulated atomic cloud



(b) In-situ atomic cloud

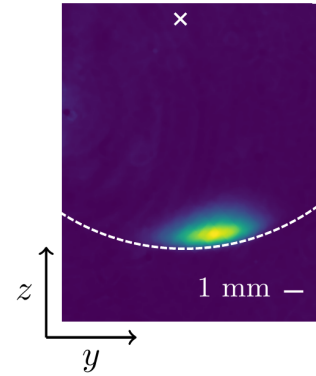


Figure 24 – (a) Estimated atomic cloud profile for different laser detunings based on equation (4.16). (b) In-situ atomic cloud profiles from the Dreon nMOT.

Source (a): By the author; (b): DREON. *et al.* (43).

proportional to the laser detuning for large detunings. In fact, the estimated centre of mass given by equation (4.20) and the experimental measures confirm this linear relation

for laser detunings roughly larger than $2\pi \times 700 \text{ kHz} \simeq 4\Gamma'$, as illustrated in Figure 25. However, the theoretical centre of mass is not as accurate as the estimated one since there is a difference of about 1mm between the experimental and theoretical centre of mass, whereas the estimated values match almost perfectly the experimental measures.

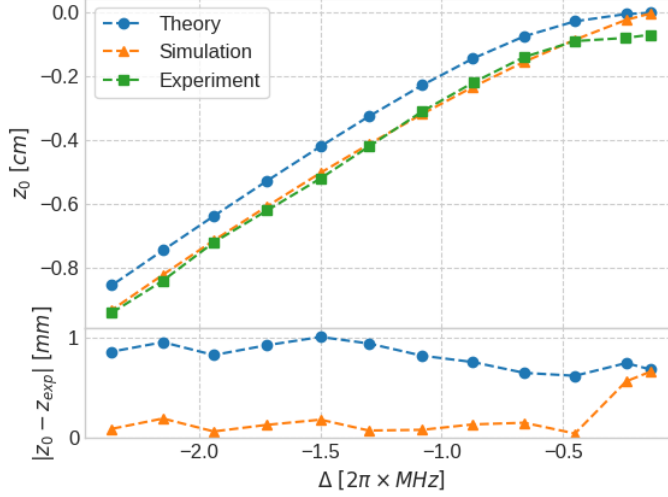


Figure 25 – The gravity direction component of the centre of mass as a function of the laser detuning. The blue spheres, orange triangles, and green squares are, respectively, the theoretical centres of mass from equation (3.20), estimated points, and experimental measures from (1).

Source: By the author.

We do not expect an accurate estimative of the cloud size since this quantity is affected by interactions between atoms, which are not taken into account in our model. Indeed, the experimental cloud sized is larger than the estimated ones given by equation (4.21), as illustrated in Figure 26a. This is expected due to the re-absorption of scattered photons. Nevertheless, we are able to compare the experimental and estimated cloud sizes more clearly by verifying the ratio between two cloud size components, as illustrated in Figure 26b. It was observed in previous works (41) that the cloud size is proportional to the cube root of the number of trapped atoms $\sqrt[3]{N}$ as discussed in Section 3.2.2. Therefore, we remove the effect of scaling constants by analysing the ratio between components. The experimental and estimated cloud sizes match roughly in the laser detuning range of $-10\Gamma'$ to $-4\Gamma'$ ($-2\pi \times 1750\text{kHz}$ to $-2\pi \times 700\text{kHz}$). We expect that the estimated cloud sizes do not match the experimental ones for lower detunings (in module) because we are out of the power-broadened regime. Although there are no experimental measures available in this range, we can observe that there are variations inconsistent with the range in which there is agreement between experimental and estimated values. For laser detunings larger than $10\Gamma'$ in module, we do not have a good matching mostly due to the σ_y values. To explain such divergence, we must consider that an ellipsoid bounds the region in which

the atoms can be trapped. The curvature effect is particularly predominant in the x and y directions and can invalidate the scaling factor $\sqrt[3]{N}$.

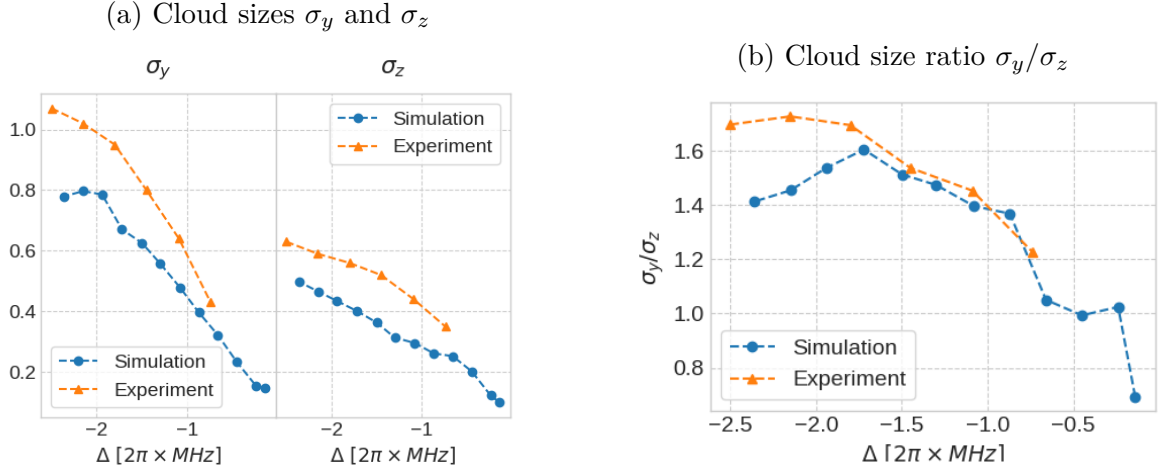


Figure 26 – (a) Cloud sizes σ_y and σ_z and (b) cloud ratio σ_y/σ_z as a function of the laser detuning. The blue spheres and orange triangles are the estimated and experimental cloud sizes respectively.

Source: By the author.

5.1.2 Temperature

The experimental and estimated temperatures are shown in Figure 27. Firstly, both estimated and experimental temperatures are higher than the theoretical temperature $T_D = 4.19 \mu K$ given by equation (3.9). For laser detunings roughly larger than $6\Gamma' \simeq 7.5\Gamma$ in module, the experimental measures match the estimated values. In this range, the temperature is approximately constant, which agrees with the theoretical temperature given by equation (3.9). However, the absolute theoretical value does not match the experimental measures. For detunings roughly lower than $6\Gamma'$, the experimental temperatures increases with the laser detuning whereas the estimated values decreases. In this range, the nMOT is not in the power-broadened regime.

5.2 Strontium

We estimate quantities from two strontium nMOTs. The first one, reproduced by Thomas Loftus (34) and his research group, was used to estimate quantities related to the atomic cloud profile. The second one was used to analyse temperature and was reproduced by the research group of the professor Raul C. Teixeira at Federal University of São Carlos. We shall call each experiments **Loftus nMOT** and **IFSC nMOT**, respectively. Both use the same electronic transition presented in Table 8, whose narrowness is $\eta = 1.6$ from

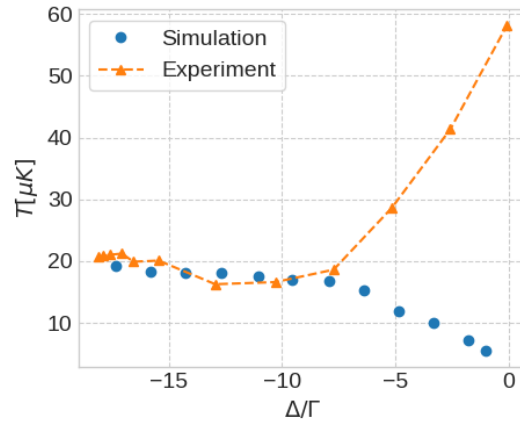


Figure 27 – Temperature of the Dreon nMOT as a function of the laser detuning. The blue spheres and the orange triangles are the estimated and experimental temperatures respectively. We can roughly split the temperatures into two regions at the laser detuning $-6\Gamma' \simeq 7.5\Gamma$. For detunings lower than $6\Gamma'$ in module, the nMOT is not in the power-broadened regime and then present a divergence between experimental and estimated values.

Source: By the author.

equation (3.16) and $R = 15.8$ from equation (3.15). Since these values are lower than the Dreon nMOT, it is easier to reach the power-broadened regime since the MOT forces will be much lower. Moreover, this transition is the same as the one analysed in Chapter 3 and therefore it does not depend on the spin-polarization phenomenon as the Dreon nMOT.

Table 8 – Electronic transition parameters from the Loftus nMOT and the IFSC nMOT.

Symbol	Quantity	Value
$\Gamma/2\pi$	Natural Linewidth	7.5 kHz
λ	Resonant wavelength	689 nm
J_{gnd}	Ground state angular momentum	0
g_{gnd}	Ground state Landé factor	0
J_{exc}	Excited state angular momentum	1
g_{exc}	Excited state Landé factor	1.5
m	Mass	88 u

Source: LOFTUS. *et al.* (34). TEXEIRA.*et al.*²

Both Loftus nMOT and IFSC nMOT have the same arrangement as shown in Section 3.2. The laser beam setup and the magnetic field profile are presented in Tables 9, 10, and 11. The polarization of the laser beams in the gravity direction are different than

² Professor Raul. C. Teixeira and his group at Federal University of São Carlos reproduced the IFSC nMOT.

the polarization of the other ones since the negative component of the magnetic field is in this direction.

Table 9 – Wave vector direction (x, y, z) and polarization $(\sigma_+, \sigma_-, \pi)$ in the laboratory frame (see Section 4.1.2) from the Loftus nMOT and the IFSC nMOT. The laser beams of the Loftus nMOT have the saturation parameter $s_0 = 248$ and waist $w = 2.6 \text{ cm}$, whereas the laser beams of the IFSC nMOT have $s_0 = 102$ and $w = 6.0 \text{ cm}$.

Wave vector (arb. unit.)	Polarization
(1, 0, 0)	(1, 0, 0)
(-1, 0, 0)	(1, 0, 0)
(0, 1, 0)	(1, 0, 0)
(0, -1, 0)	(1, 0, 0)
(0, 0, 1)	(0, 1, 0)
(0, 0, -1)	(0, 1, 0)

Source: LOFTUS. *et al.* (34). TEXEIRA. *et al.*

Table 10 – Parameters of the magnetic field profile from the Loftus nMOT.

Symbol	Quantity	Value
B_0	Axial gradient	$10G/cm$
B	Magnetic Field	$B_0(\hat{x}/2 + \hat{y}/2 - \hat{z})$
B_{bias}	Bias	0

Source: LOFTUS. *et al.* (34).

Table 11 – Parameters of the magnetic field profile from the IFSC nMOT.

Symbol	Quantity	Value
B_0	Axial gradient	$5G/cm$
B	Magnetic Field	$B_0(\hat{x}/2 + \hat{y}/2 - \hat{z})$
B_{bias}	Bias	0

Source: TEXEIRA. *et al.*

5.2.1 Atomic cloud profile

The in-situ and estimated atomic cloud profiles from the Loftus nMOT are shown in Figures 28b and 28a. They are similar to the Dreon profiles, as discussed in Section 5.2.1, but the eccentricities of the Loftus profiles are larger than those of the Dreon since the MOT forces are smaller. Moreover, the ellipsoid that bounds the atomic cloud is more

clear for the Loftus nMOT, such that its bottom is clearly visible. Overall, the Loftus nMOT exhibits the properties of power-broadened nMOTs more clearly than the Dreon nMOT due to its smaller narrowness.

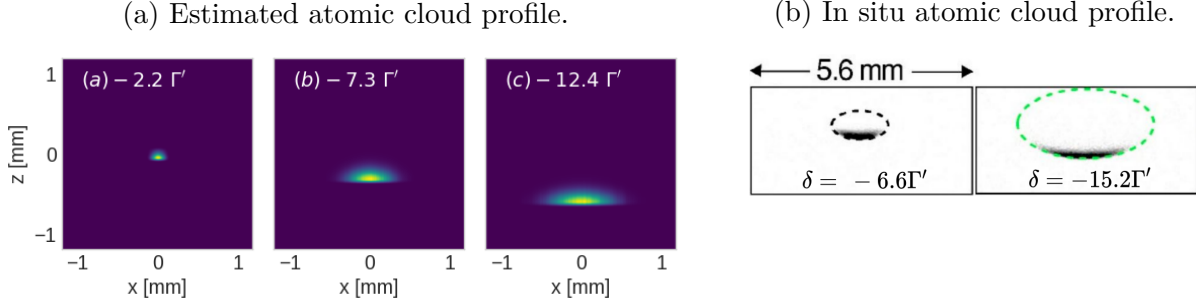


Figure 28 – (a) Estimated atomic cloud profile for different laser detunings based on equation (4.16). (b) In-situ atomic cloud profiles from the Loftus nMOT.

Source (a): By the author; (b): LOFTUS. *et al.* (34).

The theoretical centre of mass given by equation (3.20) fits perfectly the estimated values roughly about $\Delta = -5\Gamma'$, as shown in Figure (29). For laser detunings roughly below $5\Gamma'$ in module, we consider that nMOT is not in the power-broadened regime. Both estimated and theoretical centre of mass are about 0.1mm above the experimental measures.

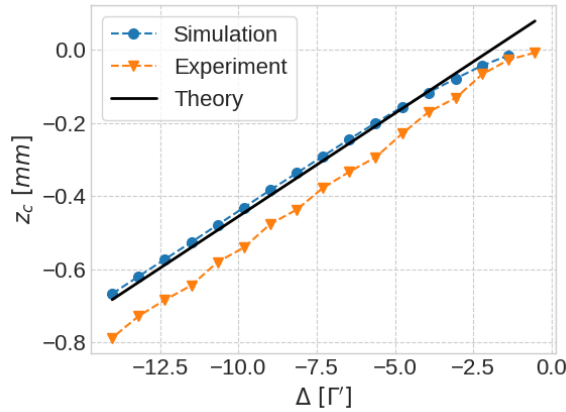


Figure 29 – Centre of mass as a function of the laser detunings from the Loftus nMOT. The blue spheres, orange triangles, and black line are the estimated, experimental, and theoretical centre of mass respectively.

Source: By the author.

We do not find experimental measures of the cloud size from the Loftus nMOT. Nevertheless, we obtained the cloud sizes based on equation (4.21), as illustrated in Figure

30. The x and y cloud size components is essentially the same since the MOT force are symmetrical in these directions. The the larger the laser detuning module, the more spread the atomic cloud is in the directions perpendicular to the gravity. The z component of the cloud size has a different behaviour. Roughly about $\Delta = -6\Gamma'$, σ_z becomes constant $-0.5nm$.

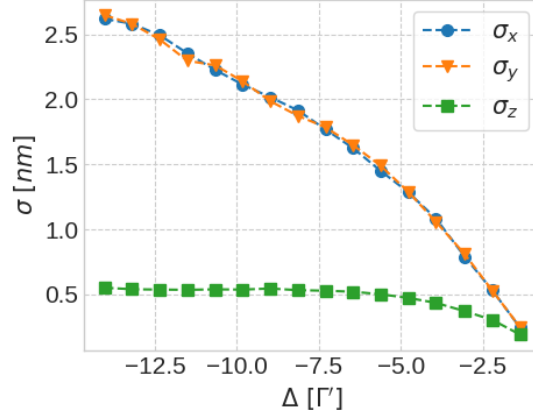


Figure 30 – Cloud sizes components from the Loftus nMOT as a function of the laser detuning. The blue spheres, orange triangles, and green squares are the estimated x , y , and z cloud size components respectively.

Source: By the author.

5.2.2 Temperature

We simulate two sets of temperatures presented in Figures 31a and 31a by fixing either the saturation parameter or the laser detuning. In the first one, for detunings roughly smaller than $-4\Gamma'$, the experimental temperatures increases with the laser detuning whereas the estimated values decrease, as the Dreon nMOT. Therefore, in this range, the nMOT is not in the power-broadened regime. In the complementary range, the estimated temperature is approximately constant and equals to $4\mu K$ whereas the experimental temperatures slowly increases from $4\mu K$ to $5.5\mu K$ so that the maximum divergence is $1.5\mu K$. The theoretical temperature given by equation (3.9) is $1.8\mu K$, which is smaller than both estimated and experimental values. In the second set of temperatures, for saturation parameters roughly smaller than 450, the maximum divergence is $1\mu K$, whereas for the complementary range, the maximum divergence increases to $6\mu K$. In both sets of temperatures, the experimental values are closer to the estimated values than the theoretical ones.

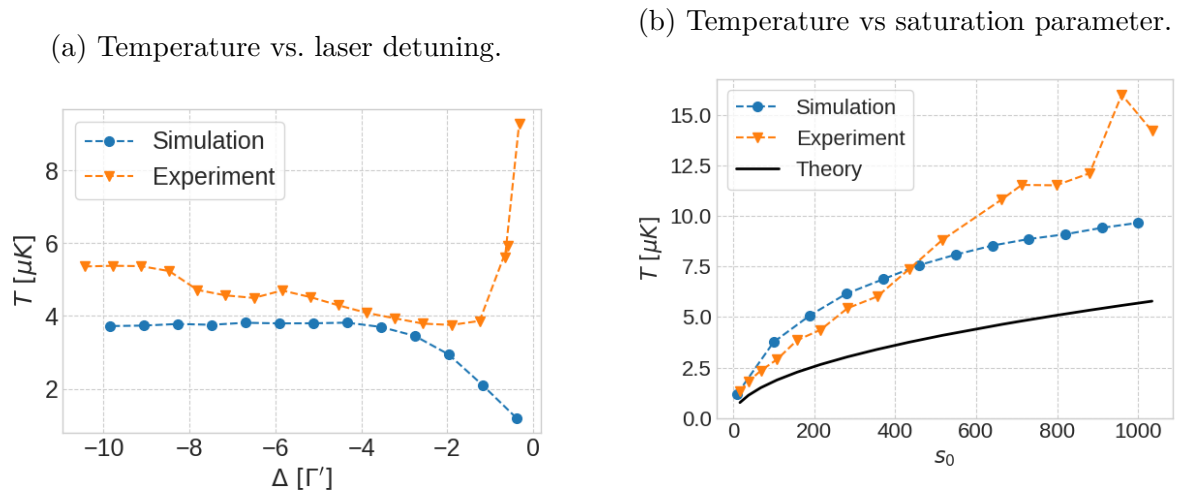


Figure 31 – (a) Temperature as a function of the laser detuning for a saturation parameter of $s = 102$. (b) Temperature as a function of the saturation parameter for a laser detuning of $\delta = -3.1 \text{ MHz}$. The blue spheres and orange triangles are the estimated and experimental values from the IFSC nMOT respectively.

Source: By the author.

6 CONCLUSION

In this Master's degree work, we proposed and implemented a Monte Carlo simulation to estimate experimental quantities of narrow-line magneto-optical traps. We essentially estimate the probability distributions of the atoms' position and velocity in the presence of laser light and a quadrupole magnetic field. Then, with these distributions, we estimate the atomic cloud profile and the temperature. Our proposal is to sample the atoms' states by considering their movement as a Markovian process.

We were able to simulate three nMOT arrangements reproduced by different laboratories and obtain estimated quantities that are more accurate than the theoretical ones. It is possible to use our simulation to optimize parameters of nMOTs without the necessity of experimental data. It is also a tool to analyse the feasibility of unusual nMOT arrangements such as nMOTs with fewer laser beams.

We analysed the limits of our model regarding the three nMOT regimes and verified that it works exclusively in the power-broadened regime. Therefore, to obtain accurate quantities, it is necessary to guarantee a set of parameters that keep the nMOT in this regime. We validated our model for nMOTs with small and slightly large narrownesses. It is possible to estimate quantities for both cases, but the larger the narrowness, the more difficult it is to reach the power-broadened regime. Hence, nMOTs with small narrownesses have a larger range in which we are able to predict experimental quantities. The nMOT setup with a slightly large narrowness must be designed to decrease the trapping effect in the gravity direction so that the atoms are able to fall under gravity. This is a typical effect of power-broadened nMOTs.

We confirmed that our simulation is capable of estimating quantities for complicated transitions by assuming the spin-polarized atoms. In our model, we are assuming that the transition is a four-level system. The dysprosium nMOT presented in Section 5.1 is based on an electronic transition with 36 states. Nevertheless, we were able to estimate quantities by assuming spin-polarized atoms based on previous works in which this phenomenon was observed experimentally.

REFERENCES

- 1 DREON, D. **Designing and building an ultracold Dysprosium experiment: a new framework for light-spin interaction.** 2017. PhD Thesis (Doctor) — Paris Sciences Lettres Research University, 2017.
- 2 PETERS, A.; CHUNG, K. Y.; CHU, S. High-precision gravity measurements using atom interferometry. **Metrologia**, v. 38, n. 1, p. 25, 2001.
- 3 MUKAMEL, S. *et al.* Roadmap on quantum light spectroscopy. **Journal of Physics B: atomic, molecular and optical physics**, v. 53, n. 7, p. 072002, 2020.
- 4 CHU, S. Nobel lecture: The manipulation of neutral particles. **Reviews of Modern Physics**, v. 70, n. 3, p. 685, 1998.
- 5 COHEN-TANNOUDJI, C. N. Nobel lecture: Manipulating atoms with photons. **Reviews of Modern Physics**, v. 70, n. 3, p. 707, 1998.
- 6 PHILLIPS, W. D. Nobel lecture: laser cooling and trapping of neutral atoms. **Reviews of Modern Physics**, v. 70, n. 3, p. 721, 1998.
- 7 METCALF, H. J.; STRATEN, P. Van der. Laser cooling and trapping of neutral atoms. Available at: <https://onlinelibrary.wiley.com/doi/epdf/10.1002/9783527600441.oe005>. Access at: 23 Jan. 2023.
- 8 LUDLOW, A. D. *et al.* Optical atomic clocks. **Reviews of Modern Physics**, v. 87, n. 2, p. 637, 2015.
- 9 SCHNEIDER, P.-I.; SAENZ, A. Quantum computation with ultracold atoms in a driven optical lattice. **Physical Review A**, v. 85, n. 5, p. 050304, 2012.
- 10 ZHANG, X.; YE, J. Precision measurement and frequency metrology with ultracold atoms. **National Science Review**, v. 3, n. 2, p. 189–200, 2016.
- 11 CORNELL, E. A.; WIEMAN, C. E. Nobel lecture: Bose-Einstein condensation in a dilute gas, the first 70 years and some recent experiments. **Reviews of Modern Physics**, v. 74, n. 3, p. 875, 2002.
- 12 KETTERLE, W. Nobel lecture: When atoms behave as waves: Bose-Einstein condensation and the atom laser. **Reviews of Modern Physics**, v. 74, n. 4, p. 1131, 2002.
- 13 KRZYSZTOF, K. *et al.* Magneto-optical trap: fundamentals and realization. **Computational Methods in Science and Technology**, n. 2, p. 115–129, 2010. DOI: 10.12921/cmst.2010.SI.02.115-129.
- 14 FRISCH, A. *et al.* Narrow-line magneto-optical trap for erbium. **Physical Review A**, v. 85, n. 5, p. 051401, 2012.
- 15 MAIER, T. *et al.* Narrow-line magneto-optical trap for dysprosium atoms. **Optics Letters**, v. 39, n. 11, p. 3138–3141, 2014.

- 16 MIYAZAWA, Y. *et al.* Narrow-line magneto-optical trap for europium. **Physical Review A**, v. 103, n. 5, p. 053122, 2021.
- 17 LETT, P. D. *et al.* Observation of atoms laser cooled below the doppler limit. **Physical Review Letters**, v. 61, n. 2, p. 169, 1988.
- 18 GATTOBIGIO, G. *et al.* Scaling laws for large magneto-optical traps. **Physica Scripta**, v. 81, n. 2, p. 025301, 2010.
- 19 LOO, F. *et al.* Investigations of a two-level atom in a magneto-optical trap using magnesium. **Journal of Optics B: quantum and semiclassical optics**, v. 6, n. 1, p. 81, 2003.
- 20 BALYKIN, V.; MINOGIN, V.; LETOKHOV, V. Electromagnetic trapping of cold atoms. **Reports on Progress in Physics**, v. 63, n. 9, p. 1429, 2000.
- 21 CHAUDHURI, S.; ROY, S.; UNNIKRISHNAN, C. Realization of an intense cold rb atomic beam based on a two-dimensional magneto-optical trap: experiments and comparison with simulations. **Physical Review A**, v. 74, n. 2, p. 023406, 2006.
- 22 ATUTOV, S. *et al.* Sodium mot collection efficiency as a function of the trapping and repumping laser frequencies and intensities. **European Physical Journal D - atomic, molecular, optical and plasma physics**, v. 13, n. 1, p. 71–82, 2001.
- 23 HANLEY, R. K. *et al.* Quantitative simulation of a magneto-optical trap operating near the photon recoil limit. **Journal of Modern Optics**, v. 65, n. 5-6, p. 667–676, 2018.
- 24 WEINER, J.; HO, P.-T.; DEE, K. C. **Light-matter interaction: fundamentals and applications**. New York: Wiley Online Library, 2003. v. 1.
- 25 FOOT, C. J. *et al.* **Atomic physics**. Oxford: Oxford University Press, 2005. v. 7.
- 26 STECK, D. A. Quantum and atom optics. 2007. Available at: <http://info.phys.unm.edu/~ideutsch/Classes/Phys581S23/Reference%20Material%EF%80%A8/Steck%20quantum%20optics.pdf>. Accessible at: 23 Jan. 2023. Access at: 23 Jan. 2023.
- 27 VALVERDE, C.; BASEIA, B.; BAGNATO, V. Mecanismos de alargamento de linhas espectrais atômicas. **Revista Brasileira de Ensino de Física**, v. 38, n. 4, p. e4302, 2016.
- 28 REINAUDI, G. *et al.* Strong saturation absorption imaging of dense clouds of ultracold atoms. **Optics Letters**, Optical Society of America, v. 32, n. 21, p. 3143–3145, 2007.
- 29 SMITH, D. A. *et al.* Absorption imaging of ultracold atoms on atom chips. **Optics Express**, Optical Society of America, v. 19, n. 9, p. 8471–8485, 2011.
- 30 SHU-BIN, Y. *et al.* Absorption spectroscopy of cold caesium atoms confined in a magneto-optical trap. **Chinese Physics**, v. 13, n. 10, p. 1669, 2004.
- 31 TORREY, H. Transient nutations in nuclear magnetic resonance. **Physical Review**, v. 76, n. 8, p. 1059, 1949.

-
- 32 PERRIN, H. Doppler cooling and magneto-optical trapping. **Part of the Les Houches lectures on laser cooling and trapping**, 2014. Available at: http://www-lpl.univ-paris13.fr/bec/BEC/Teaching/lecture2_2012.pdf. Access at: 30 Apr. 2022.
- 33 PRUDNIKOV, O.; TAICHENACHEV, A.; YUDIN, V. Three-dimensional theory of the magneto-optical trap. **Journal of Experimental and Theoretical Physics**, v. 120, n. 4, p. 587–594, 2015.
- 34 LOFTUS, T. H. *et al.* Narrow line cooling and momentum-space crystals. **Physical Review A**, v. 70, n. 6, p. 063413, 2004.
- 35 CHOI, S.-K. *et al.* Three-dimensional analysis of the magneto-optical trap for (1+3)-level atoms. **Physical Review A**, v. 77, n. 1, p. 015405, 2008.
- 36 GAJDA, M.; MOSTOWSKI, J. Three-dimensional theory of the magneto-optical trap: Doppler cooling in the low-intensity limit. **Physical Review A**, American Physical Society, v. 49, p. 4864–4875, Jun 1994. DOI: 10.1103/PhysRevA.49.4864.
- 37 BERMAN, P. R.; MALINOVSKY, V. S. **Principles of laser spectroscopy and quantum optics**. Princeton: Princeton University Press, 2011.
- 38 RAAB, E. L. *et al.* Trapping of neutral sodium atoms with radiation pressure. **Physical Review Letters**, v. 59, n. 23, p. 2631, 1987.
- 39 KATORI, H. *et al.* Magneto-optical trapping and cooling of strontium atoms down to the photon recoil temperature. **Physical Review Letters**, v. 82, n. 6, p. 1116, 1999.
- 40 ZACHOROWSKI, J.; PALASZ, T.; GAWLIK, W. Magneto-optical trap for rubidium atoms. **Optica Applicata**, v. 28, p. 239–248, 1998.
- 41 CAMARA, A.; KAISER, R.; LABEYRIE, G. Scaling behavior of a very large magneto-optical trap. **Physical Review A**, v. 90, p. 063404, Dec 2014. DOI: 10.1103/PhysRevA.90.063404.
- 42 COURTEILLE, P. W. Atom-light interaction and basic applications. 2019. Available at: <https://www.ifsc.usp.br/~strontium/Publication/Scripts/LightAtomsLecture.pdf>. Access at: 23 Jan. 2023.
- 43 DREON, D. *et al.* Optical cooling and trapping of highly magnetic atoms: the benefits of a spontaneous spin polarization. **Journal of Physics B: atomic, molecular and optical physics**, IOP Publishing, v. 50, n. 6, p. 065005, 2017.
- 44 WASSERMAN, L. **All of statistics: a concise course in statistical inference**. New York: Springer, 2004. v. 26. (Springer texts in statistics, v. 26).
- 45 LU, M. *et al.* Strongly dipolar bose-Einstein condensate of dysprosium. **Physical Review Letters**, v. 107, n. 19, p. 190401, 2011.
- 46 AIKAWA, K. *et al.* Bose-Einstein condensation of erbium. **Physical Review Letters**, v. 108, n. 21, p. 210401, 2012.
- 47 BRASIL, C. A.; FANCHINI, F. F.; NAPOLITANO, R. d. J. A simple derivation of the lindblad equation. **Revista Brasileira de Ensino de Física**, v. 35, n. 1, p. 01–09, 2013.

48 KUHR, S. *et al.* Deterministic delivery of a single atom. **Science**, v. 293, n. 5528, p. 278–280, 2001.

49 FUHRMANEK, A. *et al.* Imaging a single atom in a time-of-flight experiment. **New Journal of Physics**, v. 12, n. 5, p. 053028, 2010.

50 BÜCKER, R. *et al.* Single-particle-sensitive imaging of freely propagating ultracold atoms. **New Journal of Physics**, v. 11, n. 10, p. 103039, 2009.

APPENDIX A – Density operator

The density operator represents an **ensemble** of identical systems in different quantum states. Let us consider a system which can be found in a quantum state $|\psi_k\rangle$ with probability P_k . This system is represented by the following density operator

$$\hat{\rho} \equiv \sum_k P_k |\psi_k\rangle\langle\psi_k| \quad \text{so that} \quad \sum_k P_k = 1. \quad (\text{A.1})$$

When the system is described by a single state vector $|\psi\rangle$, which means $\hat{\rho} = |\psi\rangle\langle\psi|$, it is said to be in a **pure state**, otherwise it is said to be in a **mixed state**.

Let us consider the orthonormal basis $\{|n\rangle : n \in \{1, 2, \dots, N\}\}$ on which it is possible to represent the states $\{|\psi_k\rangle\}$ and the density operator $\hat{\rho}$ as

$$|\psi_k\rangle = \sum_{n=1}^N |c_{k,n}| e^{i\phi_{k,n}} |n\rangle, \quad \hat{\rho} = \begin{bmatrix} \rho_{1,1} & \cdots & \rho_{1,N} \\ \vdots & \ddots & \vdots \\ \rho_{N,1} & \cdots & \rho_{N,N} \end{bmatrix}, \quad (\text{A.2})$$

$$\text{where } \rho_{m,n} = \langle m|\hat{\rho}|n\rangle \quad (\text{matrix elements}), \quad (\text{A.3})$$

being ρ the **density matrix** and $c_{k,n} = |c_{k,n}| e^{i\phi_{k,n}}$. From now on, we shall assume the abuse of notation $\hat{\rho} = \rho$ in order to make the definition of a density operator easy by using its matrix representation. The probability of finding a state $|n\rangle$ in a given state vector $|\psi_k\rangle$ is $P_k |c_{k,n}|^2$. Then the probability of finding the state $|n\rangle$ in any state vector is

$$\sum_k P_k |c_{k,n}|^2 = \sum_k P_k \underbrace{\langle n|\psi_k\rangle}_{c_{k,n}} \underbrace{\langle\psi_k|n\rangle}_{c_{k,n}^*} = \langle n| \left(\sum_k P_k |\psi_k\rangle\langle\psi_k| \right) |n\rangle = \langle n|\hat{\rho}|n\rangle = \rho_{n,n}. \quad (\text{A.4})$$

Therefore, the diagonal terms, also referred as **populations**, give the probability of measuring the system in some state $|n\rangle$, which implies

$$\text{Tr}[\rho] = \sum_{n=1}^N \langle n|\hat{\rho}|n\rangle = \sum_{n=1}^N \rho_{n,n} = 1, \quad (\text{A.5})$$

where $\text{Tr}[\hat{\rho}]$ is the **trace** of the operator $\hat{\rho}$. This operation is independent of the basis since it is invariant with respect to any unitary transformation. Moreover, the trace is also invariant under cyclic permutation of the product so that

$$\text{Tr}[\hat{A}\hat{B}\hat{C}] = \text{Tr}[\hat{B}\hat{C}\hat{A}] = \text{Tr}[\hat{C}\hat{A}\hat{B}]. \quad (\text{A.6})$$

The off-diagonal terms are called **coherences**. They give information about the relative phase of different components. Let us consider a pure state so that

$$\rho_{m,n} = \langle m| (|\psi\rangle\langle\psi|) |n\rangle = \langle m| \left(\sum_p |c_p| e^{i\phi_p} |p\rangle \right) \left(\sum_q |c_q| e^{-i\phi_q} \langle q| \right) |n\rangle \quad (\text{A.7})$$

$$= \sum_{p,q} |c_p c_q| e^{i(\phi_p - \phi_q)} \langle m|p\rangle \langle q|n\rangle = |c_m c_n| e^{i(\phi_m - \phi_n)} \quad (\text{A.8})$$

For mixed systems, the coherences will be the sum of complex numbers corresponding to different states $|\psi_k\rangle$. Furthermore, it is possible to check whether a system is pure or mixed evaluating the quantity $\text{Tr}[\hat{\rho}^2]$. For a pure state $\hat{\rho}_{\text{pure}} = |\psi\rangle\langle\psi|$, we have

$$\hat{\rho}_{\text{pure}}^2 = |\psi\rangle\langle\psi|\langle\psi|\psi\rangle\langle\psi| = |\psi\rangle\langle\psi| = \hat{\rho}_{\text{pure}} \Rightarrow \text{Tr}[\hat{\rho}_{\text{pure}}^2] = \text{Tr}[\hat{\rho}_{\text{pure}}] = 1. \quad (\text{A.9})$$

Indeed, $\hat{\rho}_{\text{pure}}^n = \hat{\rho}_{\text{pure}}$ for any pure state, being n a non-negative integer. To study the case of a mixed state defined by the density operator $\hat{\rho}_{\text{mixed}}$, let us assume a basis where the matrix ρ_{mixed} is diagonal so that

$$\text{Tr}[\rho_{\text{mixed}}^2] = \sum_n (\rho_{n,n})^2 \leq \sum_n \rho_{n,n} = 1, \quad (\text{A.10})$$

since $0 \leq \rho_{n,n} \leq 1$. A diagonal pure state has only a single non-zero element, whereas a diagonal mixed state necessarily has more than one non-zero element. Hence, being the trace operation independent of the basis, for a mixed state we always have

$$\text{Tr}[\hat{\rho}_{\text{mixed}}^2] < 1. \quad (\text{A.11})$$

We can also compute expectation values using the trace operation. Let us consider an observable \hat{A} whose matrix elements are $A_{m,n} = \langle m|\hat{A}|n\rangle$. The expectation value $\langle\hat{A}\rangle$ is expressed by

$$\langle\hat{A}\rangle = \sum_k P_k \langle\psi_k|\hat{A}|\psi_k\rangle. \quad (\text{A.12})$$

On the other side,

$$\hat{\rho}\hat{A} = \sum_k P_k |\psi_k\rangle\langle\psi_k| \hat{A} \Rightarrow \langle n|\hat{\rho}\hat{A}|n\rangle = \sum_k P_k \langle\psi_k|\hat{A}|n\rangle \langle n|\psi_k\rangle \Rightarrow \quad (\text{A.13})$$

$$\Rightarrow \text{Tr}[\hat{\rho}\hat{A}] = \sum_n \langle n|\hat{\rho}\hat{A}|n\rangle = \sum_k P_k \langle\psi_k|\hat{A} \underbrace{\left(\sum_{n=1}^N |n\rangle\langle n|\right)}_{\mathbb{I}} |\psi_k\rangle = \sum_k P_k \langle\psi_k|\hat{A}|\psi_k\rangle \quad (\text{A.14})$$

$$\therefore \text{Tr}[\hat{\rho}\hat{A}] = \sum_k P_k \langle\psi_k|\hat{A}|\psi_k\rangle = \langle\hat{A}\rangle. \quad (\text{A.15})$$

Therefore, the ensemble average of any observable \hat{A} can be calculated from the diagonal elements of the operator matrix $\hat{\rho}\hat{A}$.

The density operator formalism is also great to manage **composite system**. Let us consider a system A defined by the density operator $\hat{\rho}_A$ and the Hilbert space \mathcal{H}_A , and a system B represented by the density operator $\hat{\rho}_B$ and the Hilbert space \mathcal{H}_B . The total system, which take A and B into account, is described by the density operator $\hat{\rho}_{AB}$ and the Hilbert Space $\mathcal{H}_A \otimes \mathcal{H}_B$. The operator $\hat{\rho}_A$ and $\hat{\rho}_B$ can be seen as **reduced density matrices**, which can be derived from $\hat{\rho}_{AB}$ through the **partial trace operation**,

$$\hat{\rho}_A = \text{Tr}_B[\hat{\rho}_{AB}] \quad \text{and} \quad \hat{\rho}_B = \text{Tr}_A[\hat{\rho}_{AB}]. \quad (\text{A.16})$$

Let us consider a pure state $|\psi_{AB}\rangle$ of both system A and B given by

$$|\psi_{AB}\rangle = \sum_{m,n} c_{m,n} |m\rangle \otimes |n\rangle, \quad \text{where} \quad \sum_{m,n} |c_{m,n}| = 1. \quad (\text{A.17})$$

If the systems are *independent*, we can associate a state $|\psi_A\rangle = \sum a_m |m\rangle$ to the system A and $|\psi_B\rangle = \sum b_n |n\rangle$ to the system B so that

$$|\psi_{AB}\rangle = |\psi_A\rangle \otimes |\psi_B\rangle = \left(\sum_m a_m |m\rangle \right) \otimes \left(\sum_n b_n |n\rangle \right) = \sum_{m,n} a_m b_n |m\rangle \otimes |n\rangle. \quad (\text{A.18})$$

From equations (A.17) and (A.18), we obtain $c_{m,n} = a_m b_n$. Then, the density operator $\hat{\rho}_{AB}$ is given by

$$\begin{aligned} \hat{\rho}_{AB} &= |\psi_{AB}\rangle\langle\psi_{AB}| = \sum_{m,n} \sum_{m',n'} a_m a_{m'} b_n b_{n'} |m\rangle\langle m'| \otimes |n\rangle\langle n'| = \\ &= \left(\sum_{m,m'} a_m a_{m'} |m\rangle\langle m'| \right) \otimes \left(\sum_{n,n'} b_n b_{n'} |n\rangle\langle n'| \right) = \\ &= |\psi_A\rangle\langle\psi_A| \otimes |\psi_B\rangle\langle\psi_B| = \hat{\rho}_A \otimes \hat{\rho}_B. \end{aligned} \quad (\text{A.19})$$

Therefore, when two systems A and B are **uncorrelated** or *independent*, we can write the density operator of both systems as a tensor product between the density operator of the system A and the density operator of the system B ,

$$\hat{\rho}_{AB} = \hat{\rho}_A \otimes \hat{\rho}_B. \quad (\text{A.20})$$

A.0.1 Liouville equation

The time evolution of a state vector $|\psi\rangle$ is given by the Schrodinger equation $\hat{H}|\psi\rangle = i\hbar\partial_t|\psi\rangle$, where \hat{H} is the Hamiltonian of the system. Thereby, the time evolution of $\hat{\rho}$ is given by

$$\partial_t \hat{\rho} = \partial_t \left(\sum_k P_k |\psi_k\rangle\langle\psi_k| \right) = \sum_k P_k [(\partial_t |\psi_k\rangle) \langle\psi_k| + |\psi_k\rangle (\partial_t \langle\psi_k|)] = \quad (\text{A.21})$$

$$= \frac{i}{\hbar} \sum_k P_k (|\psi_k\rangle\langle\psi_k| \hat{H} - \hat{H} |\psi_k\rangle\langle\psi_k|) = \hat{\rho} \hat{H} - \hat{H} \hat{\rho} \quad (\text{A.22})$$

Therefore,

$$\partial_t \hat{\rho} = \frac{i}{\hbar} [\hat{\rho}, \hat{H}], \quad (\text{A.23})$$

where the equation (A.23) is called **von Neumann equation** or **Liouville equation**. The commutator itself can be considered as a **superoperator** acting on the density operator,

$$\mathcal{L}\hat{\rho}(t) \equiv -\frac{i}{\hbar} [\hat{H}, \hat{\rho}(t)], \quad (\text{A.24})$$

where \mathcal{L} is known as **Liouville superoperator**. We shall work with a Hamiltonian in the form $\hat{H} = \hat{H}_0 + \hat{V}(t)$, where \hat{H}_0 is a time-independent part and $\hat{V}(t)$ is a time-dependent term. In this case, it is convenient to define an unitary transformation given by $\hat{U}(t) = e^{-i\hat{H}_0 t/\hbar}$ so that

$$\hat{\rho}'(t) = \hat{U}^\dagger(t) \hat{\rho}(t) \hat{U}(t). \quad (\text{A.25})$$

Calculating the time derivatives on both sides of (A.25) and assuming (A.23), we obtain

$$\partial_t \hat{\rho}'(t) = -\frac{i}{\hbar} [\hat{V}(t), \hat{\rho}'(t)]. \quad (\text{A.26})$$

The equation (A.26) is the **Liouville equation** in the **interaction picture**, which depends only on the time-dependent part.

The equation (A.23) is valid as long as there are only coherent effects on the system, since these processes are represented by unitary time evolutions¹. In the context of atom-light interaction when we assume an density operator associated with the atomic internal states, the Liouville equation only describes stimulated absorption and emission. However, spontaneous emission is a predominant process in MOTs, so it is mandatory to take it into account. To comply with that, we shall introduce the *master equation* in section ??.

A.1 Decoherence

Spontaneous emission comes from a coupling between an open quantum system, described by the density operator $\hat{\rho}_S$, and the environment, represented by the density operator $\hat{\rho}_E$. Moreover, the environment must have far more degrees of freedom than the system. In our case, the system can be understood as the atom and the environment as the vacuum modes of the quantized electromagnetic field. Let us consider a density operator $\hat{\rho}_{SE}$ which represents jointly the system and the environment. Assuming a weak coupling in which the system performs a small perturbation to the environment, we can treat both independently so that

$$\hat{\rho}_{SE} \approx \hat{\rho}_S \otimes \hat{\rho}_E. \quad (\text{A.27})$$

The equation (A.27) is known as the **Born approximation**. At first, both system and environment provoke mutual excitations, getting out of thermal equilibrium. After a while, both will reach equilibrium again through a relaxation process. Let us consider the relaxation times τ_E and τ_S of the environment and the system, respectively. Since the system causes small perturbation to the environment but the environment interacts strongly with the system, we can consider $\tau_E \ll \tau_S$. This is known as **Markov approximation**. The

¹ An unitary time evolution is associated with a hermitian Hamiltonian so that $\hat{U} = e^{-i\hat{H}t/\hbar}$.

equation of motion of $\hat{\rho}_{SE}$ is given by the Liouville equation,

$$i\hbar\partial_t\hat{\rho}_{SE} = [\hat{H}_{SE}, \hat{\rho}_{SE}]. \quad (\text{A.28})$$

Let us consider a multi-level system given by the basis $\{|n\rangle\}$. Taking the Born-Markov approximation into account, it is possible to derive an equation of motion for $\hat{\rho}_S$ tracing out the environment in equation (A.28). The resulting equation (47), known as **master equation** or **Lindblad equation**, is given by

$$\partial_t\hat{\rho}_S = \frac{1}{i\hbar}[\hat{H}_S, \hat{\rho}_S] + \sum_{i,j} \frac{\Gamma_{ij}}{2} (2\hat{\sigma}_{ij}\hat{\rho}_S\hat{\sigma}_{ji} - \{\hat{\sigma}_{ji}\hat{\sigma}_{ij}, \hat{\rho}_S\}) = (\mathcal{L} + \mathcal{L}_{decay})\hat{\rho}_S, \quad (\text{A.29})$$

$$\mathcal{L}_{decay}\hat{\rho} = \sum_{i,j} \frac{\Gamma_{ij}}{2} (2\hat{\sigma}_{ij}\hat{\rho}_S\hat{\sigma}_{ji} - \{\hat{\sigma}_{ji}\hat{\sigma}_{ij}, \hat{\rho}_S\}), \quad (\text{A.30})$$

where $\hat{\sigma}_{ij} = |i\rangle\langle j|$, \mathcal{L}_{decay} is the **Lindblad superoperator**, $\{\hat{A}, \hat{B}\} = \hat{A}\hat{B} + \hat{B}\hat{A}$ is the anticommutator, and $\{\Gamma_{i,j}\}$ are rates, known as *decay rates*, at which both populations and coherences vanish. The operators $\hat{\sigma}_{i,j}$ and $\hat{\sigma}_{j,i} = \hat{\sigma}_{i,j}^\dagger$ can be understood as *lower* and *upper operators* between the states $|i\rangle$ and $|j\rangle$ so that $\hat{\sigma}_{i,j}|j\rangle = |i\rangle$ and $\hat{\sigma}_{j,i}|i\rangle = |j\rangle$. The master equation results in the Liouville equation when $\Gamma_{ij} \rightarrow 0$, $\forall i, j$. Therefore, the difference between these equations is the decay term expressed by the superoperator \mathcal{L}_{decay} known as **Lindblad superoperator**.

Let us consider the case in which only $\{\Gamma_{i,i} = \Gamma_i\}$ are non-zero. Then, the superoperator \mathcal{L}_{decay} can be written as

$$\mathcal{L}_{decay}\hat{\rho} = -\frac{1}{2} \sum_i \Gamma_i \left(\sum_{j \neq i} \rho_{i,j} |i\rangle\langle j| + \sum_{k \neq i} \rho_{k,i} |k\rangle\langle i| \right), \quad (\text{A.31})$$

where $\rho_{i,j} \equiv \langle i|\hat{\rho}|j\rangle$. From equation (A.31), it is possible to see that only the off-diagonal terms are affected by \mathcal{L}_{decay} . Hence, only the coherences decay since they are associated with the off-diagonal terms. This process is known as **pure dephasing**. In the general case when $\Gamma_{i,j} > 0$ for $i \neq j$, the populations also change over time, which is known as **relaxation**. Spontaneous emission is only responsible for *relaxation* terms $\{\Gamma_{i,j}, i \neq j, i < j\}$, whereas the *pure dephasing* terms $\{\Gamma_i\}$ are associated with **elastic collisions**. Furthermore, $\{\Gamma_i\}$ are the rates at which the atoms collide between each other. We are concerned only with the regime of low temperatures in which collisions are negligible.

APPENDIX B – Scattering cross section

In atomic spectroscopy, it is often measure the light power P_{sc} which an atom emits due to spontaneous emission, i.e. the power of the scattered light also known as **fluorescence**. Fluorescence imaging can be used to detect single trapped atoms (48) and momentum distribution (49, 50). In the case of a two-level atom interacting with a monochromatic light whose frequency is ω , we can write P_{sc} as the energy $\hbar\omega_0$ ¹ of a single photon with frequency ω_0 (atomic resonant frequency) times the rate $R_{sc} = \Gamma\rho_{2,2}$ ² at which an atom scatters photons, i.e. the rate at which an atom absorb a photon stimulatory and then emit it spontaneously. Therefore, we can define a cross section given by³.

$$\sigma_{sc}(\Delta) = \frac{P_{sc}}{I_0} = \frac{\hbar\omega_0}{I_0}\Gamma\rho_{2,2} = \frac{\hbar\omega_0}{I_0}\frac{\Gamma}{2}\frac{s_0}{1 + s_0 + (2\Delta/\Gamma)^2}, \quad (\text{B.1})$$

where I_0 is the light intensity. The quantity σ_{sc} is called **scattering cross section** and it is related to the probability of happening a scattering event, i.e, the probability of absorbing a photon and then emitting it spontaneously. From equation (2.103), we have $\sigma_{sc} = \sigma_{abs}$, which is expected due to conservation of energy, i.e. the energy lost from a incident light beam must be convert to scattering light via spontaneous emission. Overall, the total absorption cross section σ_{abs} (section 2.1.5) is associated with *absorption imaging* and the scattering cross section σ_{sc} is associated with *fluorescence imaging*.

¹ The spontaneously emitted photon does not have a single frequency ω_0 (section 2.1.3). However, since ω_0 is much greater than the FWHM of the line shape, we have

$$\omega_0 \simeq \int_0^\infty \omega g(\omega) d\omega$$

² Γ is the rate at which atoms in the excited state emit photons spontaneously and $\rho_{2,2}$ is the probability of finding an atom in the excited state.

³ In a general case,

$$P_{sc} = \int \sigma_{sc}(\omega') I(\omega') d\omega',$$

where $I(\omega')$ is the spectral intensity. However, since $I(\omega') = I_0\delta(\omega' - \omega)$ for a monochromatic light, we can write $P_{sc} = \sigma_{sc}(\omega)I_0$.

APPENDIX C – Selection Rules

In section 2.2.2, we verify that electric-dipole transitions depends on the *transition dipole moment* $\vec{\mu}$. When $|\vec{\mu}|$ is greater than zero, the transition is allowed, otherwise the transition is **dipole forbidden**. The transition moment between two arbitrary electronic states $|i\rangle$ and $|j\rangle$ is given by

$$\vec{\mu}_{i,j} = \langle j|\mathbf{d}|i\rangle = -e \langle j|\mathbf{r}|i\rangle, \quad (\text{C.1})$$

where \mathbf{r} is the electron position. In this section, we shall explore spherical symmetries to obtain conditions in which the transition matrix (C.1) vanishes. These conditions are known as **selection rules**. To effectively investigate such symmetries, let us consider the electron position in spherical coordinates so that

$$\mathbf{r} = r (\sin \theta \cos \phi \mathbf{e}_x + \sin \theta \sin \phi \mathbf{e}_y + \cos \theta \mathbf{e}_z), \quad (\text{C.2})$$

where $\theta \in [0, \pi]$ is the *polar angle*, $\phi \in [0, 2\pi[$ is the *azimuthal angle*, $r \in [0, \infty[$ is the *radial distance*, and $\{\mathbf{e}_x, \mathbf{e}_y, \mathbf{e}_z\}$ is the *Cartesian basis*. It is also convenient to rewrite the position (C.2) on the **spherical basis** given by

$$\left\{ \mathbf{e}_{\pm 1} = \frac{\mp \mathbf{e}_x - i \mathbf{e}_y}{\sqrt{2}} = -(\mathbf{e}_{\mp 1})^*, \mathbf{e}_0 = \mathbf{e}_z \right\} \quad (\text{C.3})$$

so that

$$r_{\pm} = \mp \frac{r}{\sqrt{2}} \sin \theta e^{\mp i \phi} \quad \text{and} \quad r_0 = r \cos \theta, \quad \text{or} \quad (\text{C.4})$$

$$r_q = \mathbf{r} \cdot \mathbf{e}_q^* = r \sqrt{\frac{4\pi}{3}} Y_{1,-q}(\theta, \phi) \quad \text{for } q \in \{-1, 0, 1\}, \quad (\text{C.5})$$

where r_q is a component¹ of \mathbf{r} on the spherical basis and $Y_{l,m}(\theta, \phi)$ is a **spherical harmonic** of degree l and order m .

To evaluate the inner product $\langle i|\mathbf{r}|j\rangle$ in (C.1), we must describe the spatial dependence of $|i\rangle$ and $|j\rangle$. Essentially, an electronic state can be represented by $|n, l, m_l, m_s\rangle^2$ where n, l, m_l and m_s are quantum numbers described below

- *Principal quantum number n* : a positive integer related to the energy and the radial position of the electron;
- *Orbital angular momentum quantum number l* : a positive number in the range $|l| < n$ associated with the total orbital angular momentum \mathbf{L}^2 whose eigenvalues are $\hbar^2 l(l+1)$;

¹ Since the spherical basis is composed of complex elements, we must consider the component of a given \mathbb{C}^3 -vector \mathbf{v} as $v_{\alpha} = \mathbf{v} \cdot \mathbf{e}_{\alpha}^*$.

² We are neglecting the hyperfine structure.

- *Magnetic quantum number* m_l : an integer number in the range $|m_l| \leq l$ related to the z-projection of the orbital angular momentum given by the operator \hat{L}_z whose eigenvalues are $\hbar m_l$;
- *Spin quantum number* m_s : a integer number in the range $|m_s| \leq 1/2$ related to the z-projection of the spin given by the operator \hat{S}_z whose eigenvalues are $\hbar m_s$.

Let us assume $|i\rangle = |n, l, m_l, m_s\rangle$ and $|j\rangle = |n', l', m'_l, m'_s\rangle$ so that $\langle i|r_q|j\rangle = \langle n, l, m_l, m_s|r_q|n', l', m'_l, m'_s\rangle$. Since the spin does not depend on the position, we have $\langle i|r_q|j\rangle = \delta_{m_s, m'_s} \langle n, l, m_l|r_q|n', l', m'_l\rangle$, which means the transition is dipole forbidden when the spin does not remain the same. The angular state $|l, m_l\rangle$ is defined by the *spherical harmonic* $Y_{l, m_l}(\theta, \phi)$ so that, from equation (C.5),

$$\langle n, l, m_l|r_q|n', l', m'_l\rangle \propto \int Y_{l, m_l}^*(\theta, \phi) Y_{1, -q}(\theta, \phi) Y_{l', m'_l}(\theta, \phi) d\Omega \propto \int_0^{2\pi} e^{i(m'_l - m_l - q)\phi} d\phi. \quad (\text{C.6})$$

From the most right term in (C.6), we immediately see that the transition moment is zero when $m'_l - m_l - q \neq 0$, which means the transition is allowed when $\Delta m_l = 0, \pm 1$. The transitions in which $\Delta m_l = 0$ are known as **π -transitions**, whereas the transitions in which $\Delta m_l = \pm 1$ are known as **σ -transitions**.

To evaluate the middle term in (C.6), we shall rewrite the product of two spherical harmonics as a sum of spherical harmonics in the following way³

$$Y_{l_1, m_1} Y_{l_2, m_2} = \sum_{j, m_j} (-1)^m \sqrt{\frac{(2l_1 + 1)(2l_2 + 1)(2j + 1)}{4\pi}} \begin{pmatrix} l_1 & l_2 & j \\ m_1 & m_2 & m_j \end{pmatrix} \begin{pmatrix} l_1 & l_2 & j \\ 0 & 0 & 0 \end{pmatrix} Y_{j, -m_j}, \quad (\text{C.7})$$

where the matrix elements are the **Wigner 3-j symbols** which are directly associated with the **Clebsch-Gordan coefficients**. Thus, plugging $l_1 = 1$, $m_1 = -q$, $l_2 = l'$, and $m_2 = m'_l$ in equation (C.7), we obtain

$$Y_{1, -q} Y_{l', m'_l} = \sum_{j, m_j} (-1)^m \sqrt{\frac{3(2l' + 1)(2j + 1)}{4\pi}} \begin{pmatrix} 1 & l' & j \\ -q & m'_l & m_j \end{pmatrix} \begin{pmatrix} 1 & l' & j \\ 0 & 0 & 0 \end{pmatrix} Y_{j, -m_j}. \quad (\text{C.8})$$

Then, plugging (C.8) in the middle term of (C.6), we obtain

$$\int Y_{l, m_l}^*(\theta, \phi) Y_{1, -q}(\theta, \phi) Y_{l', m'_l}(\theta, \phi) d\Omega = \sum_{j, m_j} A_{j, m_j} \int Y_{l, m_l}^*(\theta, \phi) Y_{j, -m_j}(\theta, \phi) d\Omega, \quad (\text{C.9})$$

where A_{j, m_j} are constants. Since j satisfies the *triangular condition* $|l' - 1| \leq j \leq l' + 1$, the right term in (C.9) is only non-zero when $l = l' \pm 1$ due to the orthogonality property. The case $l = l'$ also seen possible, but the left term in (C.9) is zero due to the parity of the spherical harmonics given by $Y_{l, m}(\mathbf{r}) = (-1)^l Y_{l, m}(\mathbf{r})$, which requires that $l + l' + 1$ to be an even number.

³ See section 7.3.2 Spherical Harmonics in reference (26).

Overall, the selection rules for electric-dipole-transition are given by $\Delta l = \pm 1$, $\Delta m_l = 0, \pm 1$, and $\Delta m_s = 0$. We can see these rules from another perspective when we consider that an atom absorbs or emits a photon. The total angular momentum of any photon is $2\hbar^2$ ($J = 1$). Therefore, $\Delta l = \pm 1$ and $\Delta m = 0, \pm 1$ follow from the conservation of angular momentum.

Besides the transition matrix, the transition also depends on the polarization vector $\vec{\epsilon}$ of the radiation through the Rabi frequency $\Omega \propto \vec{\mu} \cdot \vec{\epsilon}$ in equation (2.50). Let us consider the polarization in the spherical basis such that

$$\vec{\epsilon} = \sum_{n=-1}^1 A_n \mathbf{e}_n \quad \text{and} \quad \sum_{n=-1}^1 |A_n|^2 = 1, \quad (\text{C.10})$$

where A_n is a component of the polarization vector. The components A_{+1} and A_{-1} are related to the right-handed and left-handed circular polarizations respectively, whereas the component A_0 is related to the linear polarization on the z-direction. In the case of π -transitions, the only non-zero component of the electron position is r_0 due to the most right term in equation (C.6). Therefore, these transitions are only induced by linearly polarized light on z-direction. The σ -transitions obey the same logic: right-hand circularly light induces σ^+ -transitions ($\Delta m_l = +1$) and left-hand circularly light induces σ^- -transitions ($\Delta m_l = -1$).